

ABSTRACT

Title of dissertation: INERTIAL WAVES IN A
 LABORATORY MODEL
 OF THE EARTH'S CORE

Santiago Andrés Triana, Doctor of Philosophy, 2011

Dissertation directed by: Professor Daniel P. Lathrop
 Department of Physics

A water-filled three-meter diameter spherical shell built as a model of the Earth's core shows evidence of precessionally forced flows and, when spinning the inner sphere differentially, inertial modes are excited. We identified the precessionally forced flow to be primarily the spin-over inertial mode, i.e., a uniform vorticity flow whose rotation axis is not aligned with the container's rotation axis. A systematic study of the spin-over mode is carried out, showing that the amplitude dependence on the Poincaré number is in qualitative agreement with Busse's laminar theory while its phase differs significantly, likely due to topographic effects. At high rotation rates free shear layers concentrating most of the kinetic energy of the spin-over mode have been observed. When spinning the inner sphere differentially, a total of 12 inertial modes have been identified, reproducing and extending previous experimental results. The inertial modes excited appear ordered according to their azimuthal drift speed as the Rossby number is varied.

INERTIAL WAVES IN A LABORATORY MODEL OF THE
EARTH'S CORE

by

Santiago Andrés Triana

Dissertation submitted to the Faculty of the Graduate School of the
University of Maryland, College Park in partial fulfillment
of the requirements for the degree of
Doctor of Philosophy
2011

Advisory Committee:
Professor Daniel P. Lathrop, Chair/Advisor
Professor Peter Olson
Professor William Dorland
Professor James Duncan
Professor Saswata Hier-Majumder

© Copyright by
Santiago Andrés Triana
2011

Acknowledgments

The design, construction, and early experimental results of the 3-meter experiment have been possible thanks to the infatigable labor of many people. First and foremost, I want to express my deep gratitude to Professor Daniel Lathrop, lead of the project, for allowing me to be part of his group and for his continuous support over all these years. I am really fortunate to have found in Professor Lathrop not only a mentor, but a person with impeccable integrity, not only in the scientific realm but also as a human being and parent. Gracias Dan!

Many skills are needed when working in such a project as is the 3-meter experiment. Donald Martin took care of providing me with all the technical skills needed. He had infinite patience with me while I was learning from him things like how to use a welder, a milling machine, a lathe, etc. He unknowingly taught me the power of common sense also. He kept me safe. To Don, all my gratitude.

My special acknowledgements to my lab partner, Daniel ‘Axl’ Zimmerman, who had to bear with me over all these years. Always sharp, Daniel Zimmerman could quickly get to the bottom of any topic, be it scientific or not, and he always brought clarity to our discussions. His technical skills are just impressive and nobody would have better suited to this project than him. Always available and always knowledgeable, this thesis wouldn’t have been possible without Axl.

I also want to thank Barbara Brawn, who gladly found time in her tight schedule and read all this manuscript. She gave me invaluable suggestions about my use of English (as it is my second language). Merci beaucoup Barbara!

My gratitude as well to J. Pyle, the nicest person I know, and to Nancy Boone, whose efficiency just amazes me. Without them, IREAP would not have been the top research institution that it is today.

I would like to express my deep gratitude to James Weldon whom offered his expertise in the design of the rotating vessel. His extensive experience in designing rotating machinery was invaluable to us, and gave us confidence in our design. Thanks Jim!

Last but not least, I want to express my infinite gratitude and love to my wife An for her unconditional support, to our daughter Maya and our son Lucas, to my mother Luz and to my family in Colombia, especially Abigail, my grandmother, whom I left one day to go to a distant country. No words can express my love for them.

A mi abuelita Abigail

Table of Contents

List of Figures	vii
List of Abbreviations	ix
1 Introduction	1
1.1 Why such an experiment?	1
1.2 A bit of lab history	4
1.3 Prior work	7
1.3.1 Precession	7
1.3.2 Inertial waves and modes	16
1.4 How to read this thesis	28
2 Theory fundamentals	30
2.1 Navier-Stokes equation for a rotating and precessing fluid	30
2.2 Dimensionless form	32
2.3 Plane inertial waves	33
2.4 Contained inertial waves, linear modes	36
2.5 Over-reflection	39
2.6 A precessing spheroid	41
3 Design and construction	46
3.1 Overview	46
3.2 The main vessel	47
3.2.1 Shape of the vessel cavity	50
3.3 Forcing Package	53
3.4 Motor control	61
3.5 Cooling system	65
3.6 Ventilation	65
4 Instrumentation	69
4.1 Instrumentation ports	69
4.2 Pressure Transducers	71
4.3 Ultrasound Velocimetry	75
4.4 Visualization	79
5 Precessional forcing	82
5.1 Stationary state	82
5.2 A free shear layer	93
5.3 Discussion	94

6	Differential rotation forcing	99
6.1	Overview	100
6.2	Pressure amplitudes and flow velocities	104
6.3	Azimuthal wave number determination	114
6.4	Zonal flow	116
6.5	Decay times	119
6.6	Inertial mode ordering	120
6.7	Spectral power scaling	124
6.8	Discussion	126
A	Analytical flow structures	131
B	Technical drawings	136
	Bibliography	158

List of Figures

1.1	The Earth's interior	2
1.2	The precessing Earth	8
1.3	Singularities in the boundary layer	10
1.4	Dye streak deformation in Malkus' experiment	12
1.5	Vanyo's experimental observations	14
1.6	Elliptical streamlines in an ellipsoid	15
1.7	Parameter space, precession	17
1.8	Internal shear layers for the spin-over mode	20
1.9	Internal shear layers evidenced by numerical simulation	22
1.10	Spectrogram from the 60 cm sodium experiment	24
1.11	Spatial patterns in the 60 cm sodium experiment	26
1.12	Continuation of Figure 1.11	27
2.1	Plane inertial wave	35
2.2	Over-reflection diagram	40
2.3	Coordinate system in the precessing frame	42
3.1	Vessel during fabrication	48
3.2	Thermal jacket schematics	49
3.3	Vessel geometrical tolerances	51
3.4	Vessel shape measurement	54
3.5	Vessel cross sections	55
3.6	General cross section with forcing package	57
3.7	Cross section of inner sphere and shaft	58
3.8	Detail of shaft and lid	60
3.9	Bayonet coupler	62
3.10	Photographs, inner sphere and shaft	63
3.11	Ventilation panels	67
3.12	Outdoor equipment	68
4.1	Ports and lid	70
4.2	Instruments on lid	72
4.3	Pressure transducer conditioning circuit	74
4.4	Particle injector diagram	78
4.5	Fluorescein injector diagram	80
5.1	Spin-up from rest, wall shear probe	84
5.2	Space-time plot of flow velocity, steady state	85
5.3	Standard deviation of velocity along chord D, retrograde rotation	87
5.4	Standard deviation (depth averaged) of velocities from chord D	89
5.5	Phase profiles for different retrograde rotation rates, chord D.	90
5.6	Phase profiles for different prograde rotation rates, chord B	91
5.7	Average spin-over phase	92

5.8	Pressure phases	94
5.9	Detail of the internal shear layer.	95
5.10	Ray paths	98
6.1	Pressure spectrogram, $-2.4 < Ro < -1.2$	101
6.2	Pressure spectrogram, $-0.8 < Ro < -0.3$	103
6.3	Pressure spectrum, $Ro = -1$	105
6.4	Pressure spectrogram, $-1.8 < Ro < -1.2$	107
6.5	Pressure and velocity amplitudes	108
6.6	Pressure spectrogram, $-0.86 < Ro < -0.18$	110
6.7	Pressure amplitudes, $-0.86 < Ro < -0.18$	111
6.8	Depth-averaged velocity amplitudes, $-0.86 < Ro < -0.18$	112
6.9	Pressure amplitudes, $E = 7.47 \times 10^{-8}$	113
6.10	Phase shifts	115
6.11	LR space-time diagram	117
6.12	Zonal flow	118
6.13	Mode decay	121
6.14	Angular drift ordering	123
6.15	Spectral power scaling	125
A.1	Flow cross section, modes $(4,1),(6,1),(3,2),(8,1)$	132
A.2	Flow cross section, modes $(5,2),(7,2),(4,3),(6,3)$	133
A.3	Flow cross section, modes $(9,2),(8,3),(5,4),(7,4)$	134
A.4	Flow cross section, mode family $(6,1)$	135

List of Abbreviations

E	Ekman number
Ro	Rossby number
Ω	Poincaré number
Re	Reynolds number
Rm	Magnetic Reynolds number
ν	Kinematic viscosity
\mathbf{u}	Fluid velocity
η	Ellipticity
L	Length scale
ρ	Density
ω	Angular frequency in rad/s
ω_c	Angular speed of the rotating container
P	Pressure
v	Velocity
m	Azimuthal wave number
S	Power spectral density
CMB	Core-mantle boundary
MRI	Magneto-rotational instability
UDV	Ultrasound Doppler velocimetry
3m	The Three-Meter Experiment
IREAP	Institute for Research in Electronics and Applied Physics

Chapter 1

Introduction

1.1 Why such an experiment?

The core of the Earth remains one of the most inaccessible places in the universe. We have scarce and indirect information about it through seismic waves and the magnetic field that can be measured at the surface. Analysis of seismic waves propagating through the interior led Danish seismologist Inge Lehmann in 1929 hypothesize the existence of a solid inner core surrounded by a liquid outer core. This has been corroborated by later seismic measurements, and constitutes our current model (Figure 1.1). Little is known about some of the core's material properties, e.g., the viscosity. In fact, the uncertainty on the viscosity value of the liquid outer core is a few orders of magnitude. Since the geomagnetic field arises from flows within the outer core, its precise generation mechanism remains uncertain to this day.

The problem of the fluid flow within the outer core is difficult not only because of our limited data, but more generally because it is a fluid dynamics problem. The Navier-Stokes equations may accurately represent the flow dynamics, but we do not have a systematic way of solving such equations. Analytical solutions are extremely scarce. To complicate things further, numerical calculations can only take us just so far toward a satisfactory solution, given the wide range of length scales involved.

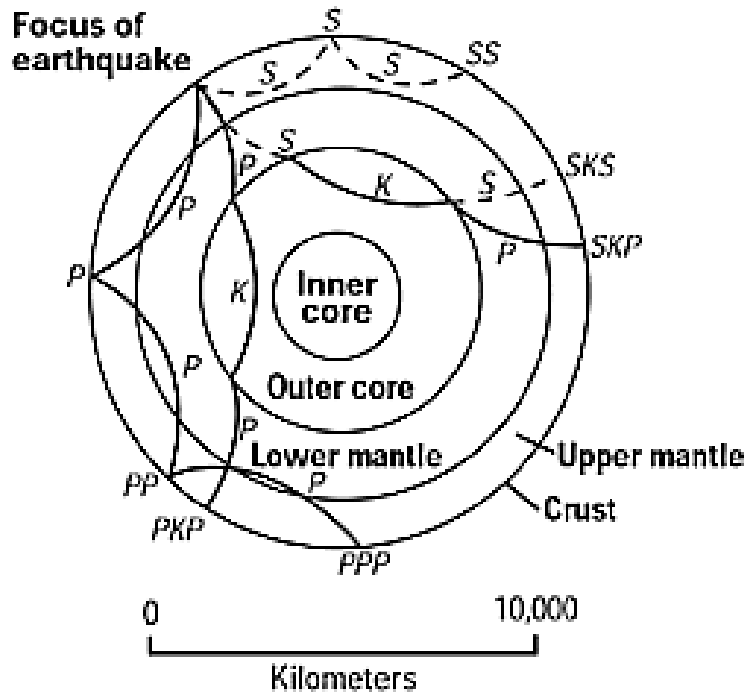


Figure 1.1: The interior of the Earth as revealed by seismic waves. *P* waves are compression waves able to propagate through solids and fluids. *S* waves are shear waves that propagate only through solids although they might excite *P* waves when incident on the liquid outer core (*P* waves in the outer core are denoted *K*).

There is a vast amount of fluid dynamics data produced numerically and not much data produced by direct experimentation or observation, and one sometimes has the impression that not enough effort is made to validate numerically-generated data. Often, analytical results are “validated” only through numerics. Experimental research is at the core of the scientific method and the importance of experimental measurements cannot be overstated. It is sometimes colloquially stated, “the experiment is always right,” when performed properly, even if its physical interpretation proves difficult.

The lab led by Professor D. Lathrop, director of this thesis, has been dedicated to experimental work investigating wide ranging phenomena, from superfluids to liquid metal flows. A series of liquid sodium experiments have been undertaken (including the present study) to explore the possibility of creating a self-sustaining magnetic field in a geometrical configuration similar to that of the Earth’s core. Numerous computational studies suggest dynamo processes occur in such configuration, although the parameter range achieved by such computations is not close to realistic terrestrial or laboratory parameters. Thus, experiments are in order.

A spherical shell configuration is not only attractive because of its potential applicability to the Earth or other astrophysical objects, but it is also interesting from a pure fluid dynamics perspective. Spherical boundaries are described simply, and they are perhaps the simplest boundaries imaginable for a rotating fluid, apart from cylindrical boundaries. In fact, numerous analytical advances have already been achieved for rotating fluids within cylindrical boundaries. Spherical boundaries come naturally as the next step in the challenge.

The original goal is, as mentioned earlier, to create a self-sustaining magnetic field in an unconstrained geometry similar to the Earth's core. We therefore need a fluid that is a good electrical conductor, just like the molten iron in the outer core. Sodium is particularly well-suited for laboratory experiments, given that its melting point is not exceedingly far from room temperature. Its electrical conductivity is higher than other liquid metals, such as mercury or gallium, near or at room temperature. Sodium is not as toxic or heavy as mercury, but it is more difficult to handle than gallium. Sodium is also cheaper than alternatives. It should be mentioned that all safety precautions associated with liquid sodium are very important for us. No shortcuts are taken on this matter.

Thanks to their dual purpose, both geophysical and purely hydrodynamical, spherical shell experiments are likely to be of interest to a wide audience. Although, often the most interesting experimental results come as a surprise, and these results do not exactly correspond to the design purpose of the experimental device. The next section describes our own experience.

1.2 A bit of lab history

The series of experiments with liquid sodium in our lab started with a stationary spherical vessel 30 cm in diameter fitted with various forcing devices, including impellers and spheres with and without baffles. Dynamo action was not achieved, most likely because one of the dimensionless parameters, namely the magnetic Reynolds number, was not large enough to trigger a dynamo instability. Nev-

ertheless, one important observation was made: the magneto-rotational instability or MRI, never observed in a laboratory experiment before. The MRI is important in astrophysics because it provides a mechanism by which angular momentum is transported in accretion disks surrounding stars in formation. An experiment of twice the diameter was then built. The 60 cm experiment was able to rotate, and it incorporated a cooled inner sphere, fixed to the main vessel, to study thermal convection phenomena. This experiment was later modified to allow independent rotation of the inner sphere, eliminating the cooling. Dynamo action was again elusive, although the system exhibited very clean inertial modes forced by the inner sphere rotation. A new question arose with these observations, i.e., how precisely are these inertial modes excited by the inner sphere? This question is partially addressed in this thesis.

At the same time these smaller experiments were under way, we were designing and building a three meter (abbreviated 3m from now on) diameter experiment. Designed as its predecessors to use liquid sodium, this large experiment promises to bring us closer to achieving dynamo action: in fact, it will achieve the largest magnetic Reynolds number of any sodium experiment globally due to its sheer size. The 3m project is by far the largest rotating spherical shell experiment today, and its design and construction proved to be a challenging and time-consuming task. Daniel Zimmerman (PhD student), Donald Martin (technician), Professor Daniel Lathrop (lead of the project), and the author comprised the team. The magnitude of the task required tenacity and endurance from all of us, on a level that we never imagined when we started the project. We persisted, and in 2008 the long construction phase

was over.

The next step was to test the system mechanically using water as the working fluid, prior to running with sodium. This is because it would be extremely difficult to take the sodium out and perform fixes; once sodium is in place, it will be there for the life of the experiment. During the water testing phase, some mechanical corrections were made and instrumentation was added incrementally. We eventually reached a point where enough instruments were in place to perform a characterization of the purely hydrodynamic flow. Obviously, we would have designed the system differently if our interest had been just hydrodynamics (as opposed to hydro-magnetics). Nevertheless our measurements during this water testing phase unveiled phenomena interesting enough to warrant detailed and systematic studies. One of those interesting phenomena, and rather surprising at first, was that when the inner sphere was locked to the outer sphere and rotating as a solid body with constant angular speed, there was always a small oscillating flow (in the rotating frame) no matter how long we waited for transients to die out. A fluid in a uniformly rotating container should eventually rotate in unison with its container after enough time has elapsed. This was briefly a puzzle, until we realized that our giant sphere was not just uniformly rotating but also precessing, its spin axis being fixed to our rotating planet. We decided to study this phenomenon by varying our only control parameter (the rotation rate), and to see how well theory was applicable. One of the main results of this thesis encompasses the systematic study of the flow induced by this type of forcing. When the inner sphere is rotated at a different angular speed than the outer sphere, inertial modes are excited in exactly the same way as in the 60 cm

experiment. These measurements, and their comparison to 60 cm data, comprise the rest of the experimental results of this thesis.

Another surprising phenomenon we observed was that, for some range of rotation rate ratios (positive, both spheres rotating in the same direction), the torque exerted by the motor on the inner sphere would suddenly decrease, stay low and gradually grow back to its original value only to crash again some time later. This would go on repeatedly, and apparently in a completely random fashion. The systematic study of this bistability phenomenon is the subject of Daniel Zimmerman's dissertation work. Both Daniel Zimmerman's thesis and the present work represent an exhaustive study of hydrodynamic phenomena taking place in the 3m experiment. We feel this knowledge will be essential background for the liquid sodium experiments in the 3m system.

1.3 Prior work

1.3.1 Precession

Ptolemy (*c.* AD 90 - 168) relates in his *Almagesto* that Hipparchus (*c.* 190 BC - *c.* 120 BC) realized, through star longitude measurements, that the equinoxes were moving at a rate no less than 1° in a century. Several centuries later, Sir Isaac Newton identified the combined gravitational torques from the Sun and the Moon on a bulging Earth as the cause of this phenomenon. It was not until the mid-18th century, with the works of D'Alembert and Euler on rigid body rotations that an adequate theoretical framework was available. Jean Baptiste Joseph Delambre, at

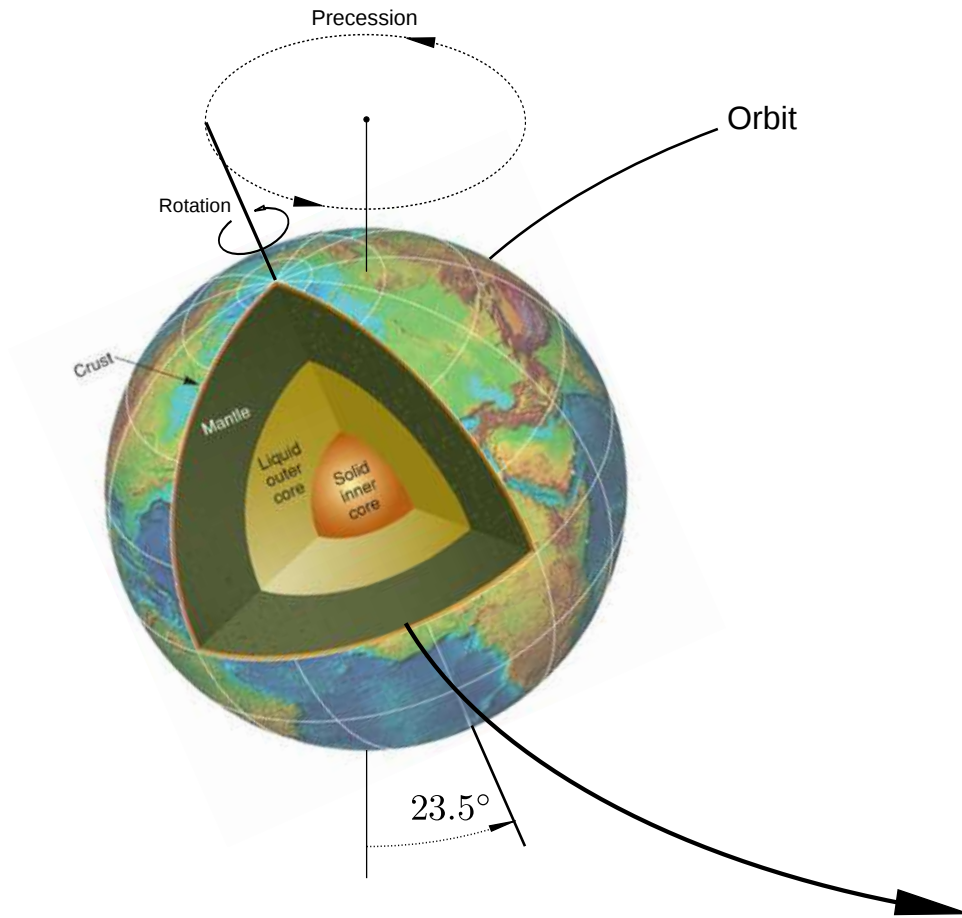


Figure 1.2: Our planet possesses a fluid outer core and a solid inner core. The rotation axis does not stay constant in inertial space but precesses due to the torque exerted by the Sun and the Moon with a period of roughly 26000 years.

the beginning of the 19th century estimated, from astronomical observations, the Earth's precession period to be 25960 years, less than half a percent off from its current accepted value.

Near the beginning of the 20th century a major question was whether the Earth was liquid or solid in its interior. Lord Kelvin and Poincaré considered in this context the problem of an inviscid fluid in a precessing ellipsoidal cavity. Poincaré

found that the nutation periods of a fluid Earth are shorter than the nutation periods of a solid Earth. Given that long nutation periods are observed he concluded that the Earth was completely solid. We know today that this effect is related to the elasticity of the mantle, as well as exchanges between the mantle and the oceans or the atmosphere. Nevertheless, Poincaré's work is very important since it established in particular that the flow of an inviscid fluid in an precessing ellipsoidal container possesses uniform vorticity. Honoring this work, a uniform vorticity flow is known in modern literature as a Poincaré flow. With the advent of modern seismology as mentioned above, a global picture of the Earth's interior emerged (see Figure 1.2). Once the Earth's interior structure was established, the focus shifted to the fluid dynamics of the outer core. In this context Bondi & Littleton in 1953 [3] took a closer look at the problem of the flow in a precessing spheroid and tried to include the effects of finite viscosity. They identified certain singularities on the Ekman layer (see Figure 1.3), but at the same time analytical difficulties led them to think that no steady state was possible for a viscous fluid in a precessing spheroid. Ten years later, Stewartson & Roberts [50] [43] used a small-amplitude approximation allowing the boundary-layer equations to be linear. They concluded that a steady state was possible, and represented the steady-state solution as a Poincaré solution modified only near the boundaries by a viscous boundary layer. In light of their analysis, the viscous boundary layer also showed the divergence noted earlier by Bondi & Littleton.

A milestone was reached when Busse [5], building upon the work of Roberts & Stewartson, successfully included the non-linear terms in the boundary-layer analysis.

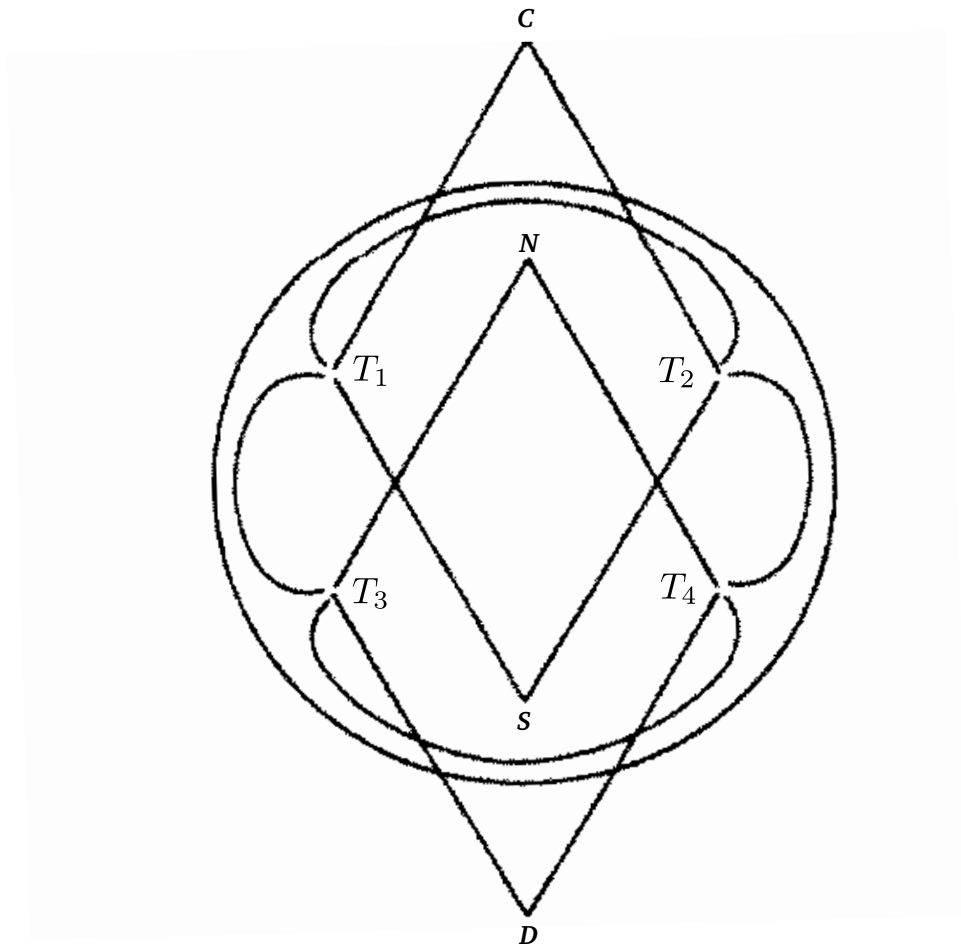


Figure 1.3: Cross section of the core through the polar axis showing the singularities on the boundary layer according to Bondi & Lyttleton [3]. Points labeled T_1 through T_4 mark the intersections of the characteristic cones with the bulging Ekman layer.

According to this analysis, viscosity selects one Poincaré solution with a particular orientation in space, and the non-linear advection of the boundary-layer velocity field superimposes a differential rotation of the fluid interior onto the uniform vorticity flow. Busse also noted that the divergence in the Ekman layer at the critical latitudes differed from the previous results, in that the critical latitudes are to be referred to the fluid-spin axis, not the container-rotation axis.

At almost the same time, Malkus [26] reported experiments with a precessing spheroid that largely agreed with Busse's theory, including the cylindrically symmetric differential rotation connecting the critical latitudes (see Figure 1.4). These experiments also exhibited a rather peculiar phenomenon: for some precession-to-rotation ratios, the flow became completely chaotic, while the dissipation suddenly increased as evidenced by the torque applied by the motor. There was no evidence of the free conical shear layers (discussed in the next section) caused by the thickening of the Ekman layer at the critical latitudes. In addition, Malkus advanced the hypothesis that the precession induced flow in the outer core of the Earth could provide enough energy to power the geodynamo, thus providing an alternate view from the widely accepted idea that the outer core flow (and ultimately the geodynamo) is powered by thermal or compositional convection.

A series of experiments by Vanyo [58][57][59] revealed not only the cylindrical shear layer connecting the critical latitudes, but also many other weaker layers in a coaxial and nested fashion. Numerous visual observations evidenced vortices appearing on the cylindrical shear layers in a way much reminiscent of the Kelvin-Helmholtz instability. A schematic diagram is shown in Figure 1.5. An axial velocity was also

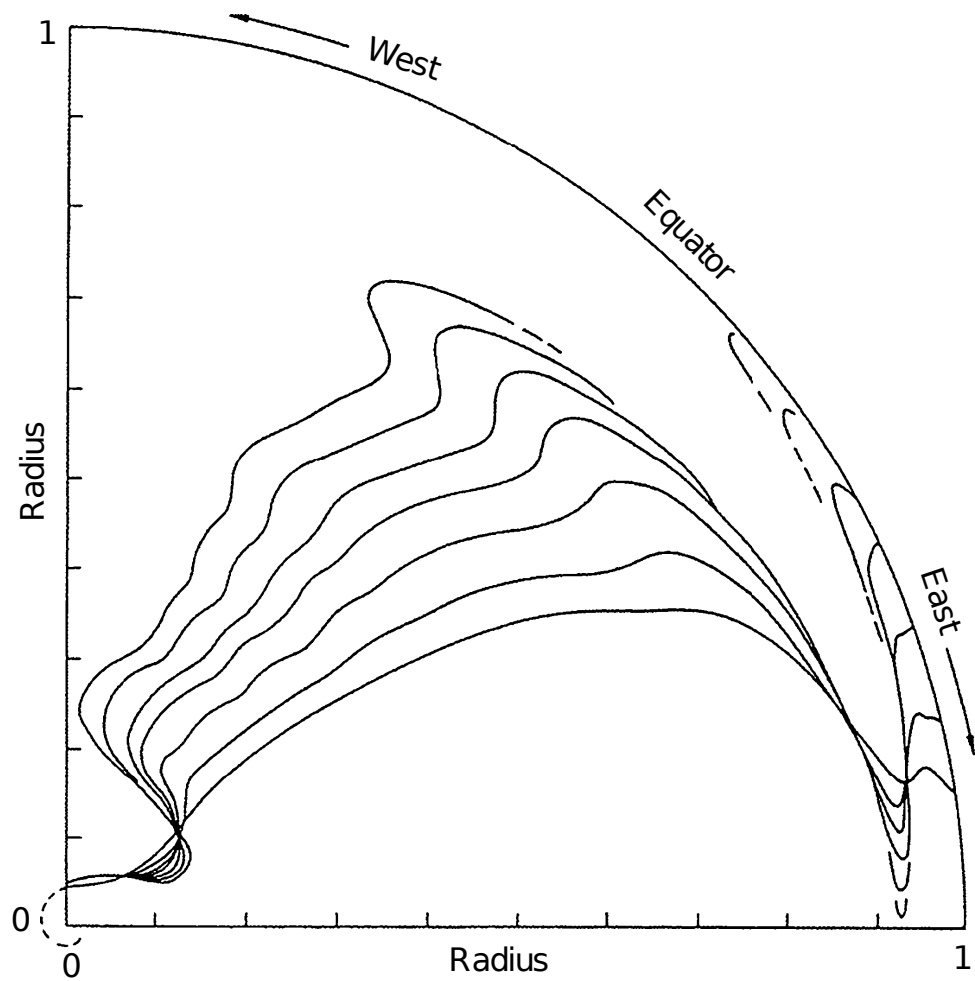


Figure 1.4: A dye streak on the equatorial plane is deformed in this precession experiment by Malkus [26]. The strongest deformation occurs at a radius ~ 0.866 where a cylinder connects the critical latitudes ($\cos 30^\circ = 0.866$) on the boundary. Rotation axis points out of the page.

detected along the vortices, making their flow helical. These helical structures are not fundamentally different from helical structures arising in buoyancy-driven flow, which is known to support dynamo action. Therefore precession-induced flow might act as a dynamo as well. Once again, the conical shear layers spawned by the thickening of the Ekman layer were elusive to detection in Vanyo's experiments.

In 1975 the idea of a geodynamo caused by precession found some resistance in the works of Rochester [44] and Loper [20]. Their criticism focused on the *laminar* aspects of precession-induced flow, establishing that the energy input would be insufficient and would dissipate mostly in the boundary layers. The interest in precession-driven dynamos was virtually nonexistent for almost two decades, until the work of Kerswell [17]. He calculated an upper bound for energy dissipation in *turbulent* precession large enough (14 orders of magnitude more than the laminar value) to power the geodynamo. Another work by Kerswell [15] provided an analytical explanation to the sudden disorder outbreak observed in the experiment by Malkus. It showed that the constant vorticity solution was actually inertially unstable by virtue of the resonant coupling of two inertial modes (see next section on inertial waves) by the underlying constant strain field. In a precessing spheroid, the Poincaré flow possesses elliptical streamlines causing an elliptical strain. Additionally and more importantly, there is a shearing component in the direction perpendicular to the plane of the elliptical streamlines (see Figure 1.6). Studies in cylindrical geometries have documented how inertial modes, once excited, tend suddenly to break down into turbulence. For instance, the works of McEwan (who coined the term resonant collapse) [29], Manasseh [27] [28] and Stergiopoulos &

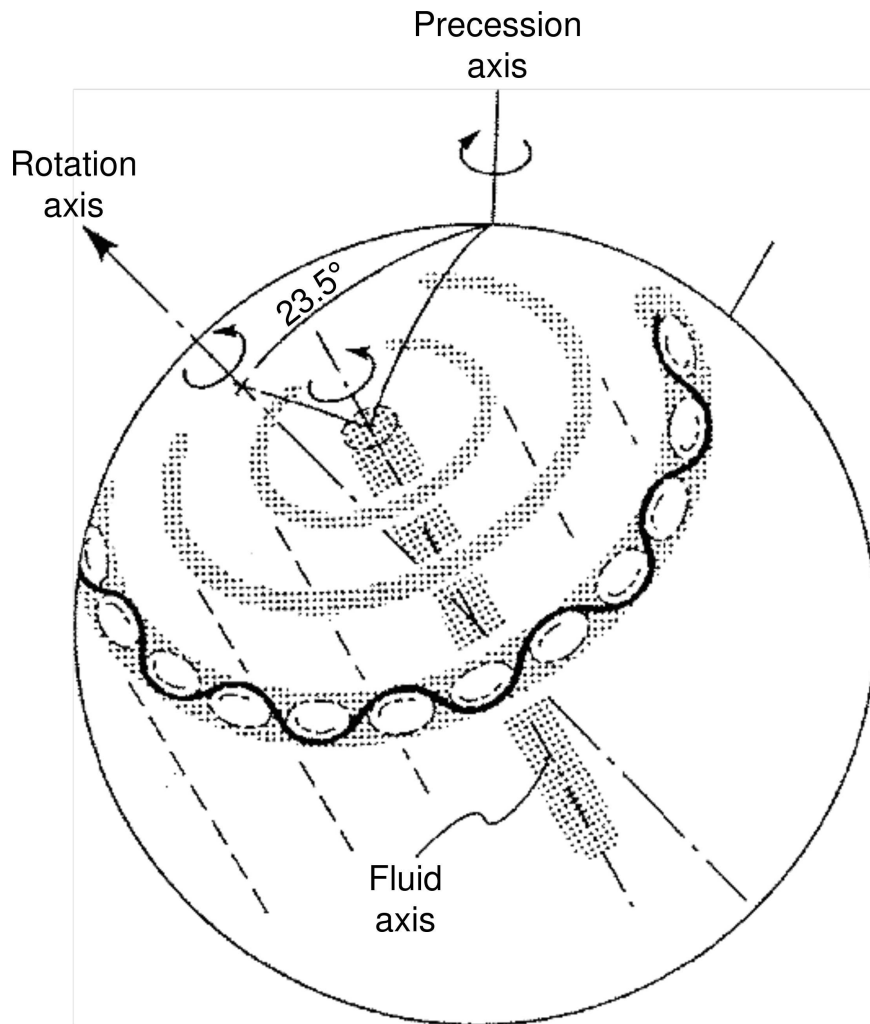


Figure 1.5: Vanyo's experiments with precessing spheroids [57] revealed nested cylindrical shear layers aligned with the fluid spin orientation. These shear layers develop wave-like instabilities at high precession rates.

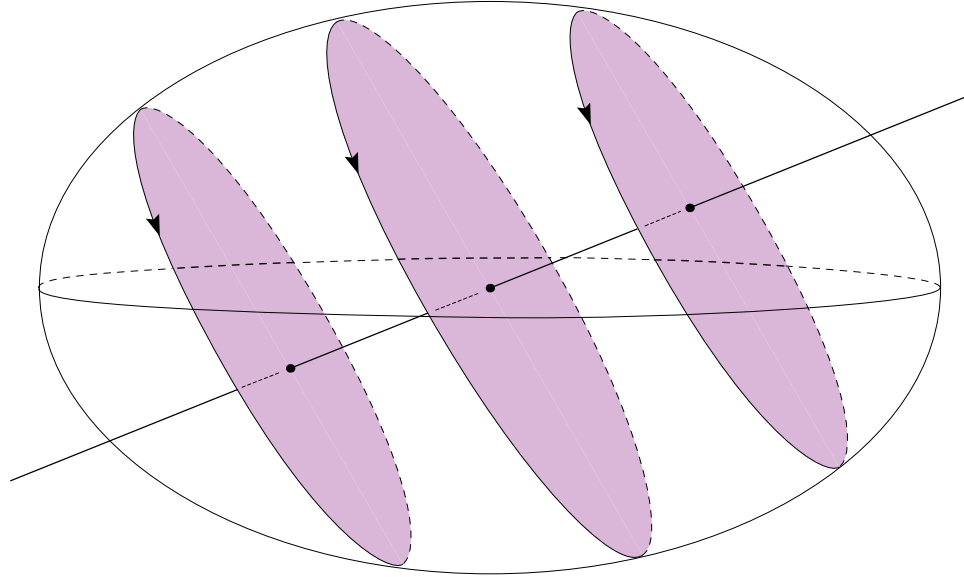


Figure 1.6: Elliptical streamlines for the Poincaré flow in an ellipsoid. Note that the center of the ellipses do not coincide causing shear over all the volume.

Aldridge [49] all suggest that the turbulent collapse in Malkus’s experiments is yet another manifestation of the same process.

The third and most recent series of experiments (apart from the present study) with precessing spheroids was carried out by Noir et al [35] [37]. These experiments tested Busse’s theory and showed good agreement, even for some parameter ranges where the theory does not formally hold. Experiments were also performed in a range of parameters where Busse’s theory predicts three different solutions, i.e., three different possible orientations of the fluid-spin axis. This situation has been described as one of non-linear resonance between the precessional forcing and the spin-over mode by Pais & LeMöuel [38]. The conical shear layers that the previous experiments failed to find was observed in Noir’s experiment by means of ultrasound

velocimetry, satisfactorily matching the velocity field they had calculated numerically [36].

With the ever-increasing computational power available, numerical calculations became possible using parameters never reached before. Examples of this are the works of Tilgner & Busse on precession induced flows [56], the study by Tilgner on hydromagnetics of the flow in a precessing sphere [52] and the works of Lorenzani & Tilgner on instabilities in a precessing flow [21] [22]. These numerical studies have recreated the cylindrical shear layers so familiar from the experiments, as well as the conical shear layers emanating from the critical latitudes. Although the smallest Ekman numbers achieved in these calculations reaches $E = 10^{-5}$, the magnitude of the velocities in the shear layers do not seem to follow any simple power law, which might be an indication that the asymptotic limit is still far away.

Regarding the geodynamo, the numerical solutions definitely show that precession can support a dynamo instability as exemplified by the work of Tilgner [54] [55] and more recently by Wu & Roberts [60] [61]. The question is whether and how the dynamo is able to tap the energy available from precession or convection. Future theoretical, observational, experimental and numerical progress on these matters will have the answer.

1.3.2 Inertial waves and modes

The Poincaré flow (the spin-over mode) excited by precession turns out to be just the first in a series of fluid wave modes in a cavity that are supported by

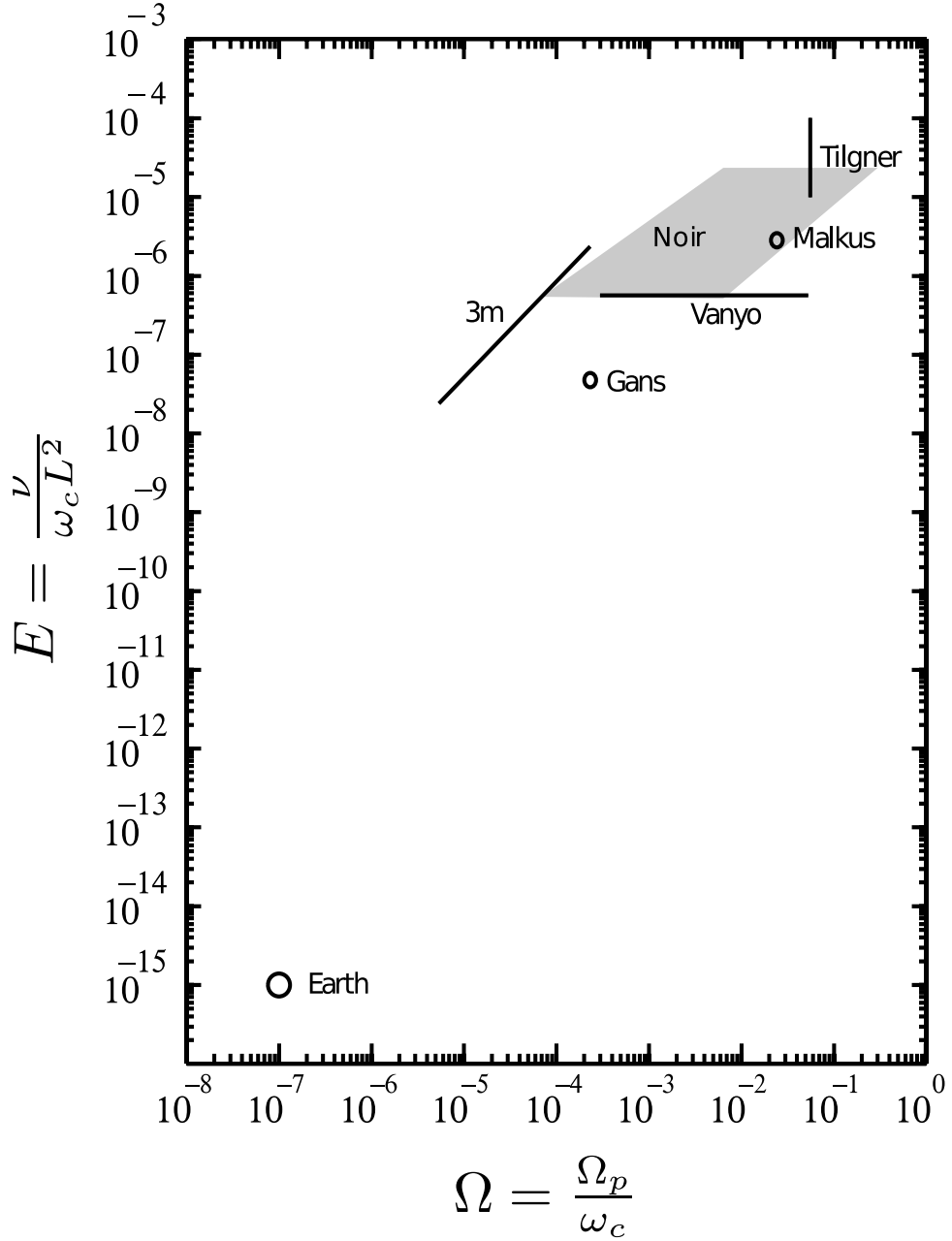


Figure 1.7: Approximate location of various experiments (Noir, Vanyo, Malkus, Gans, 3m), simulations (Noir, Tilgner) and the Earth’s core in (Ω, E) parameter space. There is a large uncertainty in the actual value of viscosity in the Earth’s core. Its corresponding Ekman number value shown is a figure often quoted in the literature. Here ω_c is the angular speed the corresponding fluid-filled cavity (of length scale L) and Ω_p is the precession rate.

the restoring action of the Coriolis force. The study of inertial modes was initiated by Kelvin in 1880, when he considered the oscillations of cylindrical vortices. Soon after, Poincaré derived the basic governing equations for the pressure which are named after him (for a derivation see Chapter 2). In 1889, Bryan found an implicit analytical solution for the inertial modes in a spheroid, but it was not until 1959 that inertial oscillations were experimentally demonstrated by Fultz. The rather pathological character of the problem of contained inertial waves in a shell geometry was considered by Stewartson & Rickard in 1969, at the same time that Aldridge & Toomre reported [2] their experimental findings on inertial modes on a full sphere matching theoretical expectations. An improved method of calculating the inviscid full sphere solution was obtained by Kudlick in his PhD thesis [18] (see also Greenspan [10]). Inertial modes in a cylinder were studied by McEwan in 1970 [29].

In 1987 Aldridge & Lumb [1] claimed detection of inertial waves in the outer core triggered by perturbation of the Earth's rotation after large earthquakes. Rieutord [41] points to the work of Neuberg, Hinderer & Zürn [34] as supporting evidence of the existence of the spin-over mode in the core. By careful measurement of the rotational modes of the Earth, e.g. using superconducting gravimeters, it might be possible to infer some details about the modes in the outer core [46] [32] [45]. The obliquity of the outer core spin axis with respect to the mantle spin axis (i.e. the spin-over mode), is incorporated in models of the Earth's nutation, exemplified by the work of Buffett [4]. At any rate the opportunities for observing the spin-over mode or higher inertial modes are scarce and detection is difficult. The existence

of the spin-over mode in the fluid outer core of Earth is generally acknowledged, although incontrovertible evidence of excitation of higher inertial modes is yet to come.

The analytical inviscid solutions for the inertial modes in a full sphere are well-behaved, but they do not meet no-slip boundary conditions. If no-slip boundary conditions are specified, the mathematical problem becomes *ill-posed* in general. Singularities appear that propagate along the *characteristic* surfaces, which in this case are cones aligned with the rotation axis. In real applications, the Ekman number is small but not zero, turning the mathematical problem into a well-posed *elliptic* one instead of an ill-posed *hyperbolic* one. “Scars” of the discontinuities in the inviscid problem appear in the finite-viscosity problem in the form of conical shear layers emanating from the critical latitudes as studied in detail by Kerswell [16] and Hollerbach & Kerswell [12] (see Figure 1.8). Very enlightening numerical work by Fotheringham & Hollerbach [7] reveals the effect of changing the boundary conditions from slip-free to no-slip on either the inner or outer boundary in a spherical shell problem. Details on the asymptotic behavior (i.e. as the Ekman number goes to zero) of the shear layers present in spherical shell modes have been studied extensively by M. Rieutord and collaborators [41] [40] [42].

One of the most striking features of inertial waves is their particular reflection upon solid boundaries, making equal angles with respect to the rotation axis, not with the normal to the solid surface, as reported earlier in 1963 by Phillips [39]. The conical shear layers can be represented as inertial wave packets traveling along the characteristic cones and reflecting off the solid boundaries. This opens the possibility

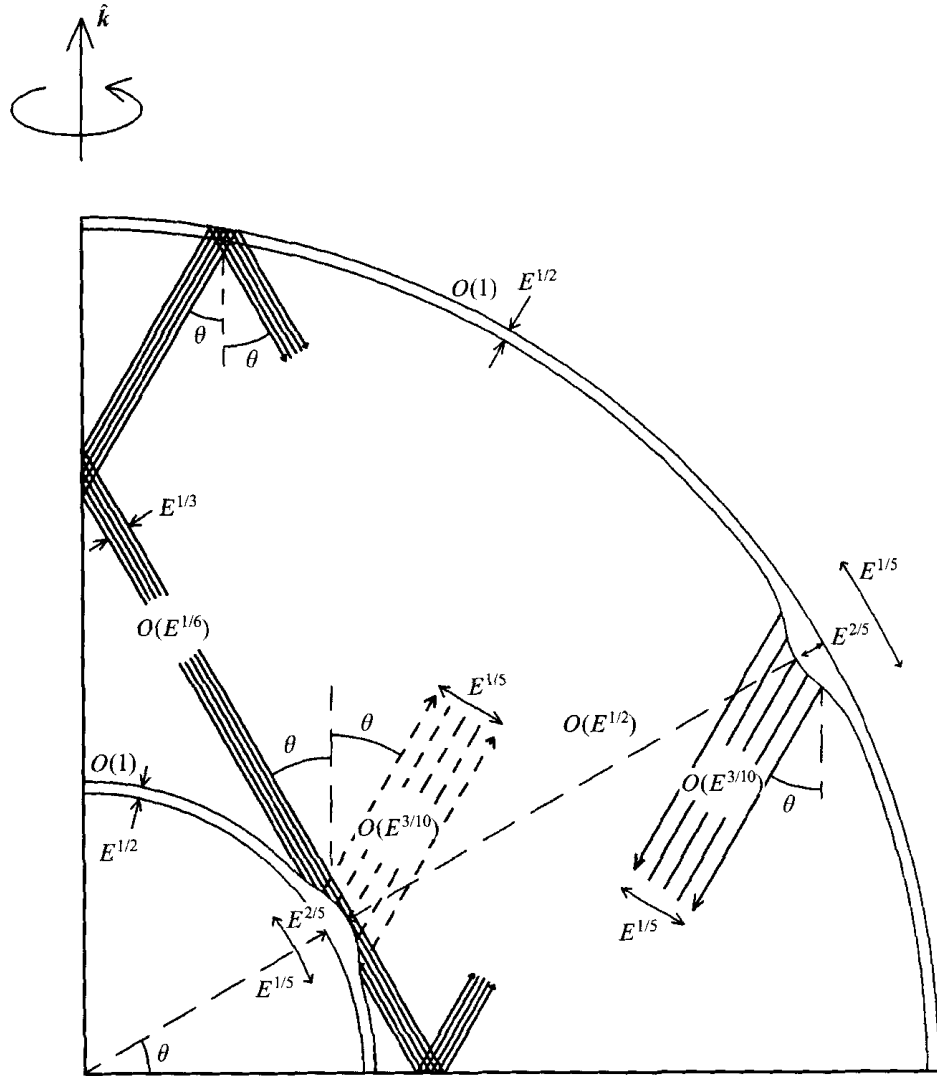


Figure 1.8: Internal shear layers originating at the critical latitudes for the spin-over mode in a spherical shell according to Kerswell [16]. The background flow field has amplitude $O(E^{1/2})$. The flow amplitude in the shear layer domains and their width is indicated.

of periodic orbits and even attractors to which the inertial waves might get “focused”, as discussed by Maas [24], Rieutord [40] and Tilgner [51]. One might imagine a perturbation created by the thickening of the Ekman layer at the critical latitudes, and propagating through the characteristic cones; after a number of reflections the wave might eventually live in a periodic orbit, limit cycle or, in some cases, an attractor if waves starting near the critical latitudes also end up in the same closed path. This phenomenon is not restricted to inertial waves, but extends to internal waves (where buoyancy is the restoring force) since their dispersion relations have the same form [25]. Much of what is known about internal waves in stratified fluids can therefore be applied to inertial waves in rotating fluids.

There are a number of experimental studies on localized inertial waves (as shear layers on characteristic surfaces) dating back to the work of Görtler in 1957 [9] and as recently as 2008 [30], using basically the same cylindrical configuration. As was mentioned in the previous section, many other studies failed to show the shear layers in an spheroid until the experimental work of Noir [36].

Although no inertial waves are reported, the numerical work of Dormy [6] in spherical-Couette flow is relevant. It describes, through numerical experiments, the structure of the Stewartson layer when the inner sphere rotates just slightly faster or slower than the outer sphere (i.e. an infinitesimal Rossby number). They include the hydromagnetic case, and they are able to reach Ekman numbers as small as 10^{-8} .

Schaeffer [47] describes very briefly an experiment with the same spherical-Couette geometry as the 3m system (or the 60 cm sodium experiment for that

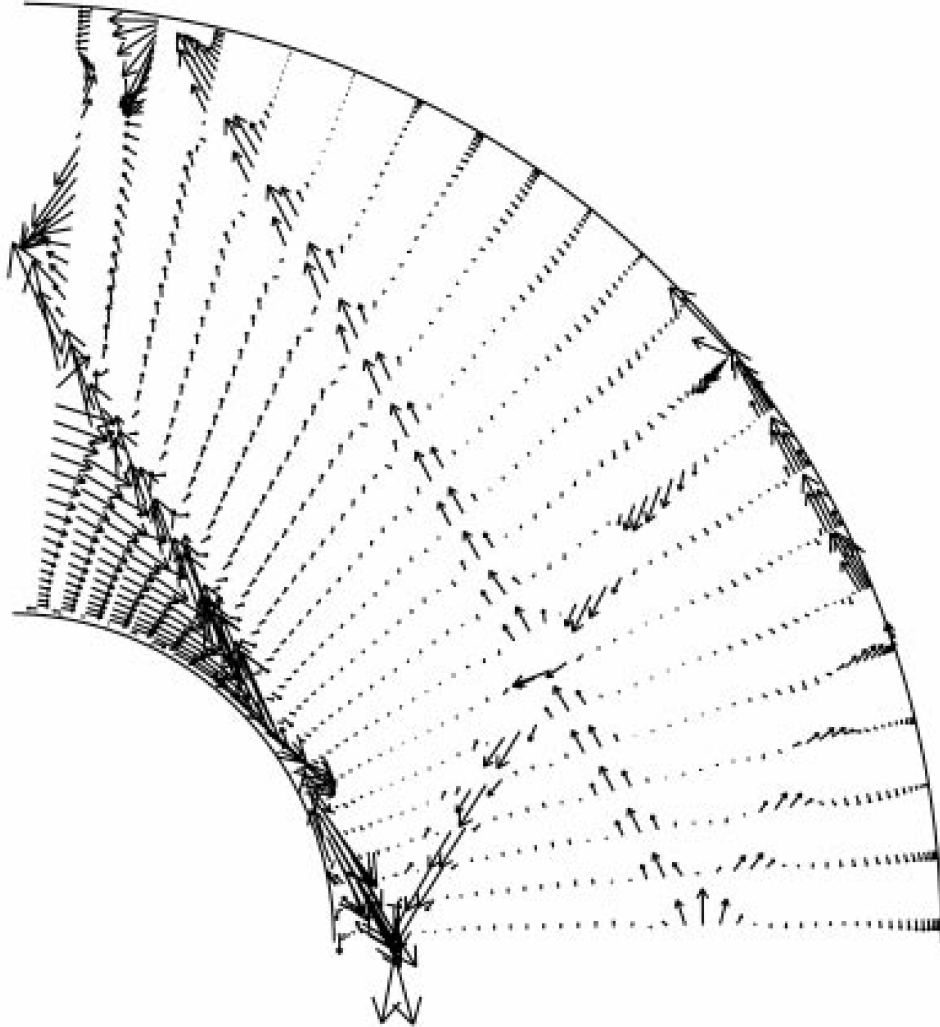


Figure 1.9: Internal shear layers are evident in this numerical simulation by A. Tilgner [51]. The inner and outer boundaries are spheroids with ellipticities equal to $1/400$. Ekman number is $E = 3 \times 10^{-6}$. Boundary conditions are stress-free at the outer boundary and no slip at the inner boundary. Overall rotation has been subtracted as well as the Ekman layer on the inner sphere.

matter), for a differential rotation range that overlaps partially with ours. Their Ekman number ranged from 2×10^{-5} to 3×10^{-6} , larger than our largest Ekman number $\sim 5 \times 10^{-7}$. They did observe a destabilization of the Stewartson layer at moderately small Rossby numbers, consistent for the most part with their own numerical model, and consistent as well with the numerical study by Hollerbach [11].

A directly relevant numerical study on spherical Couette flows is the work of Hollerbach in 2003 [11], mentioned above. He also considered the flow between two concentric spheres, where the inner sphere rotates at a different speed from the outer. The smallest Ekman number achieved in that study ($\sim 10^{-5}$) is still two orders of magnitude larger than our largest Ekman number. The critical Rossby numbers at which non-axisymmetric instabilities already appear are small (~ 0.1). The study also shows differences between flow instabilities for positive and negative Rossby numbers. In the 3m system the smallest Rossby number achieved so far is around 0.2.

Contained inertial modes were visualized via their magnetic signature in a rapidly rotating shell filled with liquid sodium and under an external magnetic field [14]. This work was performed by D. Kelley (while a PhD student in our group) using the 60 cm device referred to in section 1.2. The forcing consisted of rotating the inner sphere at a rotation rate different from the rotation rate of the outer sphere. This forcing is axisymmetric and symmetric with respect to the equatorial plane. By applying an axial, constant, and approximately homogeneous magnetic field aligned with the rotation axis, we were able to measure the induced magnetic

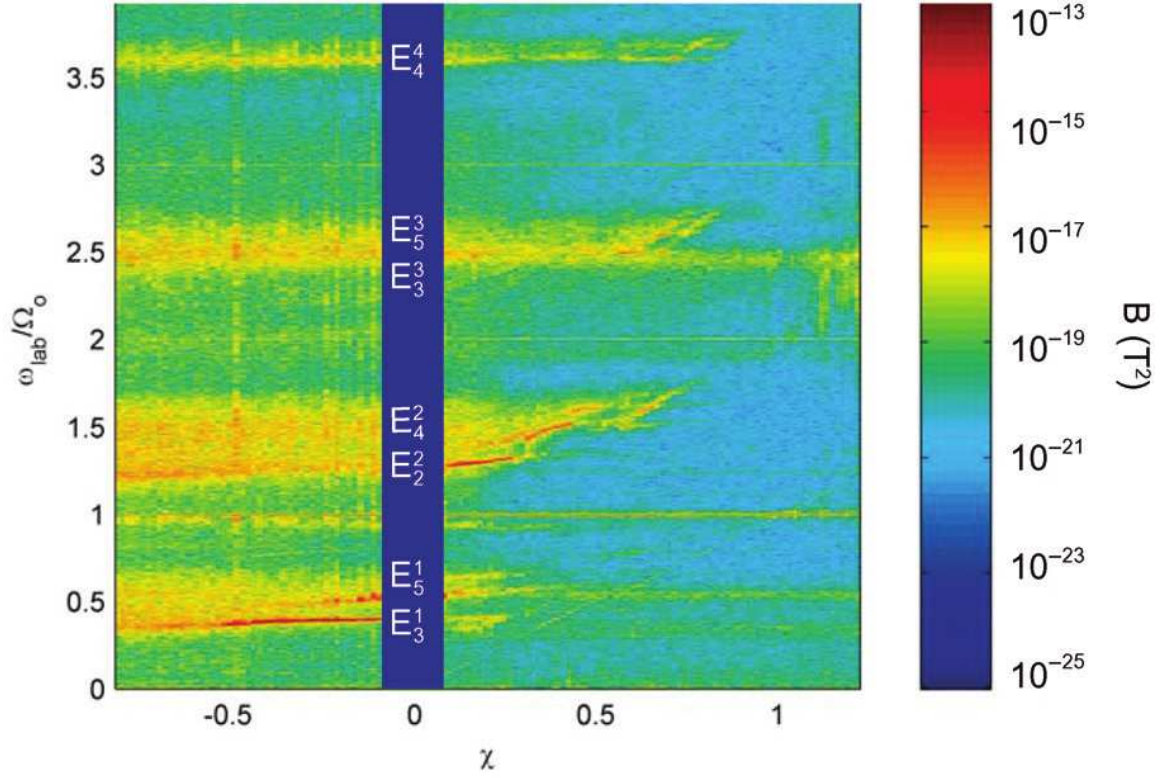


Figure 1.10: Spectrogram from a magnetic Hall probe signal in the 60 cm sodium experiment. The parameter χ is the rotation rate ratio of the inner sphere to the outer sphere, Ω_i/Ω_o . Each vertical line in this image is a color coded power spectrum of the measured magnetic field in the cylindrical radial direction just outside the spinning vessel. Banding according to different azimuthal wave numbers m can be appreciated. The Ekman number here is $E = 4.36 \times 10^{-8}$.

field arising from the inertial wave modes excited by the inner sphere. The magnetic field induced and measured just outside the rotating outer sphere revealed both the frequency (Figure 1.10) and the spatial patterns (Figures 1.11 and 1.12) of the modes. For a given inner-to-outer sphere rotation rate ratio there was typically one or two inertial modes populated. A closer examination showed that the observed modes corresponded to *some* of the inertial modes possible in a *full sphere*. Figure 1.10 shows an spectrogram computed from one of the magnetic Hall probes. It shows the progression of modes excited as the inner sphere rotation varies. We will make extensive use of the 60 cm sodium data both for comparison and to complement our observations in the 3m experiment.

In a recent paper [13], we elaborated on a hypothesis that attributed the selection rules for the modes to a mechanism of over-reflection of inertial waves. It should be mentioned that the explanation we put forward is, in a sense, phenomenological, and not without some conceptual difficulties that will be discussed at the end of Chapter 6.

A recent numerical study by Rieutord and Valdettaro [42] is of particular relevance. They obtained results for a range of very low Ekman numbers that include the range corresponding to both the 60 cm experiment and the 3m experiment. We will see that some of the results from those two experiments satisfactorily agree with a numerical simulation using the same code as used in [42]. This is a remarkable fact given the rarity of occasions when numerical predictions and experiments match in these parameter ranges.

Another recent experiment very similar to the 60 cm sodium experiment is the

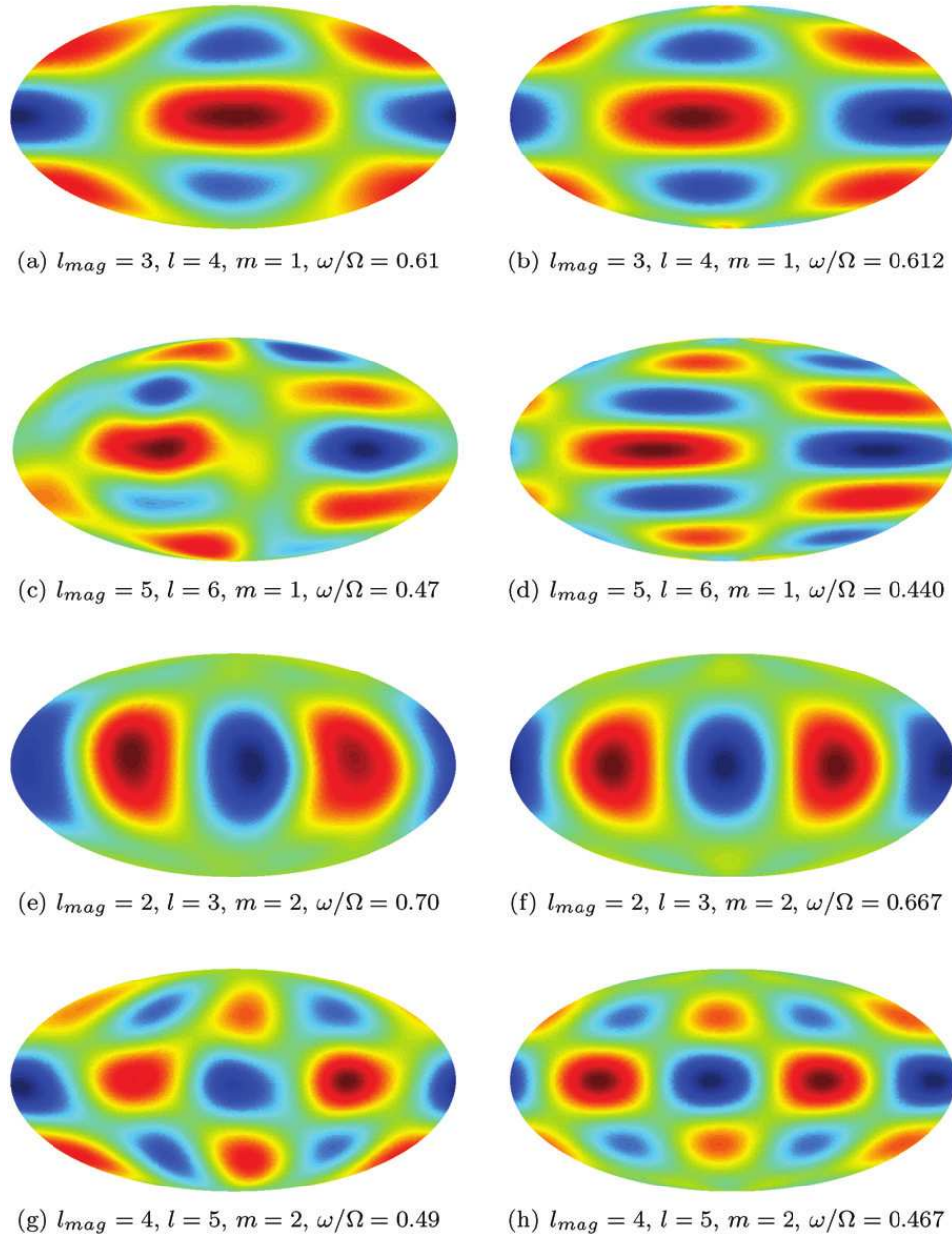


Figure 1.11: The left column here shows the (cylindrical radial) magnetic field measured using a stationary hall probe array around the spinning 60 cm sodium vessel. Magnetic data has been projected using a Mollweide projection. The patterns satisfactorily match the magnetic patterns computed (right column) for full-sphere inviscid modes (see Chapter 2).

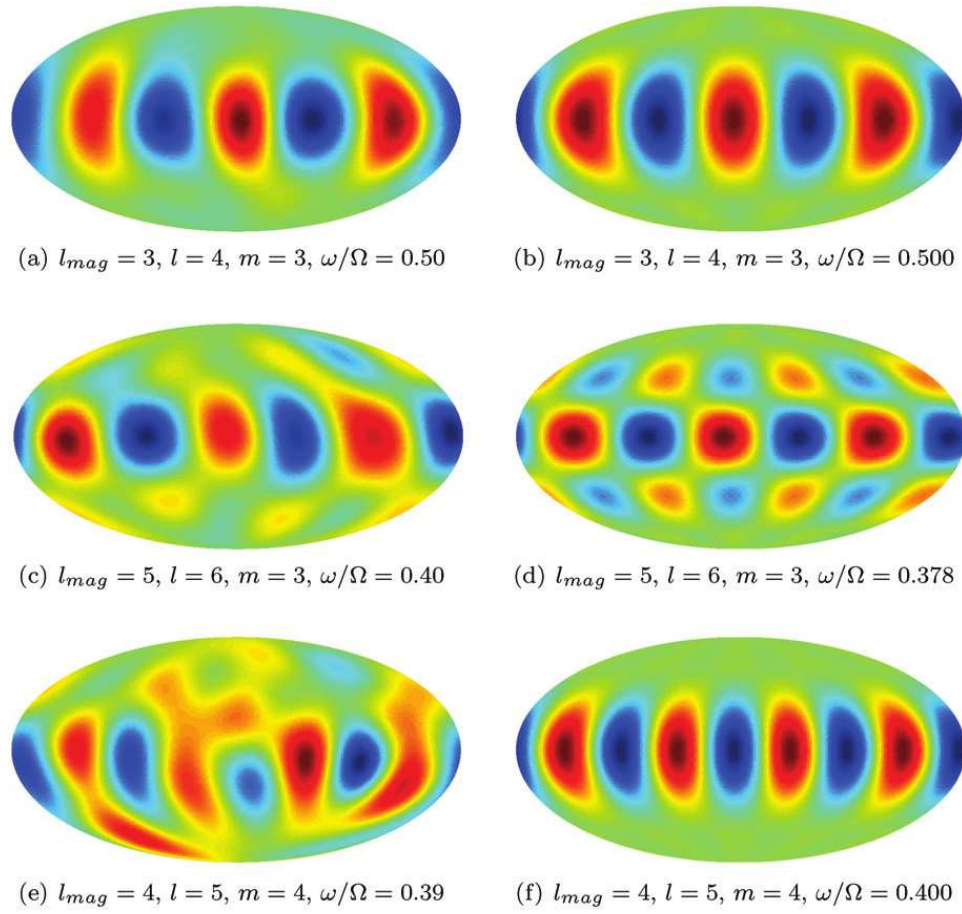


Figure 1.12: Continuation of Figure 1.11

DTS (Derviche Tourneur Sodium), which consists of a strongly magnetized inner core spinning inside a rotating spherical vessel filled with sodium. Schmitt [48] has reported the appearance of magneto-inertial waves in that device with azimuthal numbers up to seven and propagating in the retrograde direction. These waves might be the magnetic counterpart of the inertial modes observed in the 60 cm experiment and in the 3m system.

We end this review with a very recent experimental study on a tidally forced fluid ellipsoid carried out by Morize et.al. [33]. They were able to measure large azimuthal flows induced by the non-linear interaction of inertial modes excited by a tidal deformation of the outer boundary, consistent with the numerical study by Tilgner [55]. Their Ekman number is $\sim 10^{-5}$. They measured geostrophic flows whose velocities scaled as $\epsilon^2 E^{-3/10}$. They argue there that geostrophic cylinders carrying substantial azimuthal flow are a general feature of Ekman boundary layers whenever there is harmonic forcing (tides, precession, nutation, etc.)

1.4 How to read this thesis

This thesis reports on three different aspects on the work by the author on the 3m project. First we report on the design and construction of the rotating vessel (chapter three), second we report on the design, setup and testing of the instruments (chapter four), and the remaining two chapters comprise the systematic measurements on precessionally induced flows and on inertial wave modes forced by differential rotation (chapters five and six).

In the introductory chapter, the reader will find terms (like “magnetic Reynolds number”, “inertial mode”, “characteristic surfaces,” etc.) that might be unfamiliar. The second chapter introduces all definitions and relevant physical concepts in an almost self-contained way. Scientific results are presented in chapter five and six, and they assume familiarity with the concepts discussed in chapter two.

Chapters three and four will perhaps appeal more to engineers, experimentalists, or technicians. Lots of mechanical details and experimental difficulties are discussed. The majority of the time invested in the project was spent in the design and construction stage, something hardly evident from a perusal of the corresponding chapters. After all, it is a large-scale experiment, and we are a small team. As reference for future students/researchers/technicians, the technical drawings are included in the appendices.

As a final note, this manuscript should be considered as the “sister thesis” to Daniel S. Zimmerman’s thesis [63]. If some detail regarding the experiment is missing here, it is very likely it is discussed in Daniel Zimmerman’s thesis and vice-versa. Together they comprise a comprehensive account of the design, construction and early scientific results of the 3m project.

Chapter 2

Theory fundamentals

2.1 Navier-Stokes equation for a rotating and precessing fluid

Let us begin with a description of the dynamics of a fluid. Consider the time evolution of the velocity field \mathbf{u} (referenced to an inertial frame) of an incompressible ($\nabla \cdot \mathbf{u} = 0$) fluid with kinematic viscosity ν and density ρ . It is described by the Navier-Stokes equation (2.1):

$$\frac{\partial \mathbf{u}}{\partial t} + (\mathbf{u} \cdot \nabla) \mathbf{u} = -\frac{\nabla P}{\rho} + \nu \nabla^2 \mathbf{u}, \quad (2.1)$$

where P is the pressure, together with suitable boundary conditions. Let us switch now to a rotating reference frame R with an instantaneous angular velocity vector $\boldsymbol{\omega}$ relative to inertial space. Denoting with \mathbf{r} the position vector of a fluid parcel, we can express the relation between the rate of change of \mathbf{r} as measured in inertial space and the rate of change referred to R as (see Goldstein):

$$\left(\frac{\partial \mathbf{r}}{\partial t} \right)_I = \left(\frac{\partial \mathbf{r}}{\partial t} \right)_R + \boldsymbol{\omega} \times \mathbf{r}. \quad (2.2)$$

The accelerations are then related through

$$\left(\frac{\partial^2 \mathbf{r}}{\partial t^2} \right)_I = \left(\frac{\partial^2 \mathbf{r}}{\partial t^2} \right)_R + 2\boldsymbol{\omega} \times \left(\frac{\partial \mathbf{r}}{\partial t} \right)_R + \boldsymbol{\omega} \times (\boldsymbol{\omega} \times \mathbf{r}) + \left(\frac{\partial \boldsymbol{\omega}}{\partial t} \right)_I \times \mathbf{r}. \quad (2.3)$$

The second, third and fourth terms on the right-hand side correspond to Coriolis forces, centrifugal forces and Poincaré forces respectively. This last term only arises

in non-uniformly rotating systems. Let us now introduce a rotating and precessing boundary (with angular velocity $\boldsymbol{\omega}_c$ and precession vector $\boldsymbol{\Omega}_p$) enclosing the fluid and rigidly attach to it the reference frame R so that $\boldsymbol{\omega} = \boldsymbol{\omega}_c + \boldsymbol{\Omega}_p$. Not surprisingly, when considering the Earth this reference frame is usually called the *mantle* frame. Perhaps risking a bit of confusion, we will depart from this convention and refer to it simply as the *rotating* frame, even if it is also precessing. By using the following relations:

$$\begin{aligned}\mathbf{u} &= \mathbf{u}_R + \boldsymbol{\omega} \times \mathbf{r} \\ \nabla^2 \mathbf{u} &= \nabla^2 \mathbf{u}_R \\ \left(\frac{\partial \boldsymbol{\omega}}{\partial t} \right)_I &= \boldsymbol{\Omega}_p \times \boldsymbol{\omega}_c \\ \boldsymbol{\omega} \times (\boldsymbol{\omega} \times \mathbf{r}) &= -\frac{1}{2} \nabla (\boldsymbol{\omega} \times \mathbf{r})^2,\end{aligned}$$

where \mathbf{u}_R denotes the fluid velocity referred to frame R , we can then write an equation for the motion as seen from R (dropping the R subscript on \mathbf{u}):

$$\frac{\partial \mathbf{u}}{\partial t} + (\mathbf{u} \cdot \nabla) \mathbf{u} + 2(\boldsymbol{\Omega}_p + \boldsymbol{\omega}_c) \times \mathbf{u} + (\boldsymbol{\Omega}_p \times \boldsymbol{\omega}_c) \times \mathbf{r} = -\nabla p + \nu \nabla^2 \mathbf{u}, \quad (2.4)$$

where p is the *reduced* pressure defined as

$$p = \frac{P}{\rho} - \frac{1}{2} (\boldsymbol{\omega} \times \mathbf{r})^2. \quad (2.5)$$

The Coriolis and Poincaré terms appear explicitly while the centrifugal term is implicit in the reduced pressure p . No-slip boundary conditions are specified simply by setting $\mathbf{u} = 0$ on the boundaries.

Now in the *precessing* frame we have $\boldsymbol{\omega} = \boldsymbol{\Omega}_p$. In this frame both $\boldsymbol{\omega}_c$ and $\boldsymbol{\Omega}_p$

are stationary. The Poincaré term disappears and the equation of motion is

$$\frac{\partial \mathbf{u}}{\partial t} + (\mathbf{u} \cdot \nabla) \mathbf{u} + 2\boldsymbol{\Omega}_p \times \mathbf{u} = -\nabla p + \nu \nabla^2 \mathbf{u}, \quad (2.6)$$

which is simpler, although no-slip boundary conditions have to be specified this time as $\mathbf{u} = \boldsymbol{\omega}_c \times \mathbf{r}$ for \mathbf{r} on the boundaries.

2.2 Dimensionless form

The dynamics of a given physical system depend in general on different parameters of the system. For a fluid these parameters may include container size, typical velocity or viscosity. As long as the parameters stay fixed, the dynamics are the same. In some circumstances, a change in one parameter can be compensated for by changes in other parameters, so that the dynamics stay the same. One can then construct a dimensionless quantity from the parameters, so that if the dimensionless quantity does not change the dynamics remain unchanged. A theorem by Buckingham provides a systematic method for finding such dimensionless quantities. Since these quantities are sometimes not unique, the method is not guaranteed to find the most physically meaningful quantities. A dimensionless equation for the dynamics is desirable because it is generalizable, and also suitable for numerical work.

For a rotating and precessing fluid, a dimensionless form can be obtained if we measure time in units of $1/\omega_c$, length in units of system size L and fluid velocity in units of a typical fluid velocity U (some authors use the tangential velocity at the equator for a fluid in a rotating sphere). A dimensionless form with three dimensionless parameters is then obtained if the reduced pressure is measured in

units of $\omega_c LU$. The three dimensionless parameters are

$$E = \frac{\nu}{\omega_c L^2}, \quad Ro = \frac{U}{\omega_c L}, \quad \Omega = \frac{\Omega_p}{\omega_c}. \quad (2.7)$$

These are known as the Ekman, Rossby and Poincaré numbers respectively. If we choose a coordinate system whose z axis points in the same direction as $\boldsymbol{\omega}_c$ then $\boldsymbol{\omega}_c = \omega_c \hat{\mathbf{z}}$ and we can write in the rotating frame (or mantle frame)

$$\frac{\partial \mathbf{u}}{\partial t} + Ro(\mathbf{u} \cdot \nabla) \mathbf{u} + 2(\boldsymbol{\Omega} + \hat{\mathbf{z}}) \times \mathbf{u} + \frac{1}{Ro}(\boldsymbol{\Omega} \times \hat{\mathbf{z}}) \times \mathbf{r} = -\nabla p + E \nabla^2 \mathbf{u}, \quad (2.8)$$

The Ekman number tells us how the viscous forces compare with the Coriolis force and the Rossby number gives an overall estimate of the ratio of convective accelerations to Coriolis forces. In the precessing frame we write

$$\frac{\partial \mathbf{u}}{\partial t} + Ro(\mathbf{u} \cdot \nabla) \mathbf{u} + 2\boldsymbol{\Omega} \times \mathbf{u} = -\nabla p + E \nabla^2 \mathbf{u}. \quad (2.9)$$

Numerical work is usually performed in the rotating frame where velocities are small. Analytical work is conceptually simpler in the precessing frame. In the case of our experiment, the precessing frame coincides with the *laboratory* frame where the rotation axis as well as the precession axis stay fixed in space, while the rotating frame is attached to the rotating vessel.

2.3 Plane inertial waves

Let us now consider small perturbations of an unbounded, inviscid ($E = 0$) fluid in uniform rotation. In the rotating frame, if the perturbations are small enough, we can set $Ro = 0$ and get

$$\frac{\partial \mathbf{u}}{\partial t} + 2\hat{\mathbf{z}} \times \mathbf{u} = -\nabla p. \quad (2.10)$$

After taking the curl two times on both sides of (2.10) and cross-differentiating we get

$$\frac{\partial^2}{\partial t^2} \nabla^2 \mathbf{u} + 4 \frac{\partial^2}{\partial z^2} \mathbf{u} = 0 \quad (2.11)$$

which is a hyperbolic partial differential equation, and therefore admits plane wave solutions $\mathbf{u} \propto e^{i(\mathbf{k} \cdot \mathbf{r} - \omega t)}$ ¹, provided that

$$\omega = \pm 2\hat{\mathbf{k}} \cdot \hat{\mathbf{z}}. \quad (2.12)$$

The differential equation for the reduced pressure p has exactly the same form as (2.11) and can be obtained in a similar manner. It ends up as

$$\frac{\partial^2}{\partial t^2} \nabla^2 p + 4 \frac{\partial^2}{\partial z^2} p = 0, \quad (2.13)$$

which is known in the literature as the Poincaré equation. Again, we assume $p \propto e^{-i\omega t}$ and the Poincaré equation reads, using a (x, y, z) Cartesian coordinate system:

$$\frac{\partial^2 p}{\partial x^2} + \frac{\partial^2 p}{\partial y^2} + \left(\frac{\omega^2 - 4}{\omega^2} \right) \frac{\partial^2 p}{\partial z^2} = 0. \quad (2.14)$$

We see explicitly here that, depending on the sign of the third term on the left-hand side of (2.14), the problem classifies as *hyperbolic* ($\omega^2 < 4$) where wave motion is possible, or *elliptic* ($\omega^2 > 4$) in which case it becomes a Laplace problem resembling potential flow in a non-rotating fluid. The wave motion will take place on *characteristic surfaces*: a unit vector with components ξ_x, ξ_y, ξ_z is normal to a characteristic surface if

$$\xi_x^2 + \xi_y^2 + \left(\frac{\omega^2 - 4}{\omega^2} \right) \xi_z^2 = 0 \quad (2.15)$$

¹Note that ω corresponds in this case to the dimensionless angular frequency of the oscillations caused by the perturbation, not the angular frequency of the fluid rotation (which is simply equal to unity in its dimensionless form).

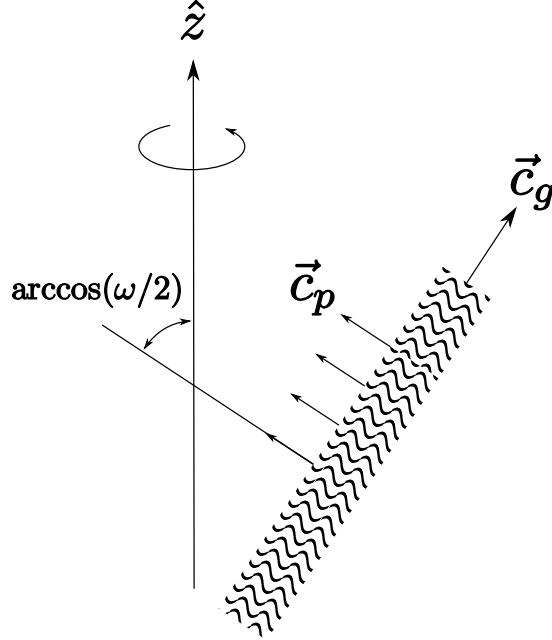


Figure 2.1: A plane inertial wave. The energy propagates with velocity \mathbf{c}_g but the wave fronts propagate at velocity \mathbf{c}_p at right angles from \mathbf{c}_g . The rotation axis $\hat{\mathbf{z}}$, \mathbf{c}_g and \mathbf{c}_p all lie on the same plane.

which means $\xi_z = \pm\omega/2$. The characteristic surfaces are then cones whose axes coincide with the z axis, and all normal vectors will make an angle $\pm \arccos(\omega/2)$ with that axis. If the perturbation is localized, it will send waves propagating along these characteristic surfaces. The angle $\theta_c = \arccos(\omega/2)$ is known as the *critical angle*.

Relation (2.12) is a rather peculiar dispersion relation, since the frequency does not depend on the wavelength but only on the direction of the wave vector. The velocity of the phase fronts c_p reads

$$\mathbf{c}_p = \pm 2 \frac{\hat{\mathbf{k}} \cdot \hat{\mathbf{z}}}{k} \hat{\mathbf{k}} \quad (2.16)$$

and the group velocity $\mathbf{c}_g = \nabla_{\mathbf{k}}\omega(\mathbf{k})$ is given by

$$\mathbf{c}_g = \pm \frac{2}{k} \hat{\mathbf{k}} \times (\hat{\mathbf{z}} \times \hat{\mathbf{k}}). \quad (2.17)$$

Therefore \mathbf{c}_p and \mathbf{c}_g are perpendicular to each other, see Figure 2.1. The inertial waves are then dispersive in general, although it is possible to set up a wave packet composed of plane waves with a single common frequency but different wavelengths, resulting in a wave whose envelope (in the direction perpendicular to the energy propagation) stays unchanged in time [53].

Inertial waves incident on a solid surface conserve their oscillation frequency after reflection, i.e. the angle between the wave vector \mathbf{k} and the rotation axis $\hat{\mathbf{z}}$ remains constant. Therefore they do not obey the familiar laws of reflection where the angles of incidence and reflection are the same with respect to the normal of the surface [39].

2.4 Contained inertial waves, linear modes

Let us consider an inviscid fluid in a uniformly rotating spherical cavity. As in previous section we will consider small deviations of the flow from uniform rotation. We will now include a no-penetration boundary condition on the spherical boundary

$$\mathbf{u} \cdot \hat{\mathbf{n}} = 0, \quad (2.18)$$

where $\hat{\mathbf{n}}$ is any normal to the boundary. Using cylindrical coordinates (s, θ, ϕ) and assuming a harmonic time dependence the solution for the velocity and the reduced

pressure have the form

$$\mathbf{u}(s, z, \phi, t) = \mathbf{U}(s, z)e^{m\phi+i\omega t}, \quad (2.19)$$

$$p(s, z, \phi, t) = f(s, z)e^{m\phi+i\omega t} \quad (2.20)$$

The functions f and \mathbf{U} are related through:

$$\begin{aligned} U_s &= \frac{i}{\omega^2 - 4} \left(\frac{2mf}{s} + \omega \frac{\partial f}{\partial s} \right) \\ U_\phi &= \frac{1}{4 - \omega^2} \left(\frac{\omega mf}{s} + 2 \frac{\partial f}{\partial s} \right) \\ U_z &= \frac{i}{\omega} \frac{\partial f}{\partial z}. \end{aligned} \quad (2.21)$$

An implicit expression for $f(s, z)$ was found by Bryan in 1880. An improved expression for spheroids in general was found by Kudlick in 1966; for a sphere it reads

$$f(s, z) = c_{lm}(\sigma_{lmn}z)^\nu \left(\frac{s}{\alpha} \right)^m \prod_{k=1}^N \{x_k^2(1 - \sigma_{lmn}^2)s^2 + \sigma_{lmn}^2(1 - x_k^2)z^2 + x_k^2(x_k^2 - 1)\} \quad (2.22)$$

where for brevity

$$c_{lm} = \frac{(2l)!}{2^l l! (l-m)!}, \quad \alpha^2 = \frac{1}{1 - \sigma_{lmn}^2}, \quad \sigma_{lmn} = \frac{\omega_{lmn}}{2}$$

and x_k are the real zeros of the associated Legendre polynomials $P_l^m(x)$ in the interval $(0, 1)$. There are N of them according to

$$N = l - m - \nu, \quad \text{with } \nu = \begin{cases} 0 & \text{if } (l - m) \text{ even,} \\ 1 & \text{if } (l - m) \text{ odd.} \end{cases}$$

There is also the same number of eigenfrequencies σ_{lmn} , $n = 1, \dots, N$ for each pair of (l, m) numbers. These eigenfrequencies are determined by solving for σ in

$$(1 - \sigma^2) \frac{d}{d\sigma} P_l^m(\sigma) = m P_l^m(\sigma). \quad (2.23)$$

For $N > 4$, it is not possible to write an analytical expression for x_k in (2.22) and therefore the polynomial $f(s, z)$ cannot be written explicitly. Zhang [62] found explicit general expressions for the components of \mathbf{U} , allowing in particular the calculation of the dissipation integral as identically vanishing for all inertial modes in a sphere.

Greenspan has formulated the problem of fluid motion inside a rotating container as a zeroth-order motion (e.g. the linear modes described above) and a series of viscous corrections in half-powers of the Ekman number E . At each stage a viscous correction on the boundary layer is made and its corresponding modification on the interior flow is calculated. A first order correction on the interior flow induces a second-order boundary layer flow which in turn modifies the interior to second order. Using a first-order order approximation $O(E^{1/2})$, the viscous decay rate can be computed for the linear modes. This is a rather laborious task and the reader is referred to Greenspan for details. Let it suffice to say that the experimentally-obtained decay rates agree well with theory [2]. Another important feature, revealed by boundary-layer analysis, is that the Ekman layer blows up at the critical angles sending inertial waves into the flow interior. Although the effect of these internal layers is small in the linear theory, their effect might become dominant at very small Ekman numbers when non-linear effects are considered.

We end noting that the modes just described are not standing oscillations of the fluid but rather *traveling* modes in the azimuthal direction; their angular propagation speed (or angular drift as we refer to it later in this thesis) is ω/m . Another important fact is that the energy of these inertial oscillations is entirely

kinetic as Coriolis forces perform no work, a consequence of being fictitious forces.

2.5 Over-reflection

In this section we will briefly review the conditions for over-reflection of a plane sound wave of the form $e^{i(\mathbf{k}\cdot\mathbf{r}-\omega t)}$, incident on a tangential discontinuity in a homogeneous, compressible medium. The formulae obtained here are the basis for the excitation mechanism proposed in [14] and [13]. Consider the situation as shown in Figure 2.2, where the medium at rest is in the region $z < 0$ and the medium at $z > 0$ moves with uniform velocity $\mathbf{v} = v\hat{\mathbf{x}}$. A plane wave with wave vector \mathbf{k} is incident on the boundary, and forms an angle θ with the z axis; the projection of \mathbf{k} on the xy plane forms an angle ϕ with \mathbf{v} . There will be a refracted and a reflected wave. The respective amplitudes can be obtained from continuity conditions on the pressure, and the vertical displacement of fluid elements on either side of the boundary.

If the incident wave has unit amplitude, then the pressure amplitude A of the reflected wave and the pressure amplitude B of the refracted wave are given by

$$A = \frac{k_z(\omega - k_x v)^2 - \kappa\omega^2}{k_z(\omega - k_x v)^2 + \kappa\omega^2}, \quad B = 1 + A \quad (2.24)$$

where we have assumed the incident wave vector $\mathbf{k} = k_x\hat{\mathbf{x}} + k_y\hat{\mathbf{y}} + k_z\hat{\mathbf{z}}$, the reflected wave vector $\mathbf{k}_A = k_x\hat{\mathbf{x}} + k_y\hat{\mathbf{y}} - k_z\hat{\mathbf{z}}$ and the refracted wave vector $\mathbf{k}_B = k_x\hat{\mathbf{x}} + k_y\hat{\mathbf{y}} + \kappa\hat{\mathbf{z}}$. The Mach number M is defined as v/c where c is the phase speed of the sound waves. The expression for κ is

$$\kappa^2 = \frac{\omega^2}{c^2} [(1 - M \cos \phi \sin \theta)^2 - \sin^2 \theta]. \quad (2.25)$$

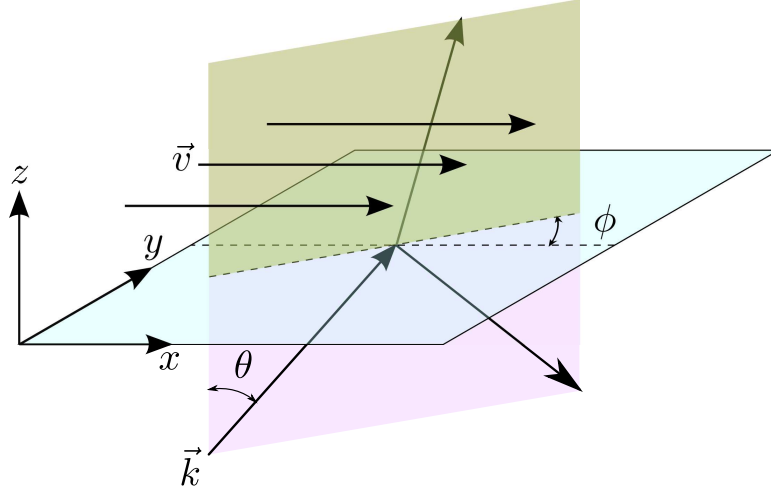


Figure 2.2: A plane sound wave is incident from below on the boundary between two identical media. The medium at $z < 0$ is at rest and the medium at $z > 0$ moves at a uniform velocity \mathbf{v}

It can be shown that if

$$\frac{1 + \sin \theta}{\sin \theta \cos \phi} < M, \quad (2.26)$$

then $A > 1$, and the reflected wave is stronger than the incoming one, having extracted energy from the relative motion of the two media. For this to be the case we need $M > 2$. Moreover, the denominator in 2.24 might become small or zero for certain incidence angles as long as $M > 2$, thus providing infinite amplification of an incoming wave. Note that it is necessary that $\phi \neq \pm\pi/2$, otherwise condition 2.26 cannot be met.

As mentioned earlier, in [14] and [13] an over-reflection mechanism is suggested to explain the excitation of shell modes that are closely related to the full sphere modes described in the previous section. It is *postulated* that the incidence angle corresponds to the critical angle θ_c . The phase speed c is identified with the angular

drift speed ω/m . Since each mode has a corresponding critical angle, it is argued that some modes will get amplified while others will not. We will get back to this topic in the discussion section of Chapter 6.

2.6 A precessing spheroid

Let us now consider a spheroidal container with ellipticity η , rotating with angular velocity $\boldsymbol{\omega}_c = \omega_c \hat{\mathbf{z}}$ but this time also precessing with angular velocity $\boldsymbol{\Omega}_p$. In the precessing frame of reference both the rotation axis of the container and the precession axis remain constant in space; see Figure 2.3. If we use $\omega_c L$ as the scale for the fluid velocity (Rossby number $Ro = 1$) the dimensionless Navier-Stokes equation in this frame is

$$\frac{\partial \mathbf{u}}{\partial t} + (\mathbf{u} \cdot \nabla) \mathbf{u} + 2\boldsymbol{\Omega} \times \mathbf{u} = -\nabla p + E \nabla^2 \mathbf{u}, \quad (2.27)$$

where $\boldsymbol{\Omega} = \boldsymbol{\Omega}_p / \omega_c$. The norm of $\boldsymbol{\Omega}$ is the Poincaré number.

The overall torque balance in steady state ($\partial_t \mathbf{u} = 0$) can be obtained from (2.27) by taking the cross product of \mathbf{r} on both sides and integrating over all the fluid volume. With the help of the divergence theorem and Green's first identity we can show that

$$\int \mathbf{r} \times (\mathbf{u} \cdot \nabla) \mathbf{u} \, dV = \int_{\partial V} (\mathbf{r} \times \mathbf{u})(\mathbf{u} \cdot \hat{\mathbf{n}}) \, d\Sigma, \quad (2.28)$$

$$\int \mathbf{r} \times \nabla p \, dV = \int_{\partial V} p \mathbf{r} \times \hat{\mathbf{n}} \, d\Sigma, \quad (2.29)$$

$$E \int \mathbf{r} \times \nabla^2 \mathbf{u} \, dV = \int_{\partial V} \{ \mathbf{r} \times (\hat{\mathbf{n}} \cdot \nabla) \mathbf{u} - \mathbf{u} \times \hat{\mathbf{n}} \} \, d\Sigma, \quad (2.30)$$

where $\hat{\mathbf{n}}$ stands for the normal unit vector to the bounding surface Σ . If we take

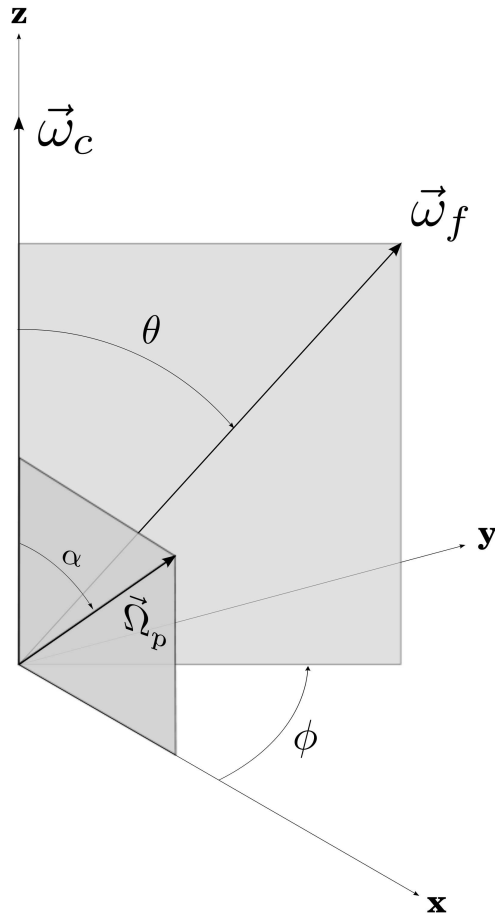


Figure 2.3: The Cartesian coordinate system fixed in the precessing (or laboratory) frame. The z axis is chosen along the rotation axis. $\vec{\Omega}_p$ is the precession vector and $\vec{\omega}_f$ is the fluid-spin axis.

into consideration the whole fluid, including the thin boundary layer, we see that the first integral vanishes, given the no-penetration boundary condition. This has a very important physical meaning: the torque in the bulk of the fluid due to precession is balanced by the pressure and viscous torques exerted by the boundary alone. Obviously, the pressure torque for a perfect spherical boundary vanishes identically; only viscous torques are exerted by the boundary.

If the viscous decay constant is known, the torque balance determines the solution [35]. According to Busse [5] the steady-state solution is composed of a uniform vorticity flow in the fluid interior and a thin boundary layer that matches the no-slip boundary conditions. The angular velocity vector of the fluid interior $\boldsymbol{\omega}$ in the precessing frame can be determined from the implicit relation

$$\frac{\boldsymbol{\omega}}{\omega^2} = \hat{\boldsymbol{z}} + \frac{A\hat{\boldsymbol{z}} \times (\boldsymbol{\Omega} \times \hat{\boldsymbol{z}}) + B(\hat{\boldsymbol{z}} \times \boldsymbol{\Omega})}{A^2 + B^2}, \quad (2.31)$$

where A and B are defined as

$$A = 0.259\sqrt{\frac{E}{\omega}} + \eta\omega^2 + \boldsymbol{\Omega} \cdot \hat{\boldsymbol{z}}, \quad B = 2.62\sqrt{E\omega}.$$

Expression 2.31 describing $\boldsymbol{\omega}$ is valid as long as $1 - \omega^2 \ll 1$. Note that $\boldsymbol{\omega} \cdot \hat{\boldsymbol{z}} = \omega^2$, which is known as the no spin-up condition. It means that the component of the angular velocity of the shell parallel to the fluid axis is equal to the angular speed of the fluid, thus no Ekman pumping will occur. Note also that there is a uniform azimuthal flow as seen in the rotating shell frame, since $\boldsymbol{\omega} \cdot \hat{\boldsymbol{z}} \neq 1$.

In the shell frame of reference, the uniform vorticity flow described by equation (2.31) is seen as a uniform rotation around a horizontal axis that precesses around the z axis plus a small uniform azimuthal flow. The flow field \boldsymbol{u} in the rotating

(mantle) frame is related to the fluid rotation vector $\boldsymbol{\omega}$ in the precessing (lab) frame through

$$\mathbf{u} = (\boldsymbol{\omega} - \hat{\mathbf{z}}) \times \mathbf{r}. \quad (2.32)$$

In cylindrical coordinates, the z component of \mathbf{u} at a point (s_0, z_0, ϕ_0) is

$$u_z(s_0, z_0, \phi_0) = s_0 \frac{\omega^2 \Omega \sin \alpha}{\sqrt{A^2 + B^2}} \sin(t - \phi + \phi_0), \quad (2.33)$$

independent of z_0 . We just have to multiply the above expression by $\omega_c L$, the velocity scale, to get dimensional units. The angle θ between the fluid rotation vector $\boldsymbol{\omega}$ and the z axis satisfies

$$\tan \theta = \frac{|\Omega \sin \alpha|}{\sqrt{A^2 + B^2}}. \quad (2.34)$$

This angle can be determined directly from the amplitude of u_z if we set $\omega = 1$ in 2.33, which we are allowed to given the range of validity of 2.31.

The thin Ekman boundary layer allows the no-slip boundary condition to be met. It turns out that this boundary layer is not thin everywhere on the boundary; it has a divergence in the inviscid limit at the critical latitudes, which are located near $\pm 30^\circ$ from the equator for small Poincaré numbers. For finite viscosity this manifests itself in the form of internal shear layers that are actually inertial waves penetrating into the fluid, spawned by the thickening of the Ekman layer at those critical latitudes. These shear layers are contained in cones aligned with the fluid rotation axis, not the rotation axis of the ellipsoidal container. They undergo multiple reflections on the boundary, and may form a closed circuit as discussed above. Internal shear layers of this kind are ubiquitous in enclosed rotating flows; they are

not restricted to the spin-over mode excited by precession. It is believed that the inclusion of an inner core would have a negligible effect on the solution described above if the core has the same ellipticity as the spheroidal container. Assuming spherical boundaries, the frictional torque of a core with diameter 0.35 times the diameter of the outer sphere can be estimated to be only 2% of the total frictional torque (see Tilgner).

Although the path followed by a fluid particle is not simple (see Pais and LeMouel), the velocity profile along a vertical line is flat, and oscillates with the rotation frequency. To see this, consider a uniformly-rotating flow with constant vorticity $\boldsymbol{\omega}$, such that the velocity is $\boldsymbol{v} = \boldsymbol{\omega} \times \boldsymbol{r}$. Imagine we are measuring the velocity *along* a straight line B with a particular direction $\hat{\boldsymbol{b}}$ in space, starting from a fixed point \boldsymbol{r}_0 . Using s as a parameter, any point in B is

$$\boldsymbol{r}_B = \boldsymbol{r}_0 + s\hat{\boldsymbol{b}}, \quad (2.35)$$

The velocity measured along B has magnitude u given by

$$u(\boldsymbol{r}_B) = \hat{\boldsymbol{b}} \cdot \boldsymbol{v} = \hat{\boldsymbol{b}} \cdot (\boldsymbol{\omega} \times \boldsymbol{r}_B) \quad (2.36)$$

$$= \boldsymbol{r}_B \cdot (\hat{\boldsymbol{b}} \times \boldsymbol{\omega}) \quad (2.37)$$

$$= \boldsymbol{r}_0 \cdot (\hat{\boldsymbol{b}} \times \boldsymbol{\omega}). \quad (2.38)$$

The measured velocity u is then independent of the parameter s . Therefore the velocity profiles along straight lines in a fluid with uniform rotation are flat.

Chapter 3

Design and construction

3.1 Overview

Given a suitable flow configuration, the dynamo instability occurs if the magnetic Reynolds number¹ Rm exceeds some critical value. In order to increase our chances of observing a dynamo instability, we want Rm to be as large as possible. This can be done by increasing the kinetic energy of the flow, by increasing the size of the experiment, or by minimizing the magnetic diffusivity η (which amounts to using a fluid with the highest feasible electrical conductivity). The size of the 3m device was the largest size of a spherical vessel that could still fit through the doors of the lab housing the experiment. The next step was to produce a feasible experimental design while reaching a compromise among achievable speed ranges, experimental versatility and safe operation.

With versatility in mind, we wanted a big opening on top of the vessel allowing for replacement of the the forcing package. Encouraged by some experiments performed with the 30 cm device, the initial design incorporated two counter-propagating marine propellers on a vertical shaft. Although efficient in providing

¹The magnetic Reynolds number Rm is defined as UL/η , where U is the typical velocity scale of the flow, L is the radius of the fluid-containing cavity and $\eta = (\mu_0\sigma)^{-1}$ is the magnetic diffusivity (μ_0 is $4\pi \times 10^{-7}$ and σ is the electrical conductivity).

kinetic energy to the flow, the propellers would render the experiment entirely intractable to numerical simulations. By using an inner sphere, we would enormously simplify the boundary conditions, therefore bringing the flow closer to the capabilities and interests of numericists. Additionally, it would make the design simpler, as the counter-rotating propeller design required two independently-rotating concentric shafts and not just one as the inner sphere required. We should mention that the two-propeller design or other designs are still possible toward the future.

The design of the rotating vessel had extensive feedback from James Weldon, an expert in designing heavy rotating machinery and whom Prof. Lathrop, director of this thesis, has always consulted with regarding earlier rotating experiments.

3.2 The main vessel

The vessel's largest outer diameter, including its jacket, is 3042 mm, as determined by the size of the door to the high bay area in the Energy Research Building housing the experiment. Stainless steel (type 304L) was the material chosen, given its known compatibility with liquid sodium and its non-magnetic character. A preliminary vessel design was evaluated by Pressure Sciences Inc., a Pittsburgh-based company, using finite element analysis, and it was determined that the vessel design met the ASME code requirements for boiler and pressure vessels, if spun at 4 Hz or less. The spherical vessel was then built in accordance to our specifications by Central Fabricators Inc, a Cincinnati-based company. Figure 3.1 shows a picture of the vessel during fabrication. We required full radio-graphical inspection of all



Figure 3.1: The vessel started out as several pieces of 1" (2.54 cm) thick stainless steel blanks, individually cold pressed to conform to a spherical surface, and then welded together to form two hemispheres and then a sphere.

welds and ASME certification as a pressure vessel. The vessel with its original lid was rated to 125 psi (861845 Pa) at 400°F (204.44°C).

To keep sodium molten at an appropriate temperature we require a thermal jacket, consisting of 2" size, schedule 40 stainless steel half-pipe, welded around the outer surface of the vessel in six spiral segments. Two manifolds provide the inlet and outlet connections to all segments (see figure 3.2). The manifolds are piped to the bottom head, providing both support for the whole vessel and a concentric connection to a rotary union. Flexible stainless steel hoses connect the rotary union

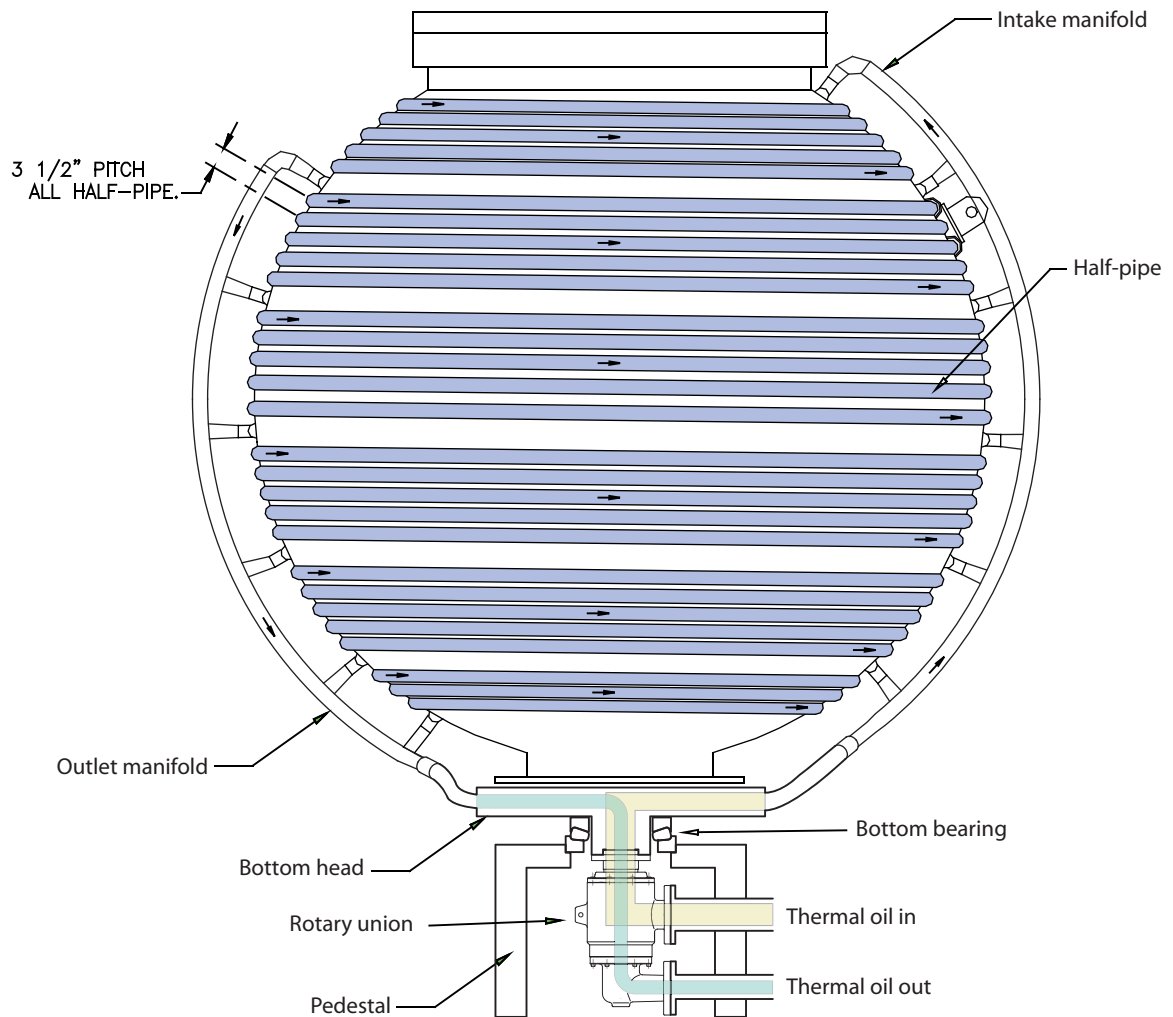


Figure 3.2: The half-pipe jacket allows thermal control of the vessel, keeping sodium molten at the right temperature. The rotary union provides the stationary connections to the cooling system outside the building.

to the cooling system located outside the building. The cooling jacket can hold up to 60 psig (413685 Pa above atmospheric pressure). We will describe the rest of the cooling system in an upcoming section.

We wanted to be able to remove and reinsert the forcing package (shaft and inner sphere) with the vessel full of fluid (water or sodium). For that purpose, a bayonet coupler at the bottom of the vessel was incorporated in the design to keep the forcing package shaft from having any motion in the (cylindrical) radial direction, while allowing the shaft to be removed or inserted freely. The geometrical tolerances diagram (figure 3.3) shows the bayonet location at the bottom of the vessel. The tip of the bayonet is within 2.54 mm from the vessel principal axis as determined by our own measurements. We manually adjusted (with some hydraulic power!) the position of the vessel on the bottom head until the tip of the bayonet was less than 2 mm away from the rotation axis.

3.2.1 Shape of the vessel cavity

The true shape of the vessel lies between two hypothetical concentric spherical surfaces whose diameters differ by less than 13 mm, according to original specifications. In order to have more detailed information about the cavity's shape, we undertook measurements using a compact laser range finder (Leica Disto D2) with 1 millimeter accuracy. Using the top flange as a base line, we measured distances on equally spaced (azimuthally) meridional planes from the top flange to corresponding points at different latitudes on the inner surface. Figure 3.4 shows a diagram of

the distances measured. Four additional measurements were taken manually on the concave dish under the top lid.

The set of $N = 116$ distance measurements were translated into a set of spherical $\{r_i, \theta_i, \phi_i\}$, $i = 1, \dots, N$ coordinates in order to calculate a least squares fit in a spherical harmonics expansion. If we go up to $l = 5$, we will have $M = (l + 1)^2 = 36$ different spherical harmonics:

$$r(\theta, \phi) = \sum_{l=0}^5 \sum_{m=-l}^l A_{lm} Y_l^m(\theta, \phi).$$

By using a single index j to denote a specific spherical harmonic function or coefficient we can write

$$r(\theta, \phi) = \sum_{j=1}^M A_j Y_j(\theta, \phi).$$

The *design* matrix X is then built with elements

$$x_{ij} = Y_j(\theta_i, \phi_i); \quad i = 1, \dots, N; \quad j = 1, \dots, M$$

The vector \mathbf{A} of coefficients A_j constituting the least squares fit (for details see [31]) can be calculated as

$$\mathbf{A} = (X^T X)^{-1} X^T \mathbf{r},$$

where \mathbf{r} is the vector of r_i measurements (N total). The design matrix X turns out to be rank deficient when the spherical harmonic expansion is carried out beyond $l = 5$. The ten largest coefficients (in magnitude) obtained this way are listed on Table 3.1.

We can see many contributions to the shape besides the spherical Y_0^0 . For comparison a perfect oblate or prolate ellipsoid would have Y_0^0 and Y_2^0 contributions

Table 3.1: Vessel shape and its spherical harmonic coefficients.

l	m	A_{lm} (in mm)
0	0	5172.7
3	0	7.1
2	2	4.9-1.3 <i>i</i>
2	1	-2.1+4.4 <i>i</i>
5	0	3.9
4	0	-3.7
2	0	-3.5
1	0	-3.2
4	2	1.9+0.1 <i>i</i>
3	1	1.4-0.9 <i>i</i>

only. A prolate (oblate) ellipsoid would have A_{20} real and positive (negative). We expect, in principle, that the A_{20} coefficient will be one of the most affected, becoming more negative, due to centrifugal forces as the rotation rate of the vessel is increased. The standard deviation of the measurements relative to the spherical expansion model is 2.1 mm. Therefore the model misses some topographical features, but it does a good job overall considering that the measurement accuracy is just 1 mm. Figure 3.5 shows cross sections of the vessel for different meridian planes as calculated from the spherical harmonics expansion model.

3.3 Forcing Package

In this section we will describe the forcing package and the top lid that supports it. As we mentioned earlier, the forcing package went through several design iterations before we settled on a design involving an inner sphere mounted on a vertical shaft. The diameter of the inner sphere was chosen so that the diameter ratio

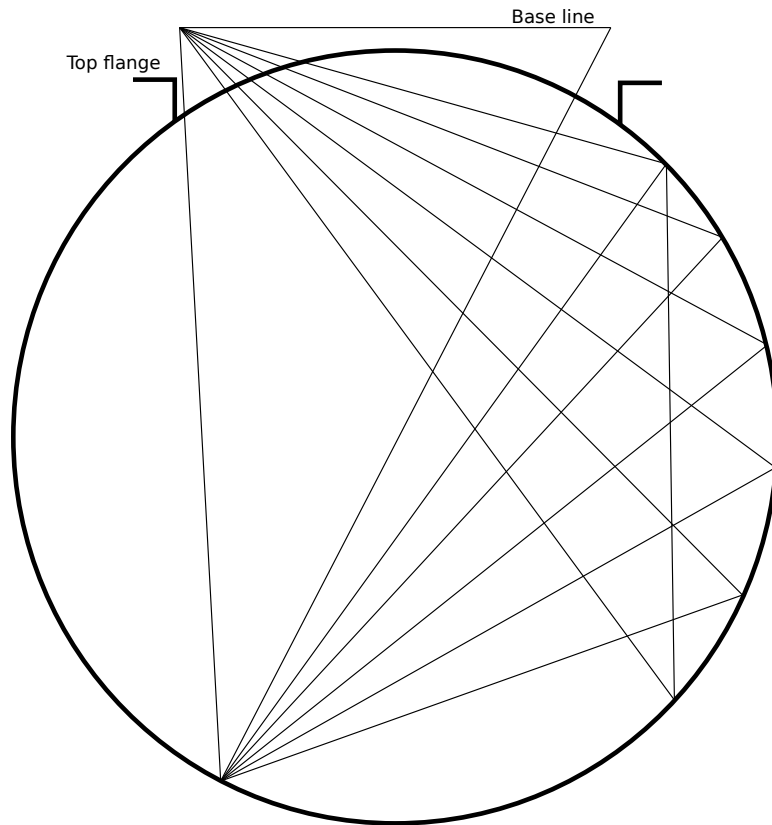


Figure 3.4: Schematic view of the different distance measurements taken inside the vessel to determine its approximate shape. The same set of measurements were taken on different meridional planes around the vessel.

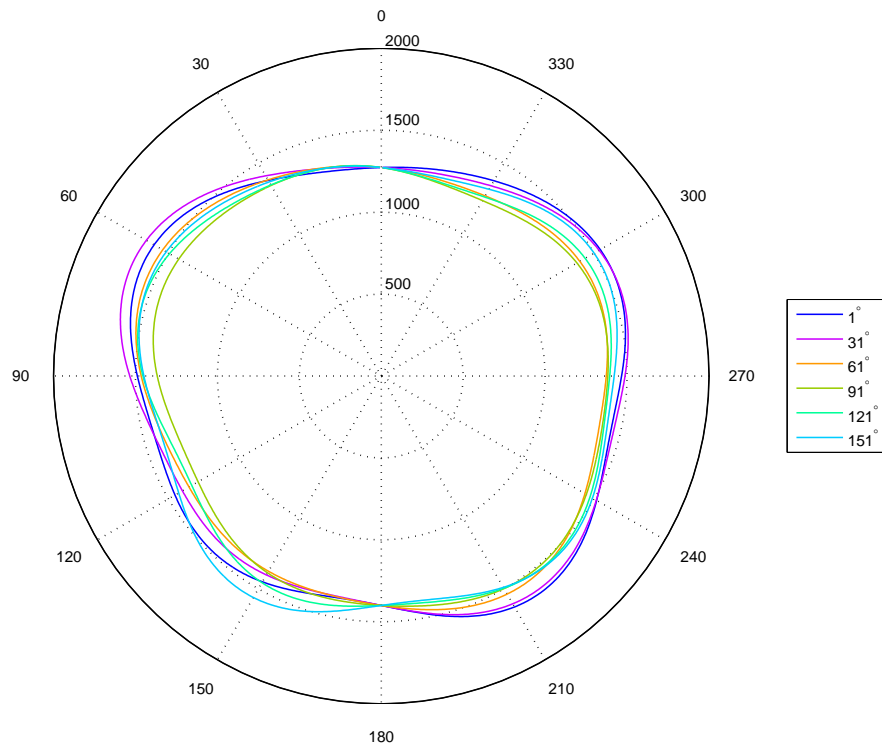


Figure 3.5: Meridional cross sections of the vessel as calculated from the spherical harmonics expansion (deviations from mean radius are exaggerated 20X). Each color corresponds to the angle between North and the corresponding meridional plane. Numbers along the vertical radius line indicate the radius of the vessel in mm

between the inner and the outer sphere is close to the diameter ratio of the inner core of the Earth to the diameter of the core-mantle boundary (CMB) (see figure 3.6). Originally we planned to have a solid inner sphere made out of either copper, stainless steel or aluminum to mimic more closely the electrical boundary conditions on the Earth's inner core. Unfortunately, no manufacturer considered it feasible to make such an object. We opted for a design involving a hollow inner sphere; this also proved difficult but not impossible. First, two stainless steel hemispheres (6.35 mm thick, 1016 mm diameter) were spin formed (by an external company), and two holes at the poles of the hemispheres were cut (in house). We then welded a cylindrical sleeve providing rigid support and attachment to the shaft (see figure 3.7).

The shaft started as a solid 6.5"-diameter stainless steel round bar. We decided to have a 3" hole drilled almost all the way to the opposite end of the shaft, to eliminate unnecessary weight while maintaining stiffness. This hole also allows for placing instrumentation at the vessel's center, but not in contact with the fluid. The shaft was then machined to incorporate two bearing seats, one for the top shaft bearing and one for the bayonet coupler bearing. An additional piece was welded around the shaft to act as the inner sphere seat.

The shaft can vibrate at its natural frequency when spinning. The rotational speed of the shaft equal in value to the natural frequency is called the *critical speed*. Its value is important since it determines a speed (or range of speeds) that should be avoided to prevent unwanted vibrations. We can make an estimate of the natural

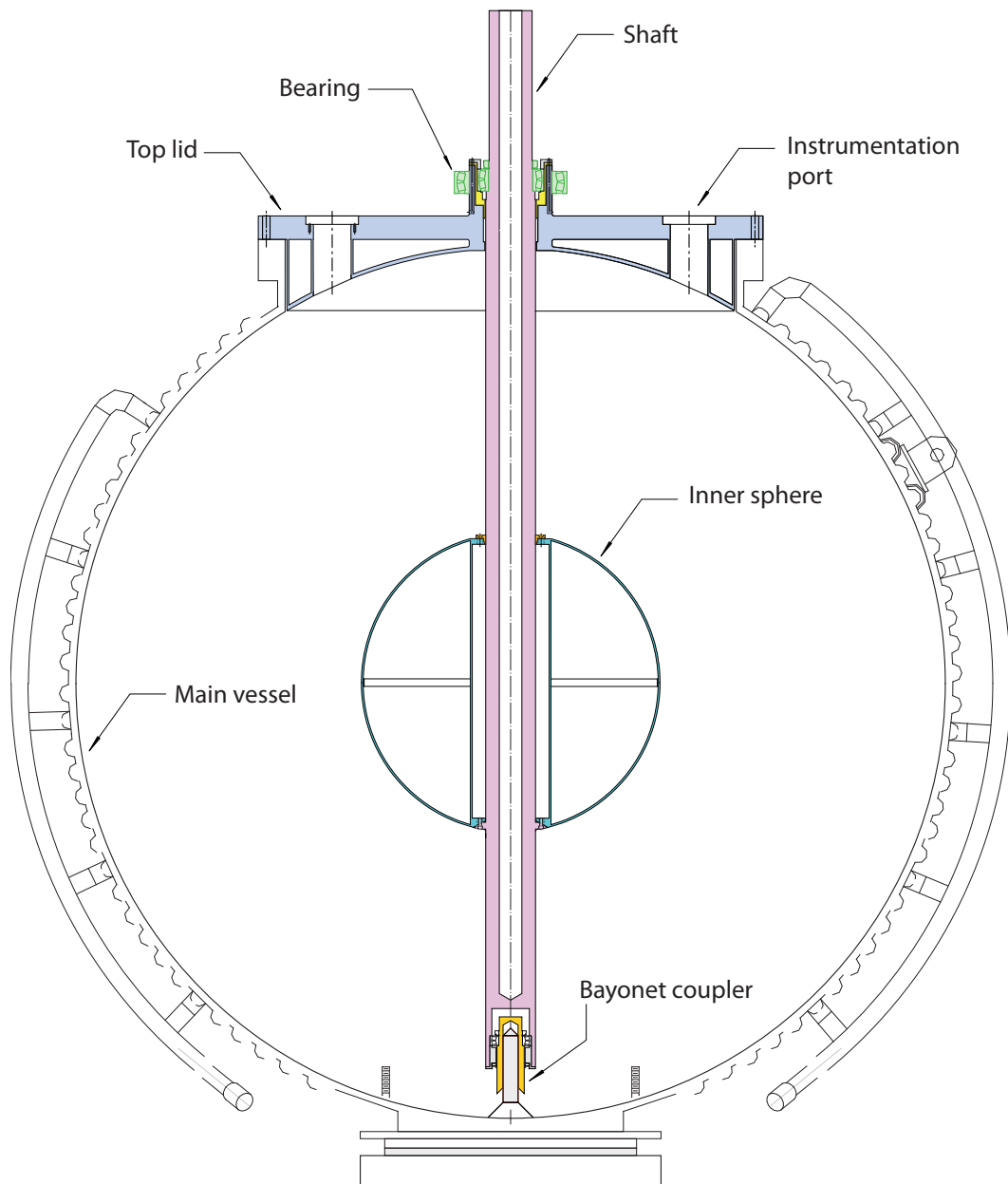


Figure 3.6: Vessel cross section with the inner sphere and shaft. Main top bearing attaches to the support frame (not shown). The top lid supports the shaft and the bayonet coupler keeps the bottom end of the shaft from (cylindrical) radial displacements. The inner sphere has 1016 mm in diameter and the diameter of the inner surface of the outer sphere is 2920 mm; their ratio is 0.348, very close to the ratio (0.35) of the Earth's inner core and the diameter of the core-mantle boundary.

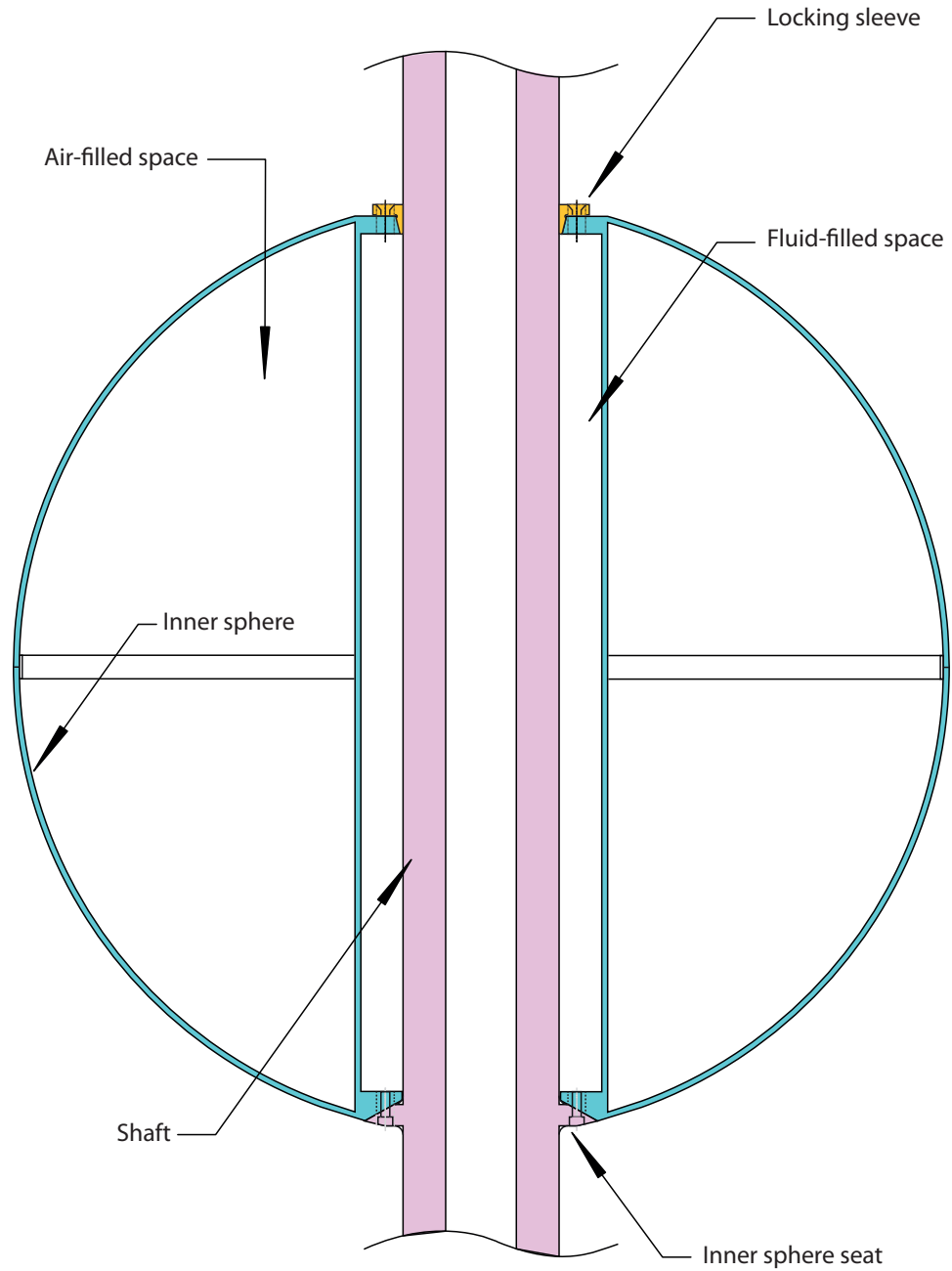


Figure 3.7: Cross section of the inner sphere and shaft. The gap between the inner sphere and the shaft is open (via several holes, not shown) so that fluid fills the space. The inner sphere can be removed from the shaft by removing the locking sleeve and the bolts on the inner sphere seat.

frequency of the shaft, assuming it is simply supported on both ends, by using:

$$f = \frac{1}{2\pi} \sqrt{\frac{3El\pi(r_o^4 - r_i^4)}{4a^2b^2(m_{is} + \frac{1}{2}m_{shaft})}}, \quad (3.1)$$

where E is the modulus of elasticity of 304L stainless steel, l is the length of the shaft, r_i and r_o are the inner and outer radii of the shaft, m_{is} is the mass of the inner sphere, a is the distance from one end of the shaft to the center of the inner sphere and $b = l - a$. The mass of the inner sphere is about 250 kg and the mass of the shaft is close to 450 kg. This results in a natural frequency of about 240 Hz, high enough not to be of any concern while spinning the inner sphere. Actually, the limits on the inner sphere speed are imposed by the stresses due to rotation on the equatorial weld joining the two hemispheres, and the welds joining the hemispheres to the cylindrical sleeve. D. Zimmerman performed a finite element analysis and estimated that the highest safe speed is 20 Hz [63]. We are not completely certain of the minimum thickness of the welds, but at any rate, the motor driving the inner sphere will run out of power due to turbulent drag at around 12-15 Hz.

The shaft is suspended from the top, with its bottom end free to slide axially on the bayonet. All bearings are of the spherical-roller type, allowing for angular misalignments up to 1.5° , except for the main bottom bearing, which is of the spherical roller thrust type, and is completely separable. The top shaft bearing seats on a piece that allows easy retrieval. In principle, the top shaft bearing can be replaced without the need to extract the shaft from the main vessel (see figure 3.8).

The bottom end of the shaft (see figure 3.9) has a spherical-roller type bearing mounted on the bayonet coupler, allowing spinning. The bayonet coupler is pre-

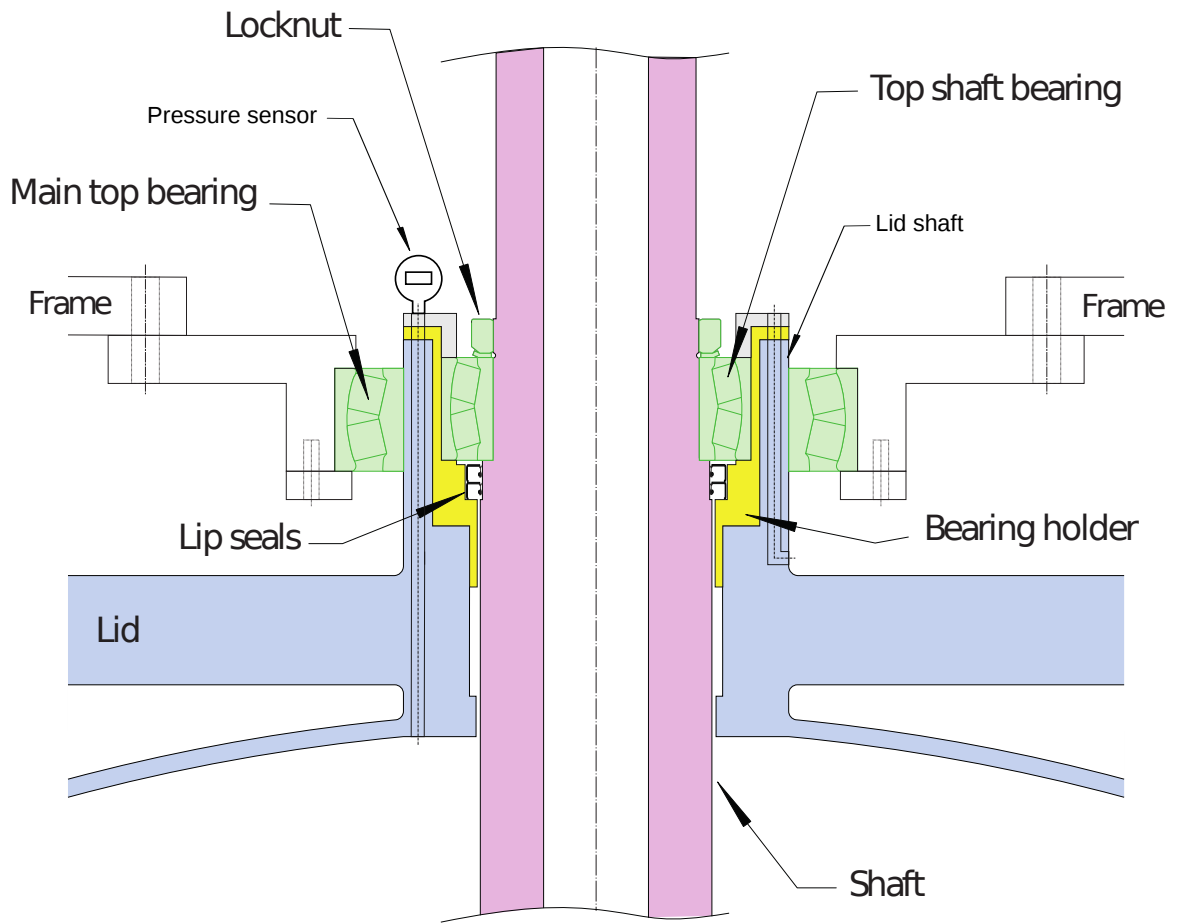


Figure 3.8: Detail of the shaft and its attachment to the lid. The inner race of the main top bearing is free to slide axially on the lid shaft, allowing for thermal expansion of the vessel. The locknut on the shaft, above the top shaft bearing, holds the entire weight of inner sphere and shaft. Two lip seals prevent fluid from leaking into the bearing.

vented from spinning by its six pins (visible in figure 3.10, bottom left). The pins fit tightly around the sides of the bayonet, which has a hexagonal cross section. Since the bayonet coupler and the pins are made out of brass, there is no risk of accidental cold welds or damage to the bayonet during insertion or removal of the shaft. When the experiment was first put together, the bayonet coupler pins were too small in diameter, and after several months of experimental runs, the pins came loose and fell from the bayonet coupler. This translated into unwanted shaft vibrations at certain rotation rates. After successful disassembly of the experiment and modification of the pins, the bayonet coupler now fits snugly on the bayonet. No further vibrational issues have arisen since this modification.

The process of insertion of the shaft (with sphere and lid) into the vessel has to be carried out following a prescribed order. Starting from horizontal, the shaft and sphere are placed vertically next to the frame of the experiment where a specifically designed arm will hold the shaft. Then, the top lid is lowered on the shaft, with the top shaft bearing in place, until the bearing sits properly on the shaft. At this point the locknut can be screwed and tightened in place with two custom-built long-lever wrenches, one to hold the shaft and one for the locknut. Finally, with the lid in place, the whole assembly is inserted into the vessel.

3.4 Motor control

Two 250 kW induction motors drive the main vessel and the inner sphere (for mechanical details see D. Zimmerman's Ph. D. thesis [63]). Current is delivered to

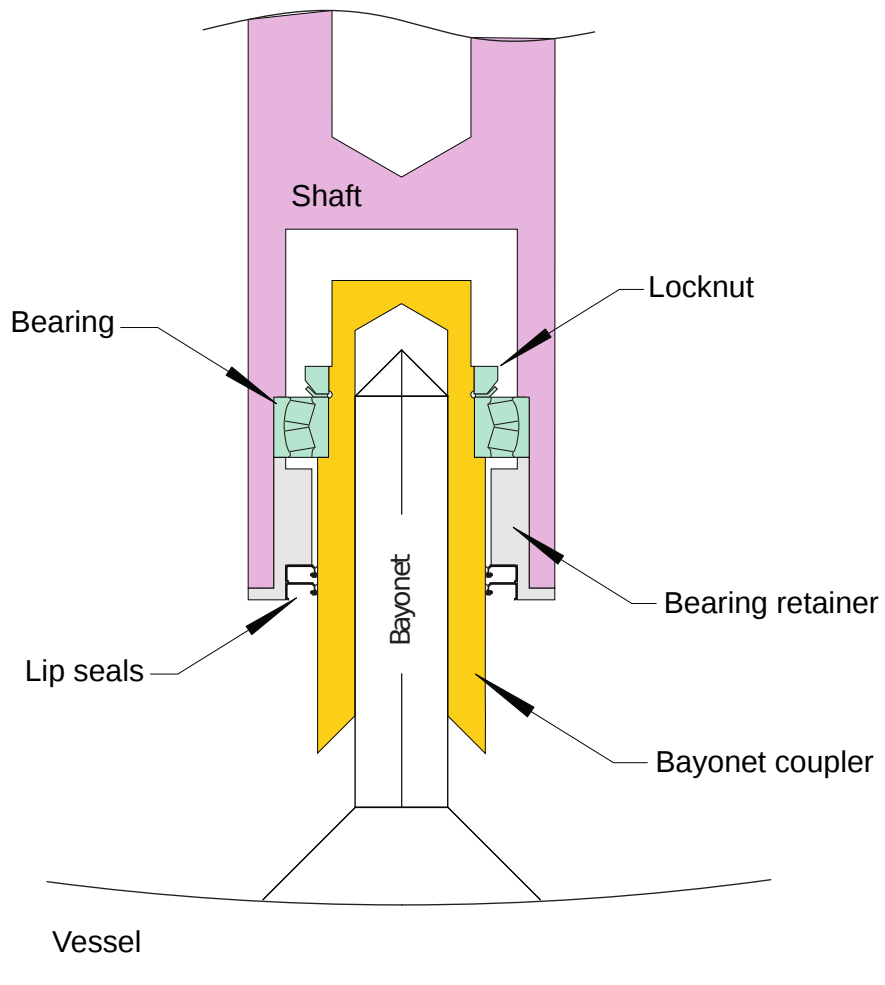


Figure 3.9: Detail of shaft and the bayonet coupler. The bottom end of the shaft can move axially on the bayonet. The bearing retainer and the bayonet coupler are made out of brass, and the bayonet coupler has a chrome coating to protect it from abrasion caused by the lip seals.



Figure 3.10: Bottom bearing retainer during fabrication (top left); bottom end of shaft without the bayonet coupler and some of the machined pieces for the inner sphere (top right); bottom end of shaft, fully assembled (bottom left); shaft and inner sphere being lowered into position (without the top lid) in the main vessel (bottom right).

the motors via a pair of ABB ACH-550 variable frequency drives. Computer control of the motors is achieved by a set of commands sent from a control computer to the variable frequency drives. These commands conform to an industry standard protocol, known as the MODBUS protocol.

Fortunately, the MODBUS protocol is widely documented and royalty-free, which has allowed third-parties to develop open-source software library implementations. The *libmodbus* library, open and designed for Unix-based systems proved useful for our purposes. A Linux computer running a C program (written by the author) using the library, provides a text-based user-interface to command the drives. The physical layer of our implementation of the protocol consists of a RS-485 serial interface, optically isolated, running from the control computer to both variable frequency drives. Optical isolation of the control computer is desirable given the high voltage and current levels in the drives themselves. The control program writes a log file (about 10 times per second) which contains all the relevant (speed, current, etc.) motor and drive parameters. This control program proved reliable, and it is being used in the 60 cm sodium experiment as well. Contrary to the author's initial expectations (as the libraries are provided with no warranty of any kind), the developers (and other users) of the *libmodbus* library were prompt and helpful when we faced programming difficulties.

3.5 Cooling system

We put in place a cooling and heating system to keep the sodium molten at an appropriate temperature ($\sim 105^\circ\text{C}$) during experimental runs. We described earlier the thermal jacket around the main vessel. Now we will describe the rest of the thermal control system.

The system consists of five heat exchangers, a heating tank, a centrifugal pump, and an expansion tank. The heat exchangers were placed on a support frame; the expansion tank, together with the centrifugal pump, rest on a separate frame shared with the ventilation scrubber (described in the next section). The thermal oil used is Shell Thermia C, which can handle temperatures up to 315°C . The pipe connections in and out of the centrifugal pump are flexible stainless steel hoses, preventing vibration in the rest of the system. Pipe connections in and out of the heat exchangers are also flexible stainless steel hoses. At the time of this writing only two of the five heat exchangers are wired electrically. We estimate that the system can provide 500 kW of cooling.

The cooling system is very close to being tested for the first time. Its full operational status is a requirement for the upcoming liquid sodium experiments.

3.6 Ventilation

In case of a sodium fire, the ventilation system will evacuate the caustic smoke from the laboratory room. Outside the building, a centrifugal blower will direct the smoke onto a scrubber, mixing it with fine water droplets, removing most of the

caustic material from the smoke. We undertook the task of building the ventilation system, cleaning and reconditioning the scrubber, and setting up the smoke stack. The scrubber, blower and stack can be seen in figure 3.12.

There will be occasions when cleaning and repairs are needed on the shaft and inner sphere (resting horizontally next to the experiment frame); it is likely that there will be small amounts of solidified sodium in them. To provide adequate ventilation for those tasks, we have put in place four ventilation panels next to the space where the shaft and sphere would rest during maintenance. The panels are also connected to the blower and scrubber outside the building (see figures 3.11 and 3.12).

Although the cooling and ventilation systems were not used during the experimental runs that we will describe in chapters 5 and 6, D. Zimmerman and the author spent a significant amount of their PhD work designing and building those systems. It should be mentioned as well that full computer control is yet to be incorporated into the systems, which will be required for future liquid sodium experiments.



Figure 3.11: Four panels provide ventilation for the designated maintenance area. The panels and the overhead ducts directly above the experiment will evacuate the smoke generated in case of fire, sending it through the outdoor ventilation section (blower, scrubber and stack). Also visible in this picture are the thermal oil pipe connections from the experiment to the cooling system section outside the building.

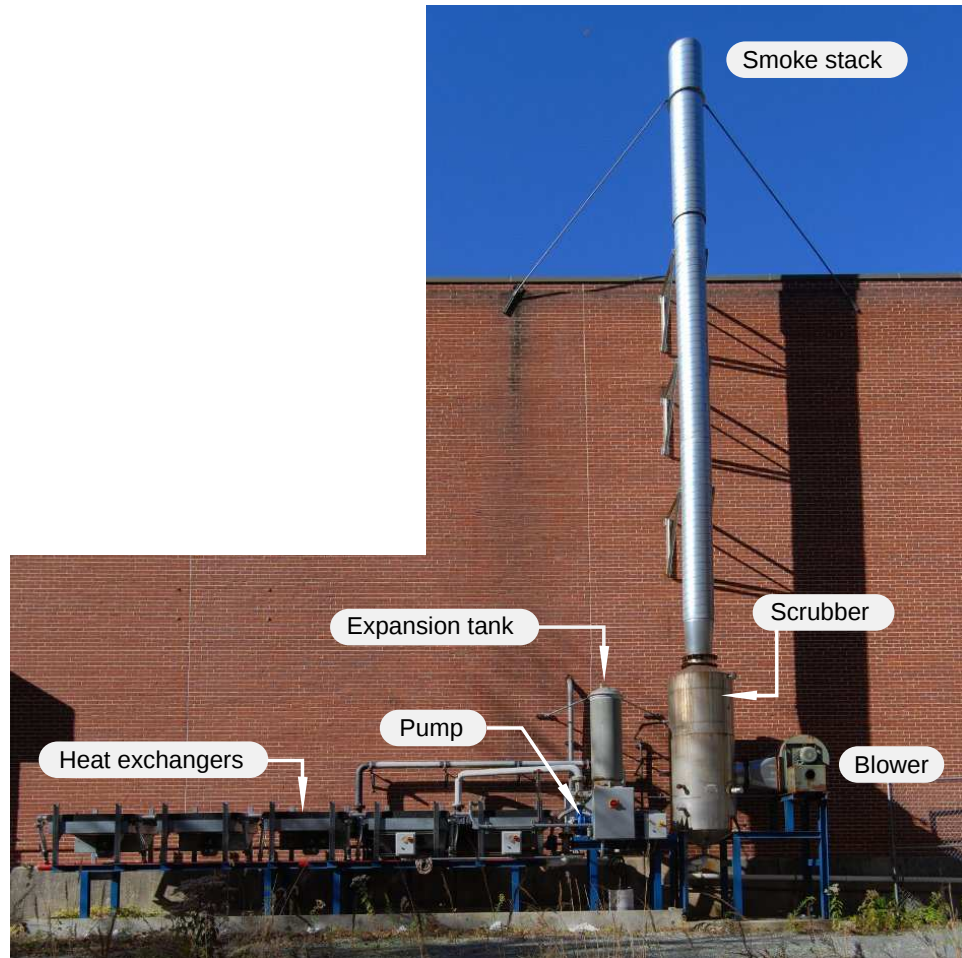


Figure 3.12: Equipment outside the building. All electrical connections and devices are at a height conforming to the building location on the one-hundred-year-flood plain map. The blower extracts air from the building, sending in through the scrubber and the smoke stack. Some components of the vessel's cooling system can be seen as well, except the oil heater which is located between the heat exchangers and the building wall.

Chapter 4

Instrumentation

4.1 Instrumentation ports

The majority of the transducers gathering data from the experiment are located in four instrumentation ports on the top lid. The ports were designed to be removable, and have been modified to accommodate different types of transducers, LED illumination, a camera, and particle and fluorescent dye injectors.

Figure 4.1 shows a stainless steel port with an ultrasound Doppler velocimetry (UDV) transducer and a pressure transducer, both in contact with the fluid. The figure also shows a plastic port (made out of PVC) with a couple of transparent acrylic windows for direct optical visualization. Different port configurations were used during the experimental runs, the configuration shown in figure 4.1 is just an example.

We fabricated a total of seven ports; four are made out of 304L stainless steel, and the remaining three are made out of PVC with transparent acrylic windows. Each port is different, as each incorporates different combinations of instruments. Ports are labeled A through C according to the corresponding opening on the lid where they fit properly. The lid openings are labeled A through C, in the anti-clockwise direction (see figure 4.2). Below is a list of all ports fabricated and their corresponding instrumentation.

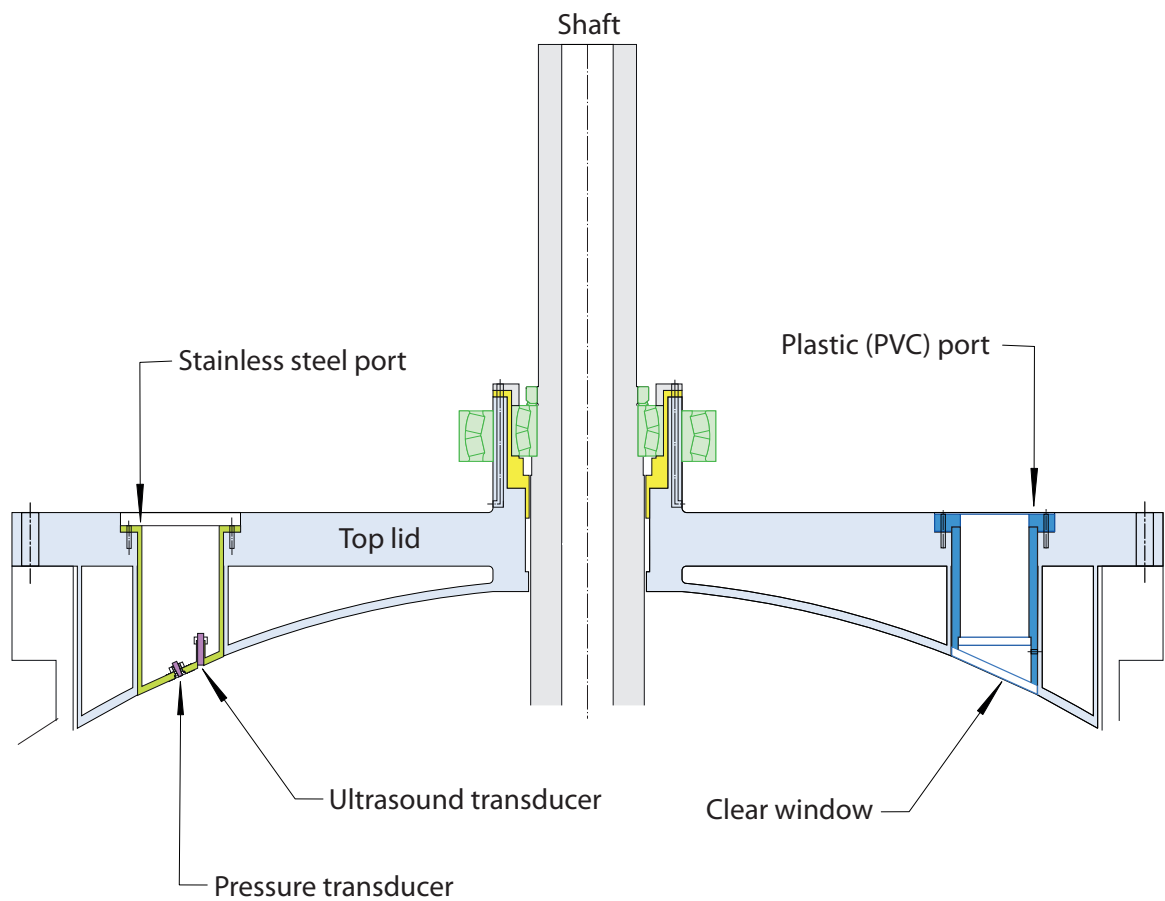


Figure 4.1: The instrumentation ports allow transducers to be in contact with the fluid, like the pressure and ultrasound Doppler velocimetry (UDV) transducers, shown here on the port to the left. For visualization purposes, plastic ports with acrylic windows were made, like the one shown here on the port to the right.

- Stainless steel port A: wall shear stress probe, pressure transducer.
- Stainless steel port B: pressure and UDV transducers.
- Stainless steel port C: pressure transducer.
- Stainless steel port D: pressure and UDV transducers, particle injector, thermocouple.
- Plastic PVC port A: pressure transducer, white LED illumination.
- Plastic PVC port B: camera, fluorescein dye injector, blue LED illumination.
- Plastic PVC port C: pressure transducer, white LED illumination.

In principle, the pressure transducers, thermocouple, and the UDV transducers on the stainless steel ports are able to work in contact with liquid sodium. The plastic ports and visualization devices were made only to be used during the experimental runs with water.

4.2 Pressure Transducers

The pressure transducers used were manufactured by Kistler Corp., model No. 211B5. Their sensing element is composed of a pair of piezo-electric quartz plates, interleaved with gold electrodes. When a force is applied to the element, the quartz plates generate an electric charge proportional to the applied force. Each quartz plate has an equal and opposite acceleration sensitivity as the other, cancelling any acceleration effects. An internal microcircuit converts the net charge into a high level

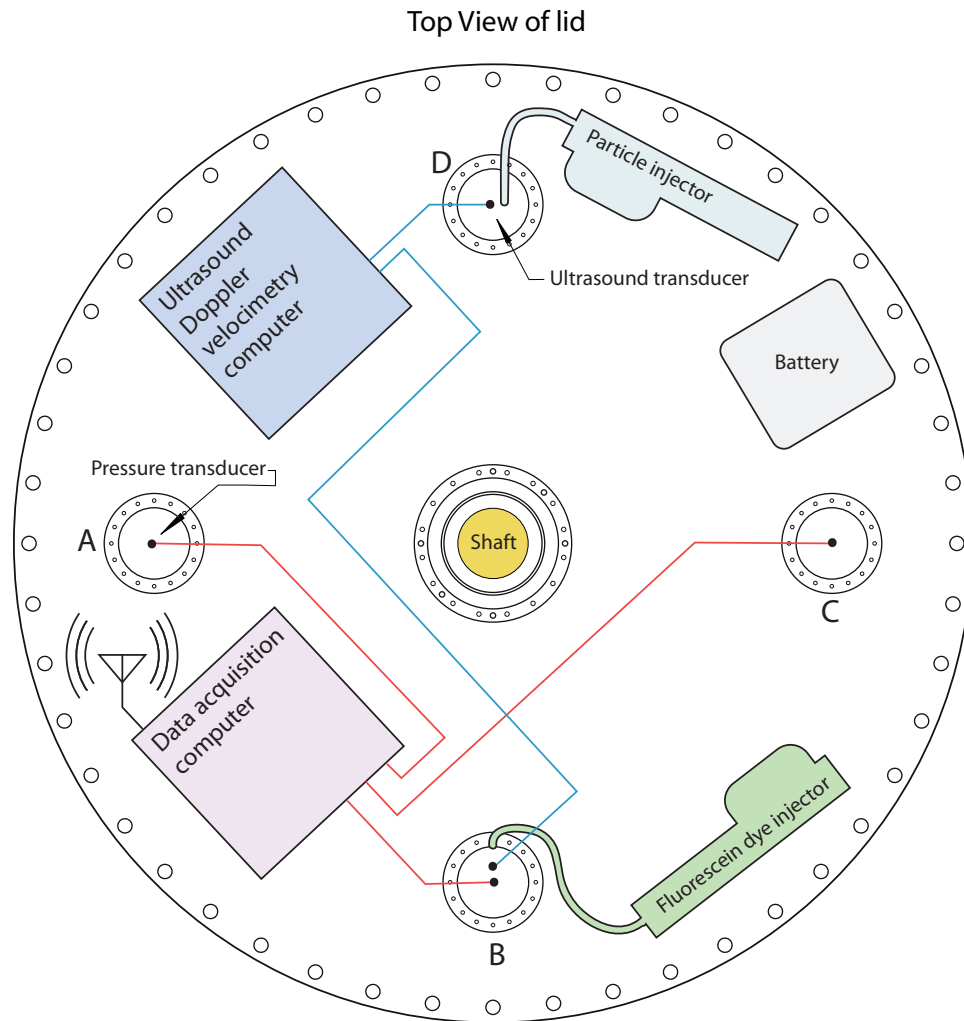


Figure 4.2: Diagram of the instruments on board the rotating vessel, seen from top. Instrumentation ports are labeled A through D. The data acquisition computer collects data from the pressure probes (including the signal from a thermocouple on port D, and a synchronization pulse from an infrared detector, not shown). The data acquisition computer also controls both injectors and serves as an ethernet bridge for the ultrasound Doppler velocimetry computer. Communication with laboratory frame computers is wireless. An on-board battery set provides power to all devices.

voltage signal with low impedance level. Their sensitivity is 7.25×10^{-6} V/Pa. The low-frequency response (-5% point) is 0.025 Hz, suitable for the frequency range of the inertial oscillations, while insensitive to the large constant centrifugal pressure background due to rotation.

A signal conditioning circuit is needed to further amplify and filter the electric signals from the transducers, to a level suitable for the data acquisition computer. For this purpose we designed a three-stage conditioning circuit for each transducer: the first stage powers the pressure transducer via a current source, the second stage amplifies (18.5X) and high-pass filters the signal, and the third stage amplifies (3.7X) and low-pass filters the signal (see electrical diagram in figure 4.3). The $10\mu\text{F}$ capacitors in the conditioning circuit are critical components; low-leakage current capacitors are required in order to keep the overall output level (from an oscillating pressure) within the voltage levels allowed by the data acquisition card.

The transducers turned out to be sensitive to wall shear stresses in the fluid whenever the transducers were not in thermal equilibrium with the fluid. In some cases, e.g. when turbulent mixing allowed the temperature to be more or less constant throughout the fluid, the transducers behaved nominally. During the precession runs (detailed in chapter 5), the flow was orders of magnitude less turbulent than when spinning the inner sphere differentially (chapter 6), and small but noticeable temperature gradients would develop in the fluid, adding a confounding signal to an already weak pressure signal from the flow.

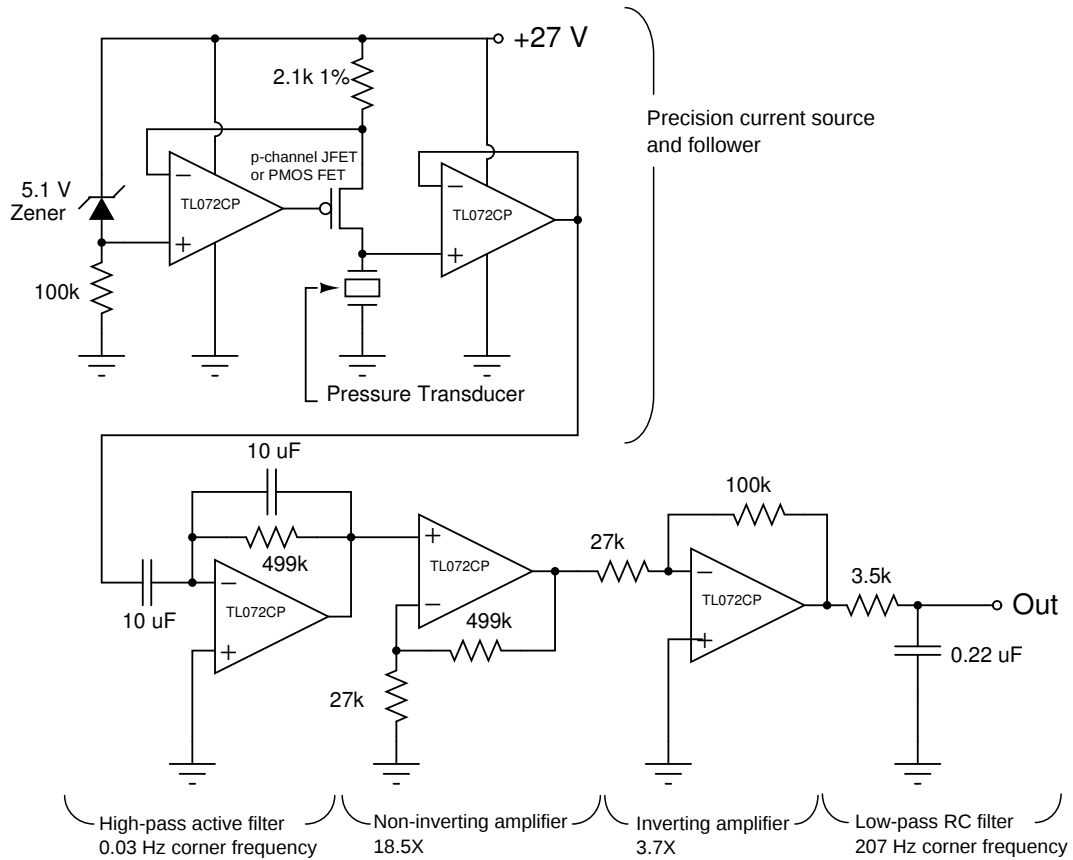


Figure 4.3: Electrical diagram of the conditioning circuit for the pressure transducers. The transducers need to be powered by a constant current source and their voltage is buffered with a high input impedance op-amp in the follower configuration. The voltage output at that point has a large DC component (close to +12 V) that is eliminated with the high-pass active filter (inverting). Subsequent stages amplify and invert the signal, so that the polarity is preserved overall, i.e., an increase in pressure causes a positive increase in the output voltage.

4.3 Ultrasound Velocimetry

Ultrasound velocimetry is a key instrumentation component in the 3m experiment. We acquired a unit (one the most expensive instruments in the system) that in conjunction with appropriate ultrasound transducers, can measure fluid velocities along the ultrasound beam emitted by the transducers. The ultrasound transducer consists of a piezo-electric material which is made to oscillate in the ultrasonic frequency range by applying the appropriate voltage to it. The ultrasound beam is actually a series of ultrasound pulses, whose duration and repetition frequency can be varied. In between two consecutive emission pulses, the transducer ‘listens’ to ultrasound echoes from particles mixed in with the fluid. By measuring the timing of the echoes, the position and velocity of the particles along the beam path can be measured. If the particles are small enough and neutrally buoyant, their velocity will accurately correspond to the flow velocity.

There are a few parameters that have to be considered when using an ultrasound velocimetry device. If F denotes the ultrasound pulse repetition frequency (determined by the hardware), then the maximum measurable depth P_{max} is

$$P_{max} = \frac{c}{2F}, \quad (4.1)$$

where c is the speed of sound. If f_0 is the ultrasound frequency, then the maximum velocity that can be measured is

$$V_{max} = \frac{cF}{4f_0}. \quad (4.2)$$

The product $V_{max}P_{max}$ is constant for a given medium, a given ultrasound probe

(they usually work only at one specific frequency f_0) and a given repetition rate F ,

$$V_{max}P_{max} = \frac{c^2}{8f_0}. \quad (4.3)$$

Another important factor is the minimum particle size, which is about one-fourth of the ultrasound wavelength. Smaller particles will not scatter ultrasound echoes back with enough amplitude to be detected. Another issue not directly related to the ultrasound pulses is the density of the particle material, which should be chosen to be as close as possible to the density of the fluid.

We acquired two 4 MHz ultrasound transducers (one-fourth of the wavelength corresponding to 4 MHz is about $90\mu\text{m}$ in water), and also a 500 kHz transducer ($360\mu\text{m}$ quarter-wavelength). We used polystyrene particles of $120\mu\text{m}$ in (average) size, with 1.05 g/cc density which we liberally mixed in with the fluid. We also used another, slightly smaller, kind of particle ($75 - 106\mu\text{m}$ size range) with better matching density (1.00 ± 0.01 g/cc) to that of water. The latter were considerably more expensive than the former, so we used the more expensive particles exclusively in the injector. In principle, if the particles stay suspended in the fluid, we should be able to measure velocities up to 30 mm/s, all the way from the port to the bottom of the vessel, using the 4 MHz transducers. In practice, this was the case only for precessional forcing at low rotation rates. Reliable velocimetry turned out to be difficult, and only was achieved in general for short distances from the ultrasound probe.

During most of the experimental runs, there was at least one ultrasound transducer on port D, pointing directly down, allowing us to measure flow velocities along

the z direction (at the cylindrical radius of the probe). In some instances we used two ultrasound transducers, one on port D and one on port B (180° apart), both pointing vertically down. We also attempted to use a perpendicular two-ultrasound transducer configuration, where both transducers were located next to each other on port D, in a perpendicular arrangement. In this latter configuration, the angle bisector (of the lines formed with the orientation of both ultrasound transducers) pointed down (in the $-\hat{z}$ direction), so that one transducer pointed East and down (in the $-\hat{\phi} - \hat{z}$ direction), while the other transducer pointed West and down (in the $\hat{\phi} - \hat{z}$ direction).

A particle injector was designed and built by D. Zimmerman to alleviate the problem of degrading ultrasound velocimetry signals due to lack of particles. A few improvements were made by the author. The injector consists of a miniature pump which extracts fluid from the vessel, and sends it through a reservoir, where the fluid mixes with particles (with the aid of a motor stirring a ‘brush’ in the reservoir). Finally, the particle-fluid mix is pumped into the flow (see figure 4.4). We estimate that the injection flow speed is of the order of 10 cm/s, with controlled duration. This evidently affects the flow we are trying to measure, but after 5-10 minutes the flow is back to normal (all injection induced flow has dissipated) and, in the best case scenario, injected particles will stay along the ultrasound beam path.

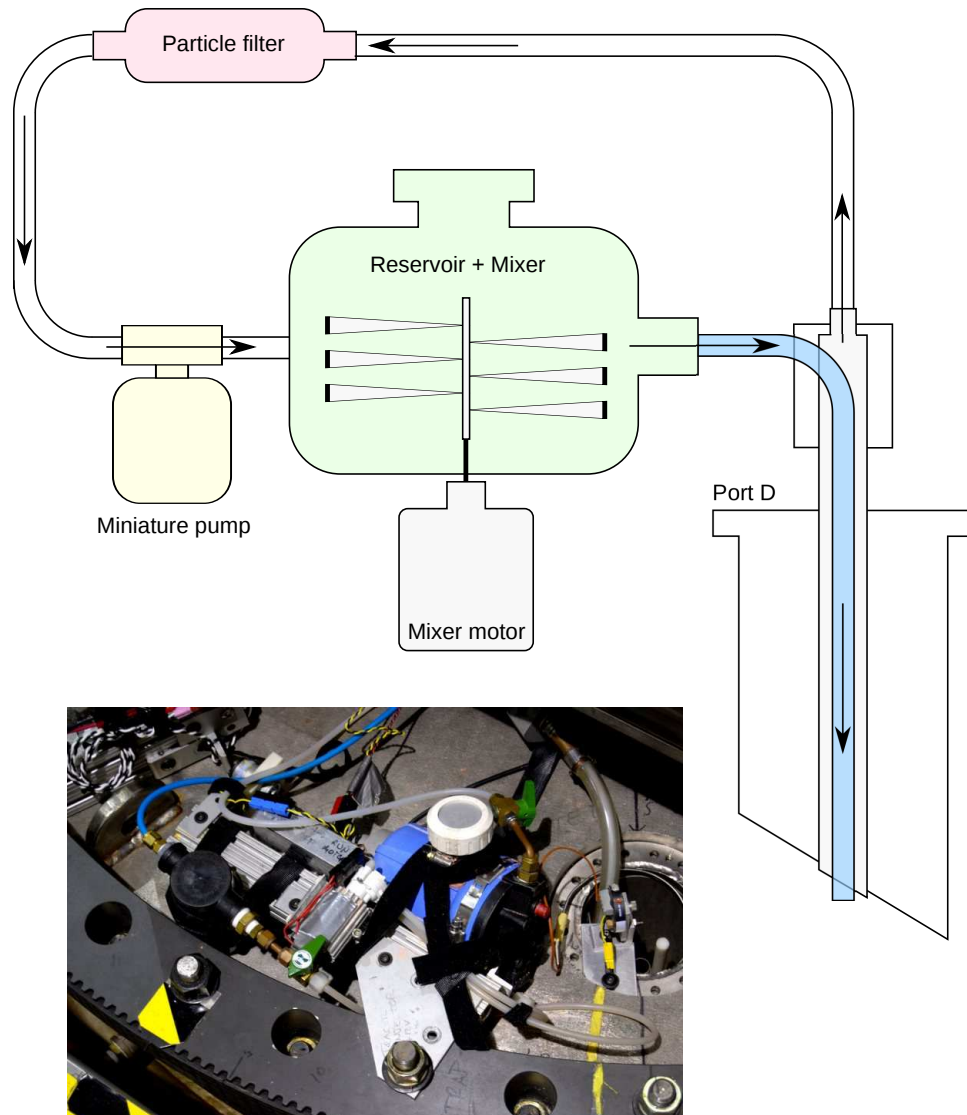


Figure 4.4: Particle injector. Before each experimental run the reservoir was filled with polystyrene particles mixed in a soapy solution. During the run, whenever the ultrasound velocimetry was degrading because of lack of scatterers, we would activate the pump and the mixer motor for a period of 1 to 10 seconds, sending particles into the fluid. The system is closed and eventually, after many injections, the reservoir will have just water and no particles. The inset is a photograph of the actual device. The injector was designed and built originally by D. Zimmerman; a few improvements were made to it by the author.

4.4 Visualization

In order to get a better idea of what the fluid was doing during a given experimental run, we built three plastic PVC ports as mentioned earlier. Two of those ports incorporate a ring of white LEDs providing illumination for a small machine-vision camera (installed in the third plastic port), able to record up to 200 frames per second. The first goal with this system was optical tracking of a small sphere, of about 1.5 cm in diameter, that was being tested by Y. Gasteuil. This sphere was nearly neutrally buoyant and radio-transmitted its acceleration as it moved with the fluid. For a description, we refer the reader to Y. Gasteuil's Ph. D. thesis [8]. The port housing the camera has a special window allowing minimal distortion of the field of view due to refraction with water (see figure 4.5).

Later, we incorporated a fluorescein injector and new blue LED illumination around the camera to visualize the flow directly. Fluorescein is a synthetic organic compound, available in powder form, that when mixed with water or alcohol is optically excited with blue light (absorption peaks at a wavelength of 494 nm) and emits green light (peaked at 521 nm of wavelength). It is widely used in microscopy, generally in conjunction with dye lasers and appropriate filters. In our case, we used nine Cree XR-E blue LEDs with peak intensity at 475 nm of wavelength, in a ring configuration around the camera lens, as can be seen in the inset photograph in figure 4.5. To avoid glare from the acrylic window, we used two optical filters in front of the camera lens, one band-pass filter allowing light with wavelengths of 510-560 nm, and a band-reject filter blocking wavelengths smaller than 512 nm.

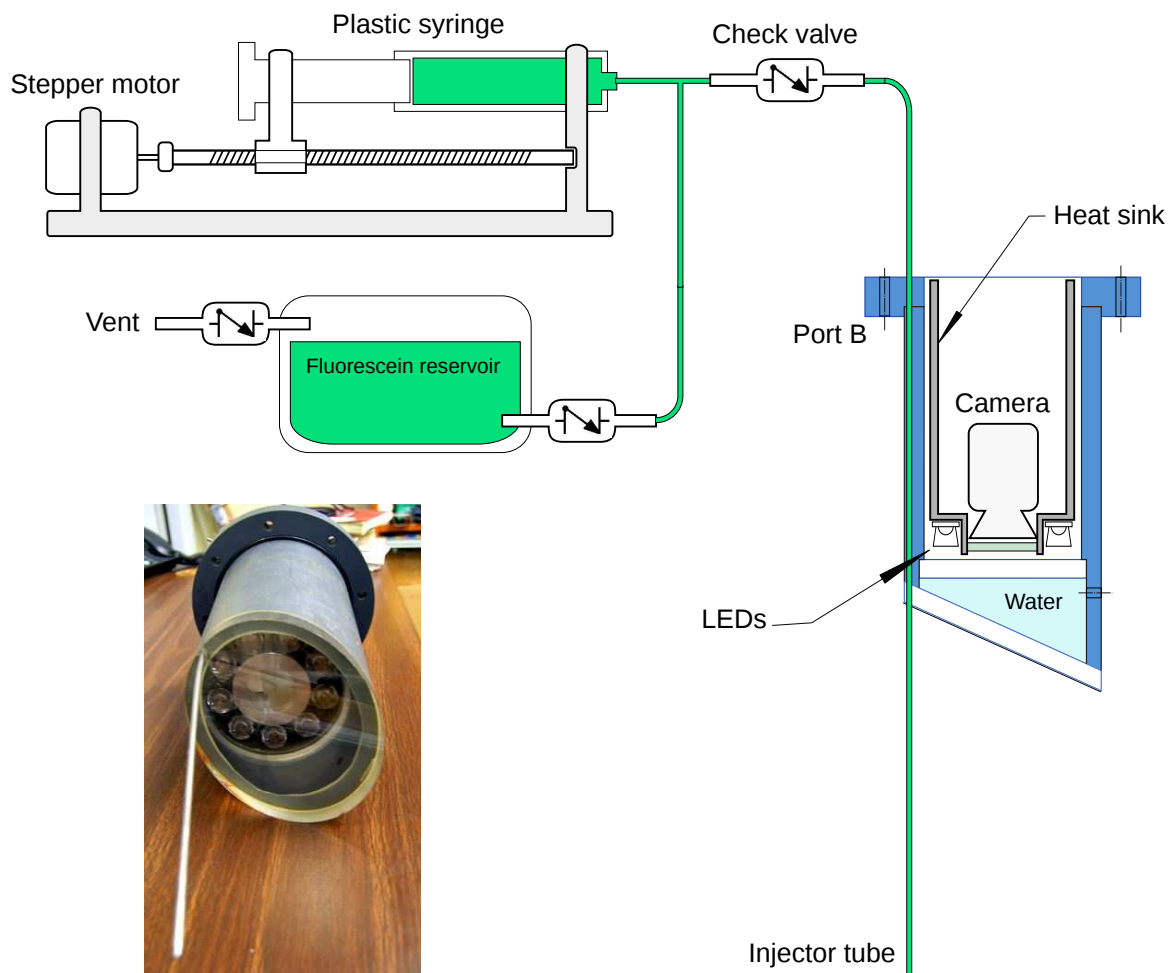


Figure 4.5: Fluorescein injection system. A computer controlled stepper motor actuates a plastic syringe. When the motor spins in one direction, fluorescein solution is injected into the 3m vessel. When the motor spins in the opposite direction, it fills the syringe with fluorescein from the reservoir. A ring of blue LEDs around a video camera provides plenty of illumination to the fluorescein dye. The plastic PVC port B has a double acrylic window filled with water to minimize image distortion due to refraction. The inset shows a photograph of the port with the illumination ring and injector tube.

This setup allowed for fluorescein images with excellent contrast.

The fluorescein injector started as a motorized syringe built by D. Zimmerman, but was not considered for use in the experimental setup until we considered fluorescein dye for visualization. D. Zimmerman also built the motor control electronics of the injector based on an Arduino board. The author introduced some mechanical improvements on the syringe and motor frame and incorporated the fluorescein reservoir, conduits, valves, and injector nozzle. The PVC port B was modified to incorporate the injector nozzle (actually a long stainless tube of about 4 mm in diameter) under the camera field of view.

Chapter 5

Precessional forcing

In this chapter we will present the experimental results when the inner and outer sphere are locked together, and rotating as a solid body at a uniform rotation rate about an axis vertical in the laboratory. No provision other than the addition of the Earth's rotation is employed to achieve precessional forcing. The Ekman and Poincaré numbers, E and Ω , are then linked and cannot be varied independently. Rotation rates range from about 0.05 Hz to 1.5 Hz, corresponding to $E = 1.49 \times 10^{-6}$, $\Omega = 2.31 \times 10^{-4}$ and $E = 4.98 \times 10^{-8}$, $\Omega = 7.72 \times 10^{-6}$ respectively. The fixed precession angle is precisely our geographical colatitude, $\alpha = 51^\circ$. Retrograde in this chapter means in the opposite direction to the precession direction, i.e. sphere rotation vector pointing down, opposite to the Earth's rotation.

5.1 Stationary state

In each experimental run the sphere was set to a predetermined constant angular speed, while wall shear stress, pressure, temperature and fluid velocity are recorded. Typically, 2 to 3 minutes after the start of the run, the sphere reaches its target speed while most of the fluid is still spinning up. The wall shear stress probe shows a large signal at this point; as the fluid spins up the signal's magnitude progressively diminishes. After many spin-up times elapse (the characteristic time

scale of spin-up is $(\omega_c \sqrt{E})^{-1}$, with ω_c the rotation rate of the container), the fluid still does not rotate with the container as a solid body as evidenced by the residual wall shear stress level (see plot in Figure 5.1). Rather, it shows oscillations at the same frequency as the sphere rotation. The ultrasound probe on port D, measuring fluid velocities along a vertical chord (referred to as chord D from now on) also shows oscillations as can be seen in Figure 5.2. As the fluid spins up to match the sphere's rotation, the sphere itself changes its orientation in inertial space, due to the rotation of the Earth. The flow generated this way is a realization of the spin-over mode excited by the precessing sphere.

The velocity profile as evidenced in Figure 5.2 departs little from being a flat profile with depth. As we have shown earlier in Chapter 2, a flat profile is expected if the flow corresponds to a solid body rotation around a horizontal axis (of course, as measured in the frame rotating with the sphere). This turns out to be the case, as we will show below. In fact, we observe that departures from a flat profile are mostly caused by internal shear layers.

The measured amplitude of the fluid velocity along chord D depends on its z coordinate. Figure 5.3 shows the standard deviation of the velocity as measured with the ultrasound doppler transducer on port D as a function of z/L (L is the vessel radius in mm) for a range of retrograde rotation rates. Note the feature around $z/L = 0.77$, common to almost all rotation rate profiles. The oscillations as measured along chord B (not shown) which is azimuthally 180° away from chord D, have a relative phase difference of $\sim 180^\circ$ indicating an $m = 1$ azimuthal pattern, a clear indication of the spin-over mode. The velocity amplitude is almost flat at

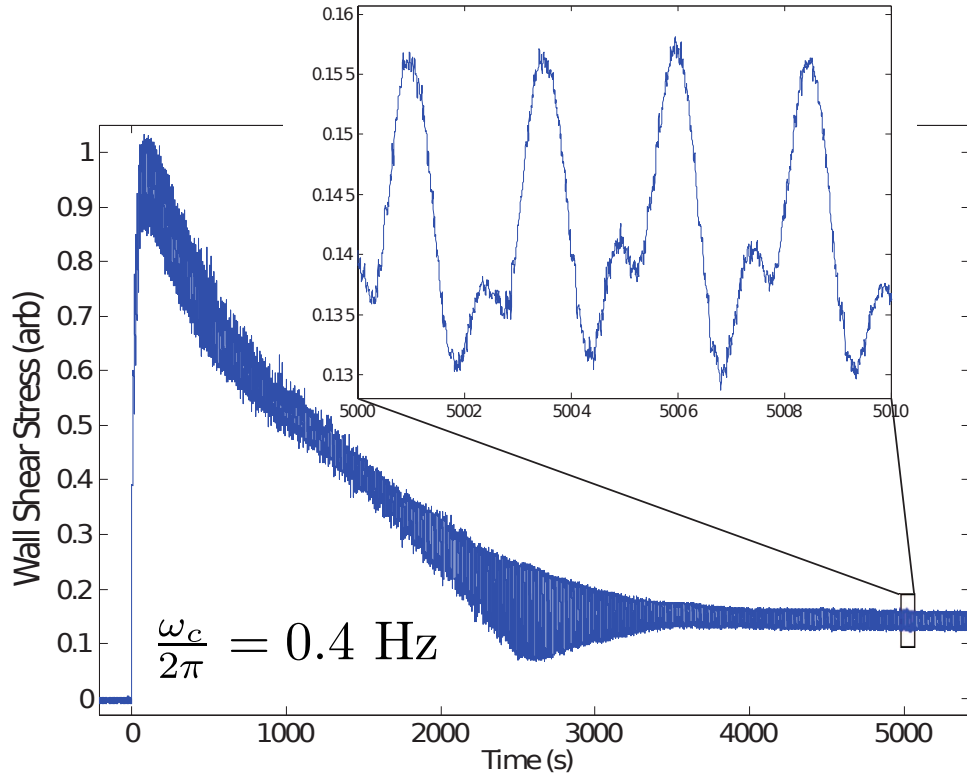


Figure 5.1: The signal from a wall shear stress probe on the outer boundary. At $t=0$ the sphere is set to spin at a uniform rate of 0.4 Hz. After the initial transient motions dissipate (about 4000 seconds in this example) small fluid oscillations persist. These oscillations have the same frequency as the rotating sphere. The small higher harmonic components of the signal are due mainly to the non-linear response of the probe. Note also that the mean level of the signal in the steady state is different from the mean level when $t < 0$.

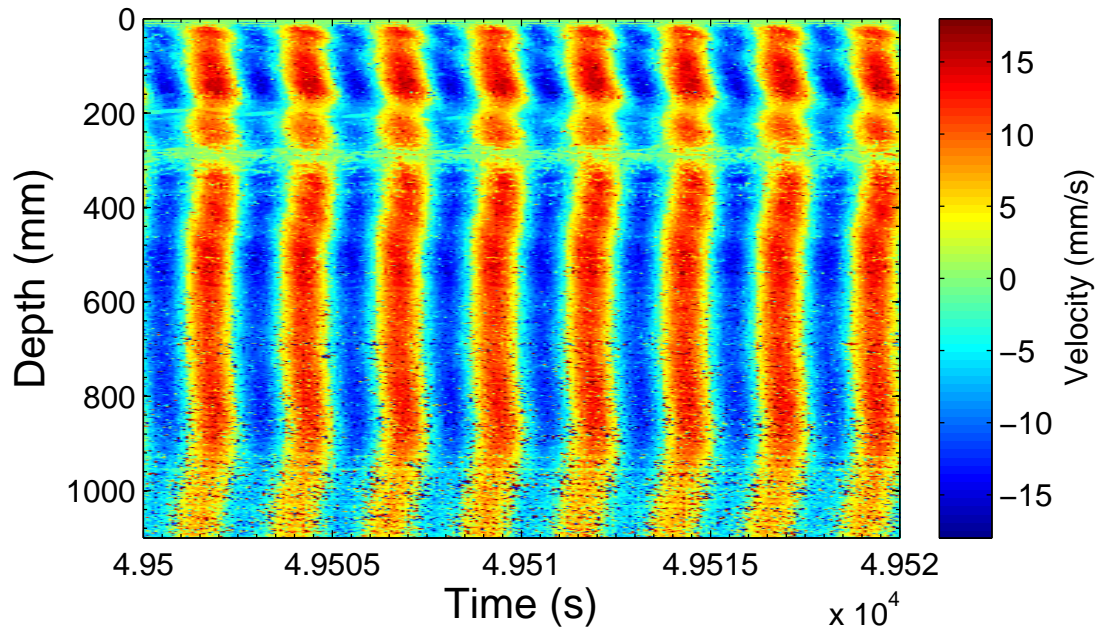


Figure 5.2: Velocity of the steady state flow in the vertical z direction as measured with an ultrasound doppler transducer on port D; rotation rate is 0.4 Hz. Vertical axis is distance to the probe. At around 300 mm there are not enough particle scatterers to get an acceptable ultrasound echo. For depths larger than 1000 mm the signal starts to degrade as well due to weak echoes from particles and unwanted echoes from solid surfaces.

slow rotation rates, and shows more features as we go up in rotation rate. Features are sharper at smaller Ekman numbers

Unfortunately, the tracer particles in the fluid do not stay suspended over prolonged periods of time, due to centrifugal effects. There were always some tracer particles in the fluid prior to each experimental run, and initial transients and turbulence would mix them more or less uniformly over the volume. Usually, by the time the flow reached stationary state (about 3 hours for 0.05 Hz and about 30 minutes for 1.5 Hz) the particles would be absent from the ultrasound beam. Therefore, we inject particles periodically into the fluid to get usable ultrasound signals. The particles injected stay in the beam longer when the sphere is spinning at slow rotation rates. Centrifugal forces at high rotation rates quickly pull particles away from the beam path. For small rotation rates we were able to obtain full-depth velocity profiles, while at high rotation rates there were often large voids. Reliable ultrasound echoes common to all rotation rates were registered only up to 600 mm away from the transducer ($0.9 > z/L > 0.5$).

The mean value of each profile in Figure 5.3 is a single quantity roughly proportional to the spin-over amplitude at each rotation rate. To compare this quantity with the theory discussed in Chapter 2, we need the ellipticity that best represents the outer sphere. As we have seen in Chapter 3, the outer sphere shape is not simple and no single value can represent its true shape. In view of this difficulty, we compare the measurements with the theory using a range of ellipticities close to the outer sphere's actual shape. For example, one value could be the ellipticity of an oblate spheroid having the same polar diameter as the outer sphere and an equa-

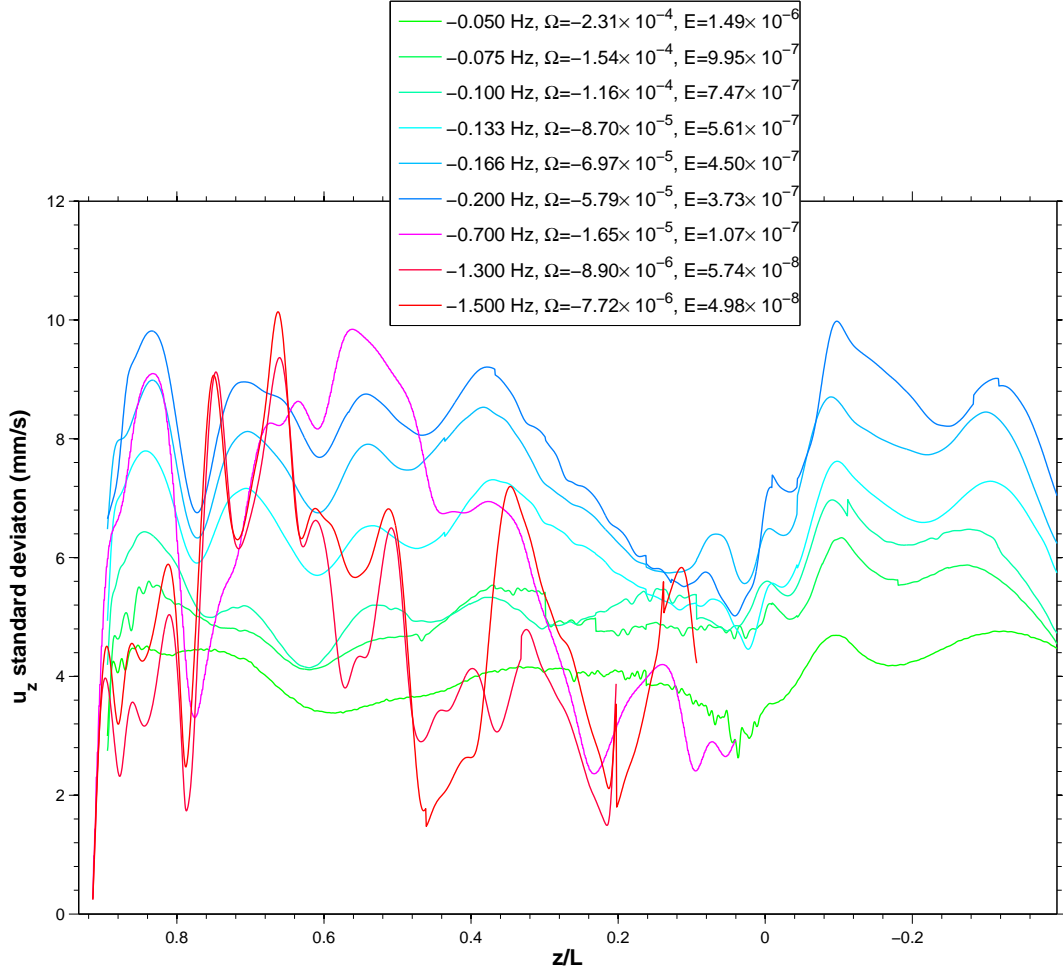


Figure 5.3: Standard deviation of flow velocity along chord D for different retrograde rotation rates. The velocity is measured using an ultrasound Doppler transducer located at $z/L = 0.9147$ pointing in the negative z direction. $L=1460$ mm is outer sphere radius. The equator is at $z/L = 0$. Departures from flat profiles, observed at low rotation rates, are caused by internal shear layers that strengthen at high rotation rates.

torial diameter equal to an average of the equatorial diameters of the outer sphere. This translates into an ellipticity $\eta \sim 1/280$. A further complication comes from the fact that the outer sphere shape must deform slightly due to rotation. Using linear elasticity theory we can estimate the fractional change in the outer sphere radius to be

$$\frac{\Delta R}{R} = \frac{\sigma}{E} \quad (5.1)$$

where σ is the hoop stress and E the modulus of elasticity for type 304L stainless steel. Due to this effect one needs to, in principle, adjust the ellipticity as the rotation rate is increased. The plot shown in Figure 5.4 summarizes all velocimetry data for all rotation rates both prograde and retrograde, compared against theory (equations 2.31 and 2.33) using a range of ellipticities (when at rest) between $1/600$ and $1/200$. The general trend observed compares qualitatively well with the theory.

The oscillation amplitude determines the angle θ between the vessel rotation vector $\boldsymbol{\omega}_c$ and the fluid rotation vector $\boldsymbol{\omega}$, according to equation 2.34. To determine the orientation of $\boldsymbol{\omega}$ it is necessary to measure the oscillation phase with respect to the synchronization signal provided by the infrared LED in the lab frame. The measured phase provides the azimuthal coordinate ϕ of $\boldsymbol{\omega}$ directly; see Figure 2.3 and equation 2.33. The measured phase profile for different depths is not constant, especially at high rotation rates as evidenced in Figures 5.5 and 5.6. The phase around $z/L = 0.77$ changes rapidly with depth and eventually wraps around for rotation rates higher than 1.0 Hz. Therefore to obtain a single quantity representing the overall phase for a given rotation rate profile is not well defined, given the

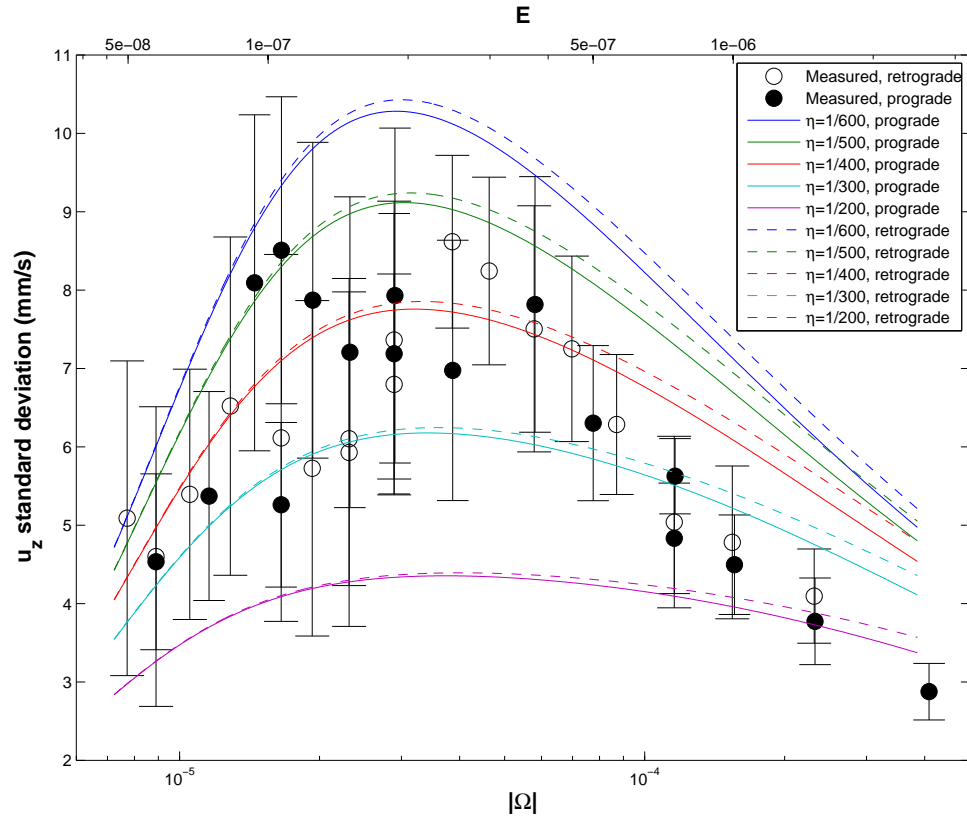


Figure 5.4: Standard deviation (depth averaged) of the z component of the fluid velocity as measured from port D. The error bars give a measure of the variability of the velocity amplitudes along z . Colored curves color represent the theoretical prediction computed from equation 2.31 for the standard deviation of u_z given different ellipticities η (at rest). Top and bottom horizontal axes show the corresponding Ekman and Poincaré numbers, respectively.

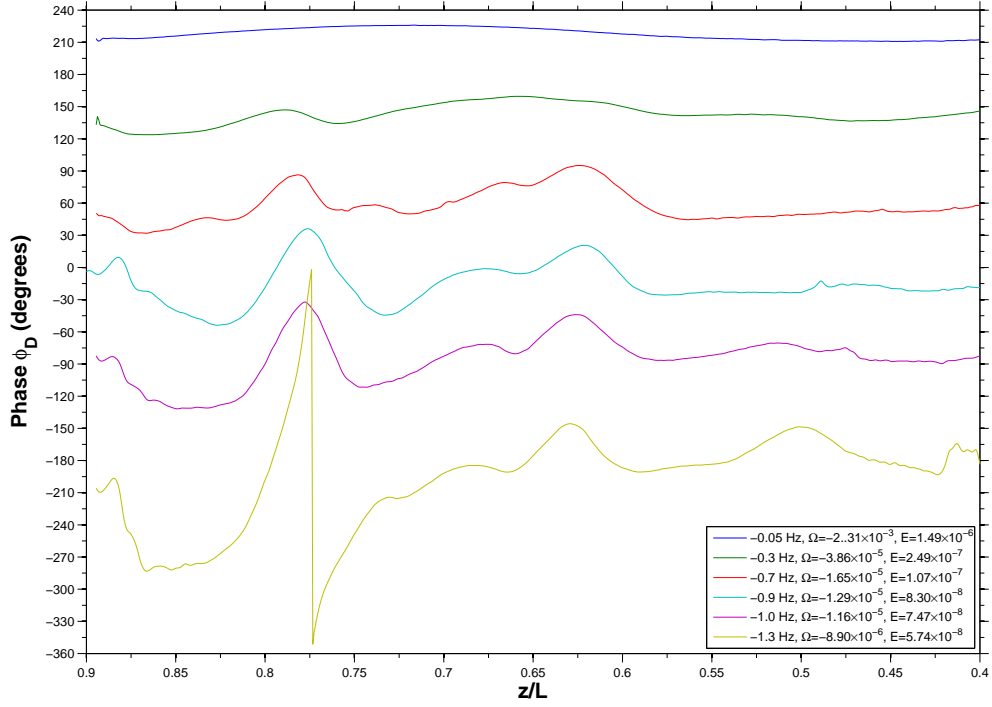


Figure 5.5: Phase measured from chord D at different retrograde rotation rates. Note the feature near $z/L = 0.78$. Phase is measured with respect a synchronization signal in the precessing (lab) frame.

large variability in the profile. For low rotation rates an average of the phase is nevertheless used to estimate of the overall phase. The average of the phases is calculated as a vector sum and not arithmetically (since the average between, e.g. 180° and -180° is *not* 0°). Figure 5.7 shows a comparison of this average and the expected phase as calculated from equation 2.31. There is agreement between theory and experiment only for the smaller rotation rates. Later, we will discuss possible reasons for this.

The pressure transducers provided very limited information. Unfortunately,

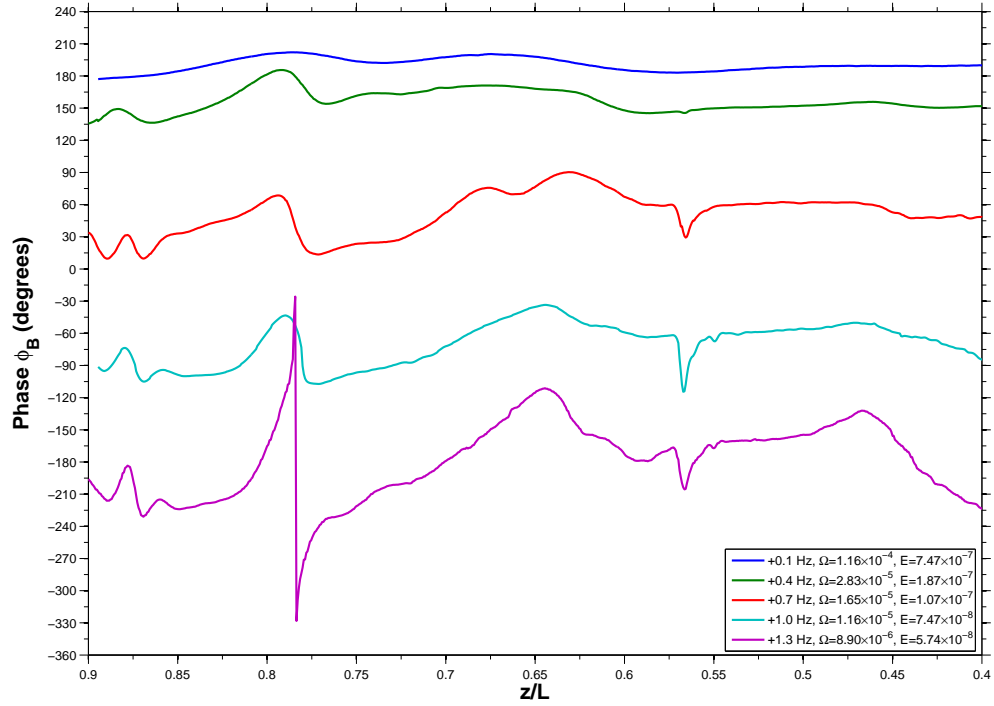


Figure 5.6: Phase profiles for different prograde rotation rates, measured from port B. Note the rapid change near $z/L = 0.77$ as the rotation rate increases. The feature near $z/L = 0.53$ is an artifact due to echoes, reflecting multiple times from solid boundaries, dominating the echoes from tracer particles.

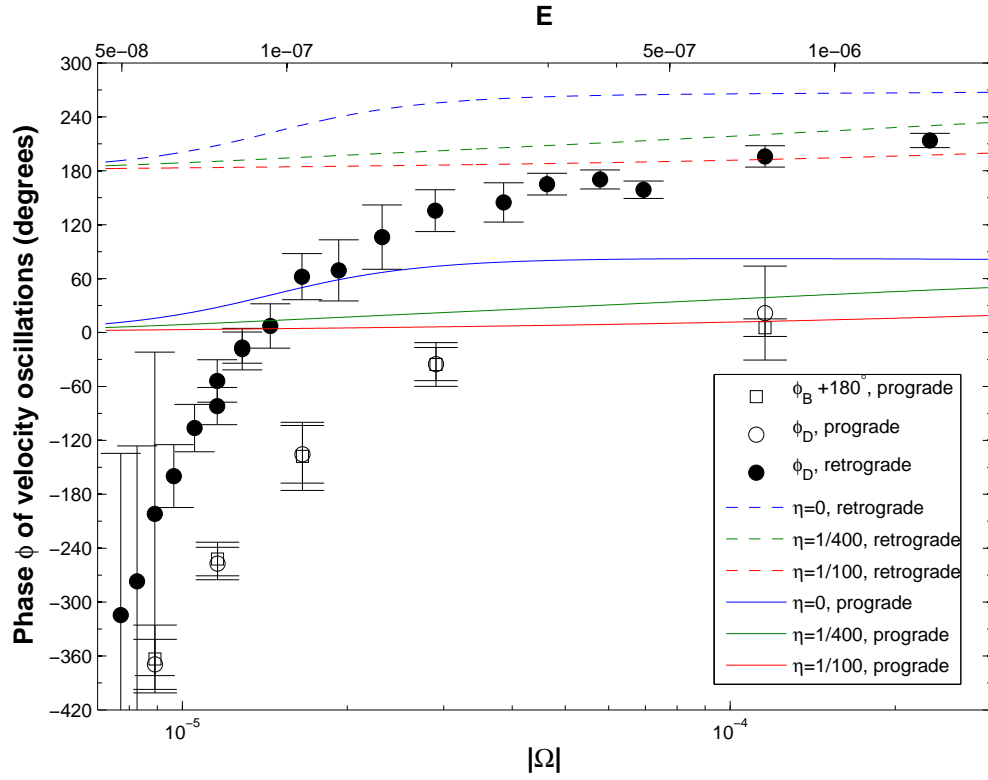


Figure 5.7: Average phase of fluid oscillation as a function of Poincaré number for all prograde and all retrograde rotation rates explored. Colored lines are the predicted phases for different ellipticities.

they turned out to be sensitive to wall shear stress whenever they were not in thermal equilibrium with the fluid. Noticeable temperature gradients would develop in the fluid during the time needed to reach steady state. This is not a problem when differentially spinning the inner sphere (Chapter 6), as the increased turbulence levels provided enough mixing to bring the probes to thermal equilibrium with the water. As indicated in Figure 5.8 the phase of the pressure signal is not consistent with the phase ϕ of the spin-over flow, nor with the theoretical phase. It does not show, however, the drastic change in phase with rotation rate as u_z does. It stays about 90° away from the theoretical phase for almost all rotation rates. An approximate $m = 1$ azimuthal pattern is evident when comparing the pressure signals from different ports. We believe these pressure phase observations are due to their signal being dominated by shear stress.

5.2 A free shear layer

Let us examine in more detail the feature around $z/L = 0.77$. The space-time diagram in Figure 5.9 shows a localized shear layer at that position. It can be described as a localized wave packet whose phase is propagating along the profile. This feature was visible only for rotation rates higher than 1.0 Hz. A rough estimate of the feature's wavelength is $\sim 58\text{mm}$ (rotation rate is 1.3 Hz). Assuming this is a shear layer inclined 30° from the vertical (as is expected since the dimensionless oscillation frequency at any point in the profile is 1), then the actual wavelength is $\lambda \simeq 29\text{mm}$. The phase speed \mathbf{c}_p corresponds to the smallest inclination of the phase

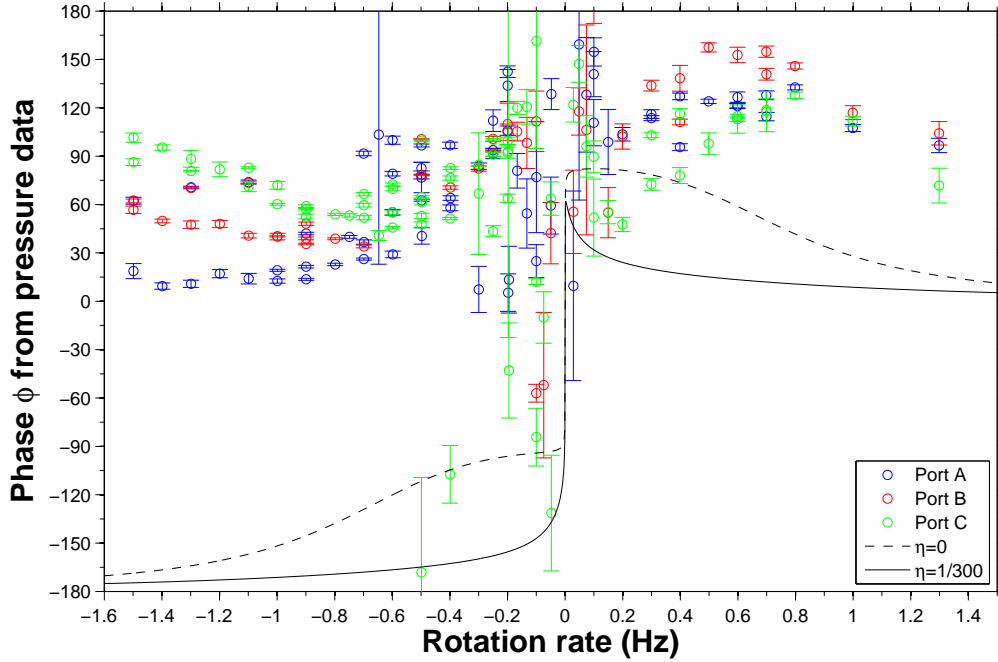


Figure 5.8: Oscillation phase ϕ as calculated from pressure measurements on ports A-C. The pressure transducers are sensitive to wall-shear stresses originating in the Ekman layer, in addition to fluid pressure, complicating their interpretation.

fronts in Figure 5.9, which is $\sim 36.5\text{mm/s}$ as measured from the figure itself. This is in reasonable agreement with equation 2.16 as the magnitude of the phase velocity is $c_p = \lambda\omega_c/2\pi = 37.7\text{mm/s}$.

5.3 Discussion

For a cavity with a given shape, the amplitude of the spin-over mode excited by precession depends ultimately on the Ekman and Poincaré numbers only. In other words, equilibrium is reached between dissipation and the precessional forcing. The fact that the measured amplitude of the spin-over mode is consistent with Busse's

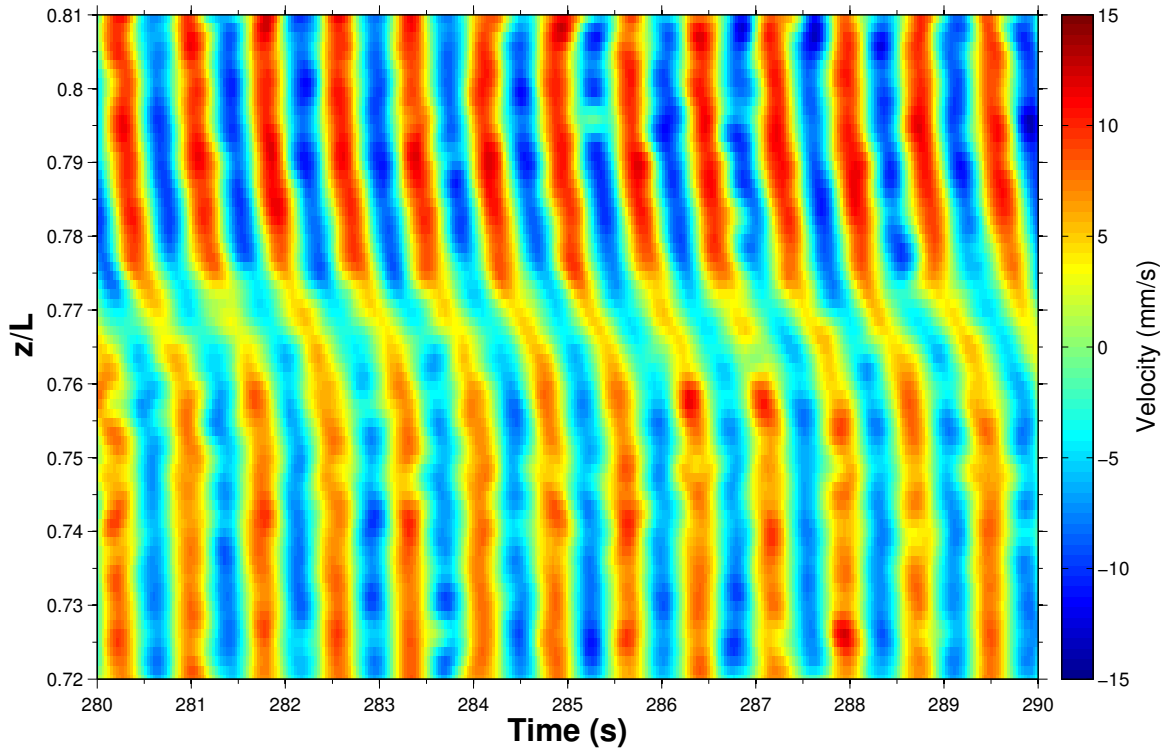


Figure 5.9: An internal shear layer, seen here between $z/L = 0.760$ and $z/L = 0.775$, for $E = 5.74 \times 10^{-8}$. The velocity amplitude of the internal shear layer at this rotation rate (1.3 Hz) was enough to overcome the background spin-over flow and reveal its moving phase front.

theory indicates that the effect of the inner core (or the shaft), or the topographical details of the outer boundary are relatively unimportant when it comes to the energy balance, which is determined ultimately by the ellipticity, the Ekman and Poincaré numbers.

The phase ϕ (or azimuthal orientation) of the fluid spin axis deviates significantly from the prediction for moderate rotation rates and higher. The presence of the inner sphere or the shaft can be related to the cause but, it should be noted, at moderate and higher rotation rates it is difficult to define a fluid-spin axis, as the internal shear layers, becoming sharper, complicate the underlying flow. The phase discrepancy can also be related to a different torque balance from that of a precessing spheroid as the theory assumes, given that the pressure torque (see equation 2.28) depends on the actual shape of the outer boundary.

The energy appears to concentrate at specific locations as the rotation rate increases, a fact already familiar to theorists (see for example [40]). Our basic observation is that both the amplitude profile and the phase profile along the z direction develop sharper features as the rotation rate increases. This fact should be attributed to the shrinking Ekman number and not to the Poincaré number. At high rotation rates any topographical feature on the boundaries will shed inertial waves, propagating into the interior forming free shear layers, just the same as the singularity in the Ekman layer does at the critical latitudes. The feature observed near $z/L = 0.77$ could be caused by a topographical feature, in which case its size would be independent of the Ekman number, but figure 5.3 suggests that its size decreases as E decreases, just as many numerical simulations and analytical work

(e.g. that of Kerswell [16]) show.

Figure 5.10 shows the ray paths emanating from the critical latitudes of either the inner or the outer boundary. The ultrasound beam first crosses one of the rays at around $z/L = 0.74$ but we can see that a small change in the boundary shape will change the precise location of the crossing. In fact, any deviation from a sphere can dramatically change the ray pattern and thus the amplitude and phase profile along any chord.

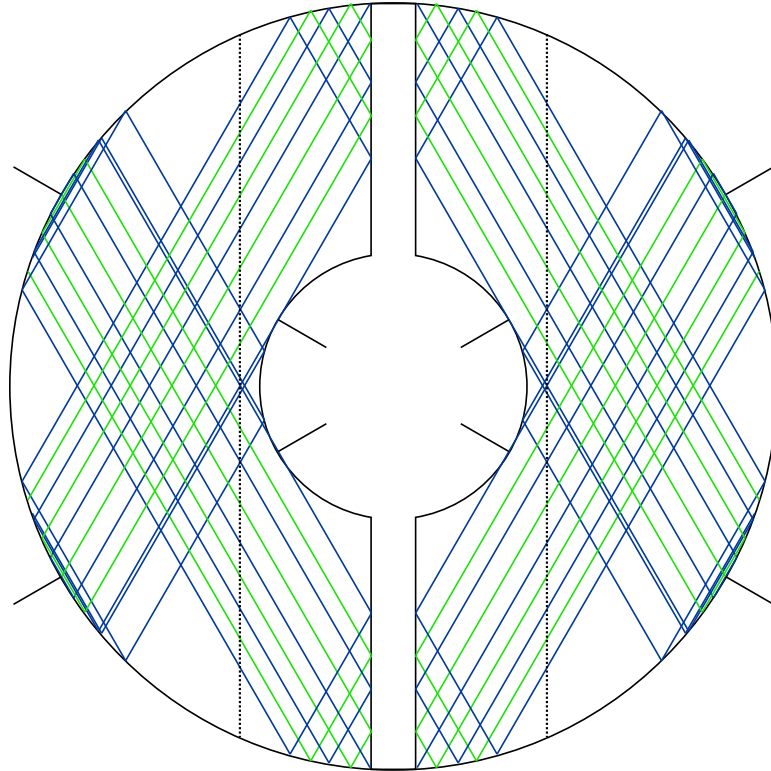


Figure 5.10: Ray paths of inertial waves launched from the critical latitudes up to seven reflections. Green paths emanate from the critical latitudes at the outer boundary and blue paths originate at the critical latitude on the inner boundary. The two dotted vertical lines show the location of the ultrasound beams used for velocimetry. The first crossing of the ultrasound beams with one of the rays occurs near $z/L = 0.74$. Compare this to the experimentally measured location of the shear layer at $z/L = 0.77$.

Chapter 6

Differential rotation forcing

Let us turn to the experimental results obtained when the inner sphere rotates at an angular speed different from the angular speed of the outer sphere. Their angular speeds constitute the two experimental control parameters. The corresponding dimensionless parameters are the Ekman number E and the Rossby number Ro defined as follows:

$$E = \frac{\nu}{\omega_c L^2}, \quad Ro = \frac{\omega_i}{\omega_c} - 1, \quad (6.1)$$

where ω_i and ω_c are the angular frequencies of both the inner and outer spheres respectively. $L = 1.46$ m is the mean radius of the outer sphere. By using these quantities, we are effectively implying a velocity scale $(\omega_i - \omega_c)L$ and a corresponding pressure scale $\rho(\omega_i - \omega_c)L^2\omega_c$. This is the same convention used in experimental studies by D. Kelley in the 60 cm experiment, and by D. Zimmerman in the 3m device. It should be noted that, in the frame rotating with the outer sphere, the above velocity scale corresponds to the tangential velocity at the equator of the inner sphere if it had the same diameter as the outer sphere. This choice of scale ensures that the Rossby number Ro represents precisely the (dimensionless) angular speed of the inner sphere, as seen in the outer sphere frame.

6.1 Overview

The basic phenomena observed with differential rotation are as follows: members of a sub-family of the full sphere inertial modes are excited as the inner sphere speed is changed. Which members of the sub-family are excited depends on the speed of the inner sphere. Let us examine in some detail the signature of these modes from the recorded pressure measurements.

For a given experimental run examined here, the outer sphere is set to spin at a fixed angular speed and the inner sphere angular speed is ramped from close to perfect corotation ($Ro \simeq 0$), down to no net angular speed in the lab frame ($Ro = -1$) and then reverse direction until reaching about $Ro \simeq -2$. The dynamics for $Ro > 0$ is detailed in D. Zimmerman's dissertation work, and the reader is encouraged to consult it as relevant inertial wave phenomena are also described there. In the present study we restrict ourselves to the $Ro < 0$ range.

Let us begin with the spectrograms in Figures 6.1 and 6.2, computed from the pressure measured at one of the ports. The fixed rotation rate of the outer sphere is 0.7 Hz and the corresponding Ekman number is $E = 1.067 \times 10^{-7}$. There is a gap in the measurements in the range $-1.2 < Ro < -0.8$ given that the inner sphere motor cannot be made to spin reliably at low speeds (< 0.15 Hz). The frequency is made dimensionless by using $1/\omega_c$ as the unit of time, and the pressure is similarly made dimensionless by using $\rho(\omega_i - \omega_c)L^2\omega_c$ as the unit of pressure.

As expected from our previous experience with the 60 cm apparatus (Kelley et al. [14]), a number of features appear. They can be identified as inertial modes of the

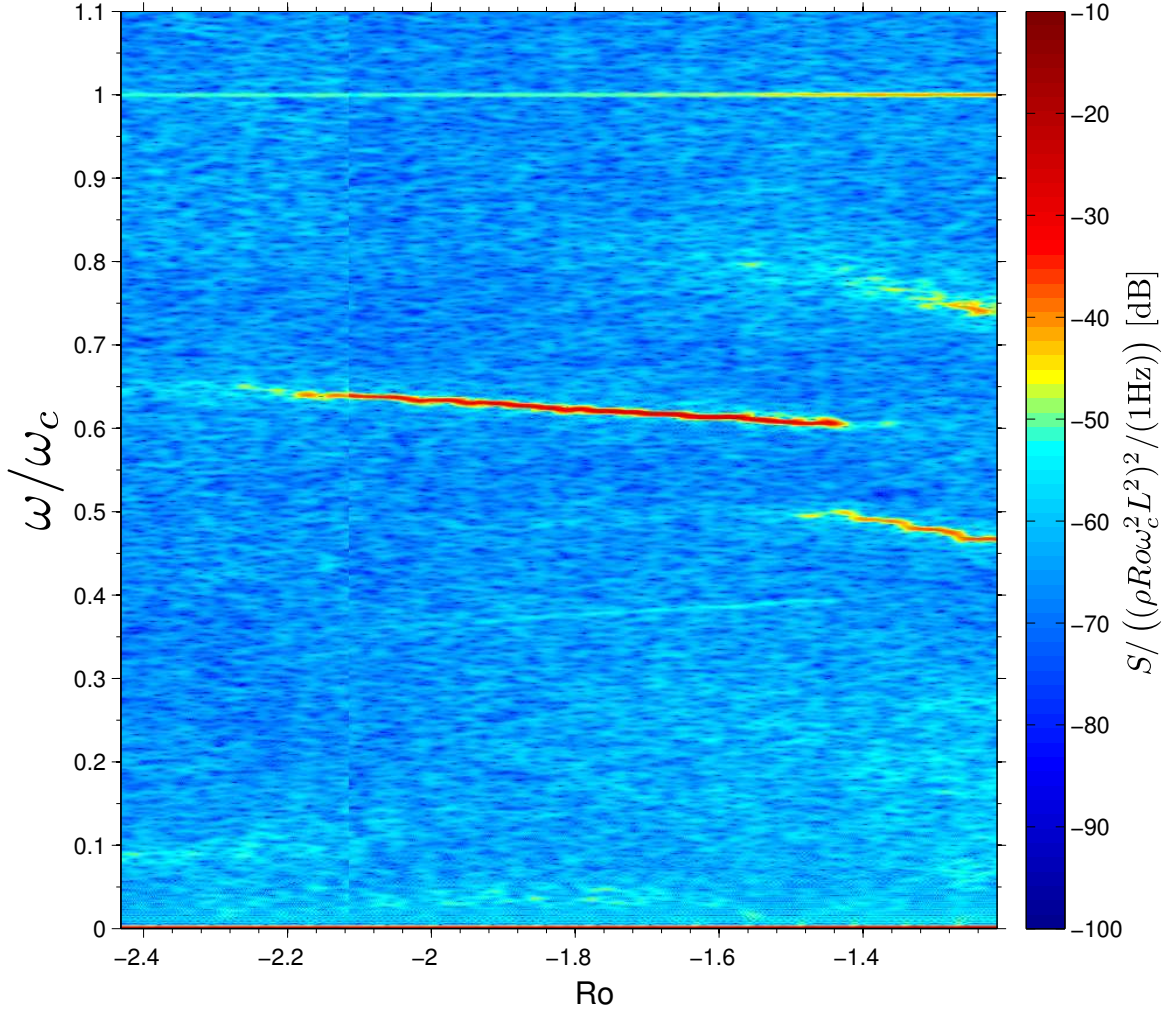


Figure 6.1: The dimensionless power spectral density $S/[(\rho R \omega_c^2 L^2)^2 / 1\text{Hz}]$ in dB (color scale) of the pressure as measured at one of the ports (S is the power spectral density of the pressure in Pa^2/Hz , and $\rho R \omega_c^2 L^2$ is the unit pressure scale). This plot is assembled by computing an FFT of the pressure signal at a particular rotation rate of the inner sphere. At each step the inner sphere was kept constant for about 10 minutes and then increased by 0.05 Hz (this particular ramp goes in time from right to left). The range of Ro here corresponds to the inner sphere rotating in the opposite direction to the outer sphere. The Ekman number here is $E = 1.067 \times 10^{-7}$, corresponding to an outer sphere rotation rate of 0.7 Hz.

container excited by the differential rotation of the inner sphere. All the measuring probes are in the rotating frame, and the spectrum does not unfold due to azimuthal wave numbers m different than one, as is the case in the 60 cm experiment where the probes are fixed in the lab frame, and therefore their frequency spectrum is unfolded according to the azimuthal wave number m .

We use a digital bandpass filter on the data generated by the pressure probes to examine their phase relationships. Since we have only three pressure probes situated physically 90° apart we cannot distinguish an $m = 2$ azimuthal pattern from another $m = \text{even}$ pattern. Higher $m = \text{odd}$ modes can also be difficult to resolve. We nevertheless have the frequency of each mode and an estimate of what m number to expect based on 60 cm data. It is also somewhat unlikely that very high m modes are excited since their viscous damping is correspondingly higher.

Examining figure 6.1 in more detail we see a strong signal with $\omega/\omega_c \simeq 0.6$ appearing between $-2.2 < Ro < -1.4$. By examining the phases of the three bandpassed pressure signals in this region, it is clear that there is an $m = 1$ azimuthal pattern going in the retrograde direction, i.e., the direction opposite to the outer sphere rotation. This corresponds to the $l = 4, m = 1, \omega/\omega_c = 0.612$ inertial mode for a full sphere (see Chapter 2 for details on mode notation). On the right side of the Figure we see two other features, weaker in power, corresponding to the modes $l = 6, m = 1, \omega/\omega_c = 0.440$ and $l = 3, m = 2, \omega/\omega_c = 0.667$. Perhaps the identification of this latter mode would have been more difficult without the previous observations of its spatial shape as imaged by the 60 cm device; the measured frequency of this particular mode is about 8% higher than the theoretical, making identification

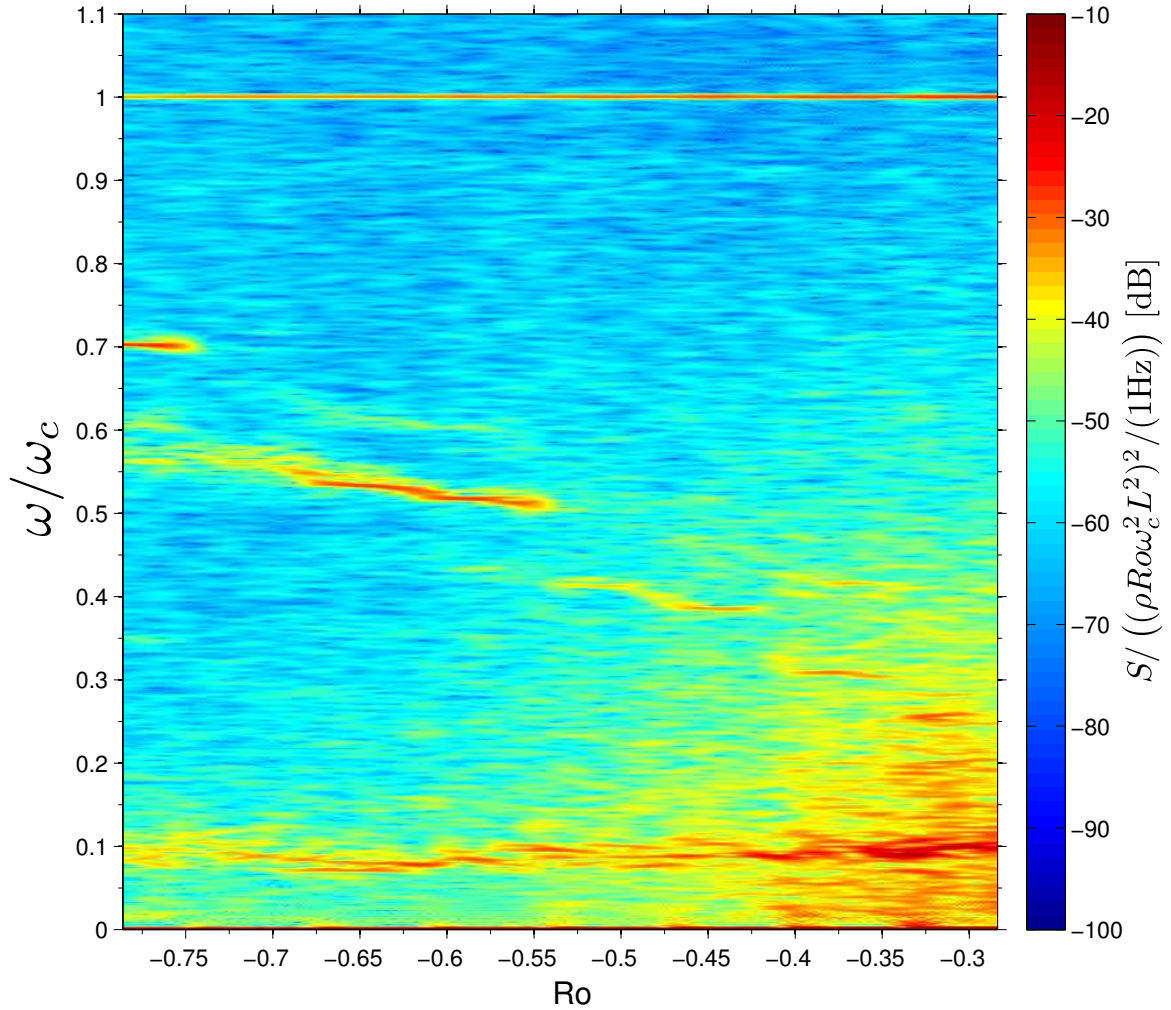


Figure 6.2: . In this range of Ro the inner sphere is rotating in the same direction as the outer sphere but at a lower speed. The feature at $\omega/\omega_c = 1$ is caused mostly by electromagnetic or acoustic noise. A low frequency oscillation around $\omega/\omega_c = 0.1$ can be seen during the whole range of Ro in this ramp. The remaining features can be identified as full sphere inertial modes.

harder.

The Ro ramp continues as shown in Figure 6.2, and new modes appear as Ro becomes less negative. At least four new modes appear, in addition to a low-frequency oscillation with $\omega/\omega_c \simeq 0.1$ that is present during this part of the ramp. The four new modes have been identified with full sphere inertial modes and will be described below. The low-frequency oscillation was not seen before in the 60 cm device, and more spatial information is needed to determine if it corresponds to a full sphere inertial mode. This oscillation even persists for large positive Ro as observed by D. Zimmerman. Note also that as we approach less negative Ro values, the background turbulence is concentrated more in the low-frequency region. For the sake of completeness, we performed measurements with the inner sphere shaft attached rigidly to the support frame. The region near $Ro = -1$ is out of the motor speed range as mentioned earlier, but by fixing the inner sphere we get measurements at precisely $Ro = -1$. The corresponding power frequency spectrum is shown in Figure 6.3.

6.2 Pressure amplitudes and flow velocities

The longer each step of an inner sphere rotation ramp is kept constant, the better the frequency resolution in a frequency spectrum or spectrogram. Figure 6.4 shows an inner sphere ramp at an Ekman number $E = 4.98 \times 10^{-8}$. Recall that the inertial modes grow typically in an Ekman spinup time $E^{1/2}$, therefore a slower ramp at a smaller E also improves our chances of reaching a true steady state at

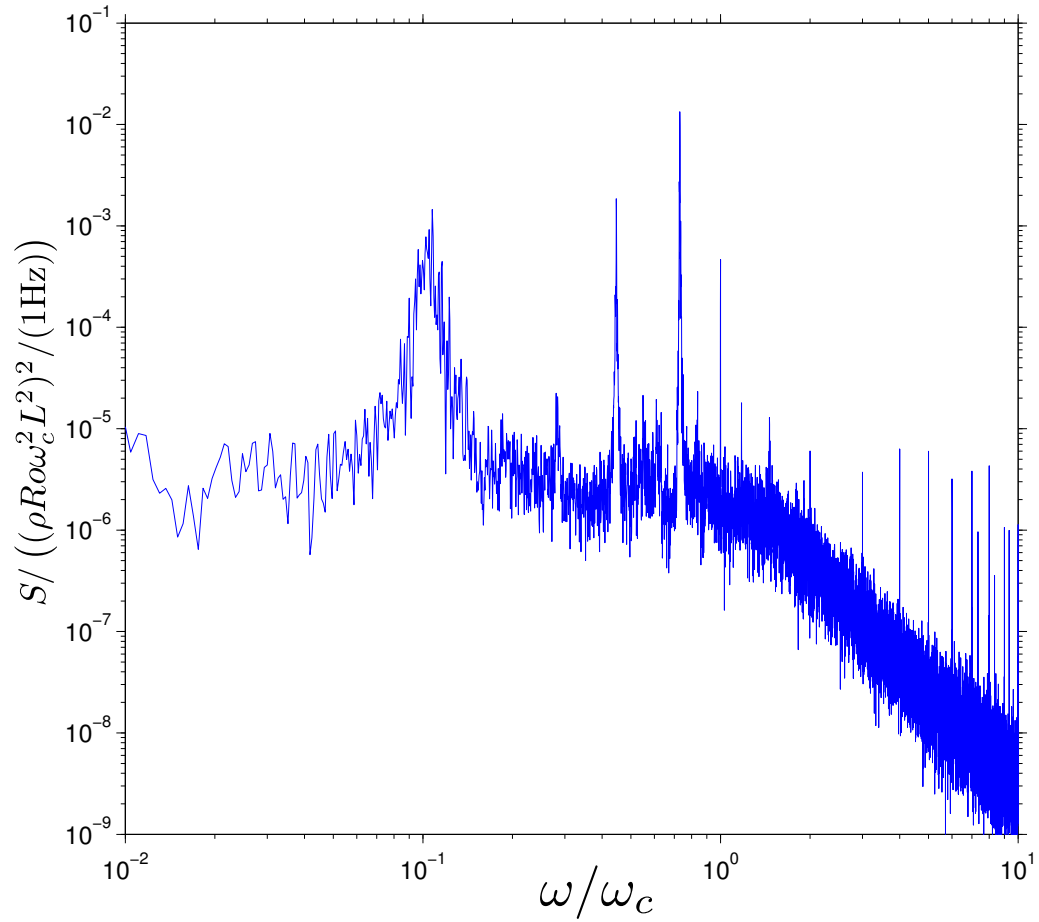


Figure 6.3: Dimensionless power spectrum $S(\omega)$ of pressure when the inner sphere shaft is rigidly attached to the support frame. The outer sphere rotates at 1.5 Hz, with a corresponding Ekman number $E = 4.98 \times 10^{-8}$ and Rossby number $Ro = -1$. The two modes indicated correspond to the full sphere modes $l = 3, m = 2, \omega/\omega_c = 0.667$ and $l = 6, m = 1, \omega/\omega_c = 0.44$. The broad low frequency oscillation peak around $\omega/\omega_c = 0.1$ is also one of the dominant features.

every step. According to Figure 6.4 no new modes appear as compared with Figure 6.1, except perhaps the weak, low-frequency oscillation near $\omega/\omega_c \simeq 0.1$.

Ultrasound velocimetry data along the z direction is available for this run. This allows us to compare absolute amplitude estimates based on pressure and flow velocity. To calculate the velocity amplitude we start with the analytical expression for a mode flow velocity \mathbf{u} , as given by 2.19, which does not have any particular normalization. We want to find the amplitude constant A such that $A\mathbf{u}_z$ equals in magnitude the measured velocity v_z (scaled with $R\omega_c L$ as the unit of velocity). Denoting a z -average with $\langle \rangle$, the amplitude constant A is

$$A = \frac{\langle v_z(z) \rangle}{\langle u_z(s_0, z) \rangle}, \quad (6.2)$$

where s_0 is the cylindrical radius of the ultrasound probe location (which also coincides with the location of the pressure probe). Since A serves as an amplitude constant to both p and \mathbf{u} , as equations 2.21 show, the expected dimensionless pressure amplitude, derived from the velocity measurements, is simply $Af(s_0, z_0)$. Figure 6.5 shows a comparison of the measured pressure and the pressure derived from velocimetry as explained.

The measured pressure is consistently lower than expected from the velocity measurements. We should bear in mind that this comparison assumes that the mode is a full sphere mode, with its flow field a small perturbation from solid body rotation. Our flow field in the experiment is far from solid body rotation, and we do not have a full fluid sphere, we have an inner sphere. We can imagine the mode being distorted by these two facts, without losing its global full-sphere character.

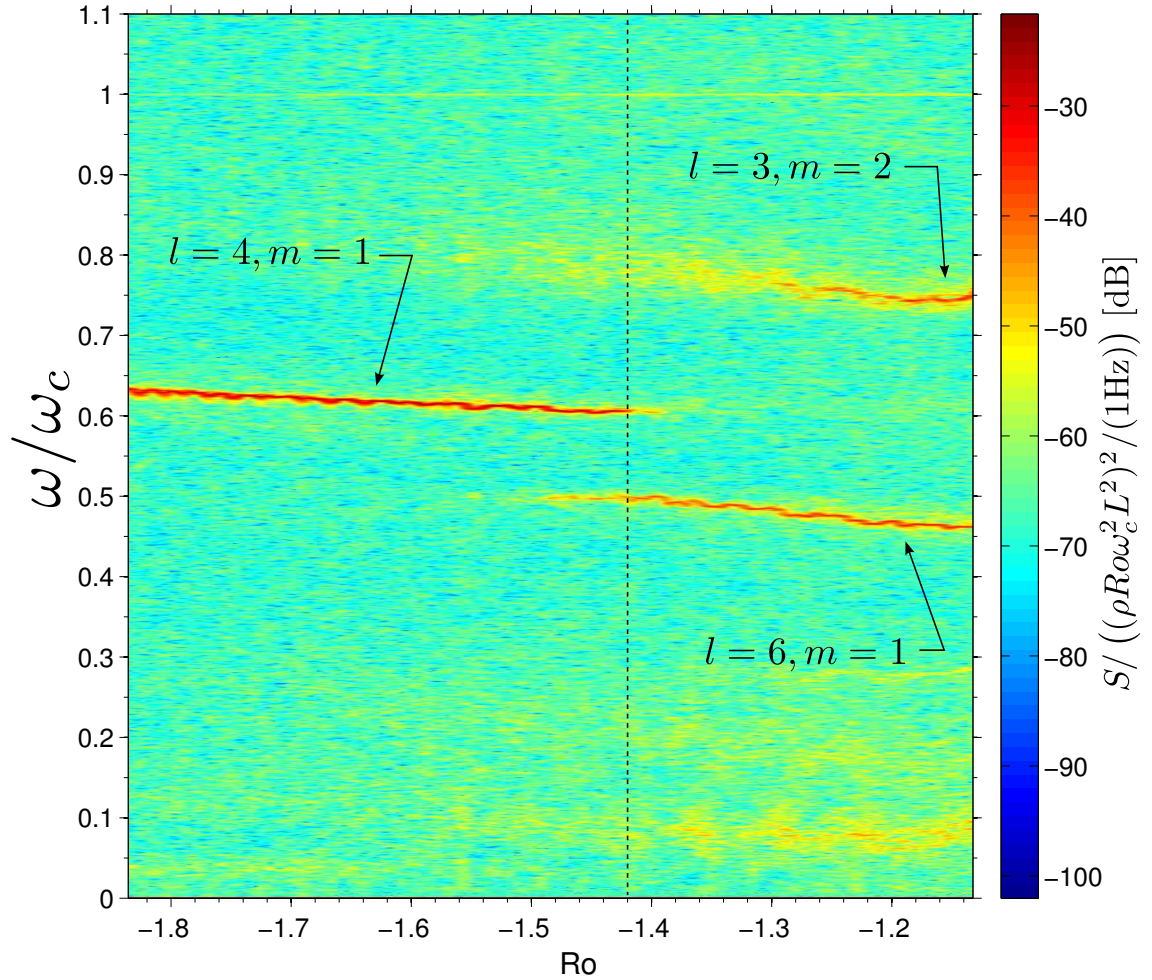


Figure 6.4: Pressure spectrogram computed from a slow experimental ramp where each inner sphere rotation speed was kept constant for 900 s. The outer sphere here is rotating at 1.5 Hz, with a corresponding Ekman number $E = 4.98 \times 10^{-8}$. Three modes are identified and the vertical dotted line marks an approximate boundary between the (4,1) and (6,1) modes.

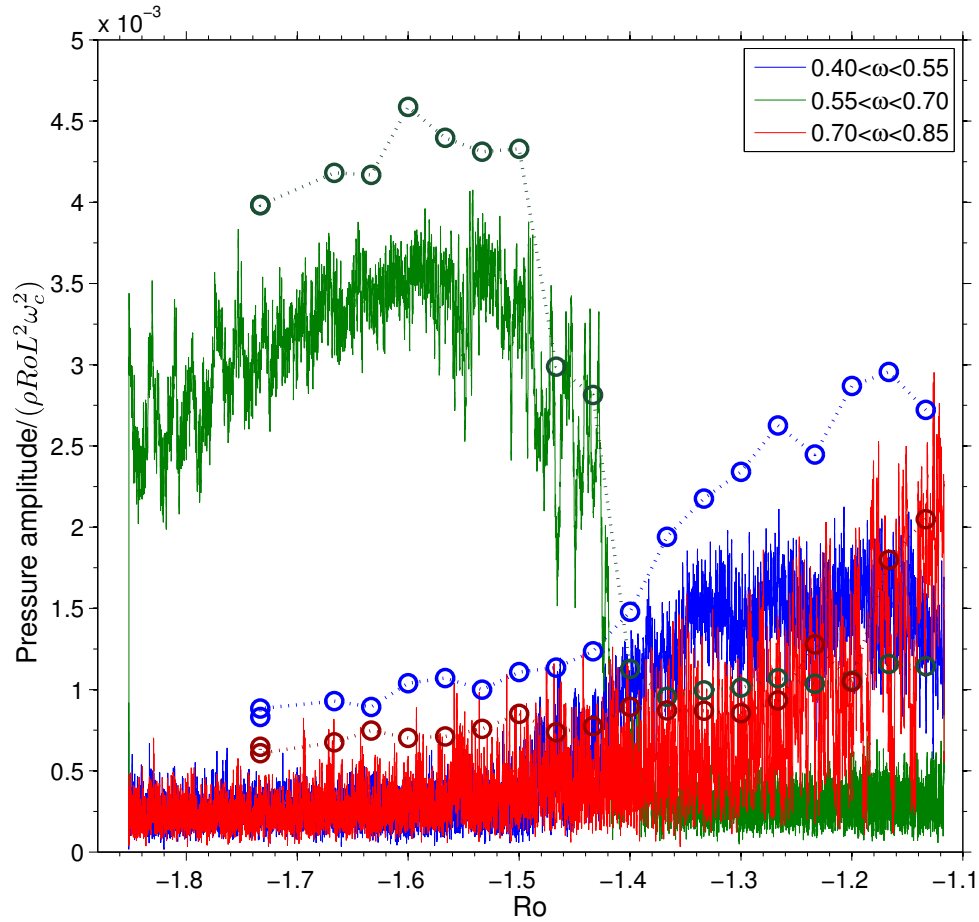


Figure 6.5: Dimensionless pressure amplitudes as measured directly (continuous lines) and pressure amplitudes as expected from ultrasound velocimetry data (circles). The data has been band-pass filtered to compute amplitudes in the frequency bands indicated. In this Ro range (same as in Figure 6.4) there is only one mode on each band. The pressure amplitudes are calculated using the magnitude of the Hilbert transform of the band-passed pressure signals. Velocity amplitudes are computed through the time-averaged standard deviation of flow velocity. Each time average corresponds roughly to a step during the inner sphere rotation ramp.

In addition, the pressure probes (due to their locations) are also measuring pressure disturbances deep within an Ekman layer.

Let us now examine a slow ramp performed with the inner sphere rotating in the same direction as the outer sphere. A pressure spectrogram is shown in Figure 6.6. The Rossby number range is $-0.86 < Ro < -0.18$. The outer sphere is rotating at 1.5 Hz with a corresponding Ekman number $E = 4.98 \times 10^{-8}$ as before. Only one of the two modes present at $Ro = -1$ (Figure 6.3) survives as the inner sphere speed approaches $Ro \simeq -0.86$. At least six more modes are excited during the course of the ramp, in addition to the low frequency oscillation around $\omega/\omega_c \simeq 0.1$. To find their azimuthal wave numbers, we use a digital band pass filter centered at the appropriate frequency, and measure the phase shift among the filtered signals coming from the three pressure probes. We will return to this in section 6.3.

Figures 6.7 and 6.8 show the pressure amplitudes and velocity amplitudes respectively for different frequency bands. Given the number of different modes present, sometimes with similar frequencies, it is not practical to carry out a comparison between pressure and velocity as described above for the counter-rotating part of the ramp. Instead, Figure 6.8 shows the z -averaged velocity amplitude over a range of z . This time we include the frequency band around $\omega/\omega_c = 1$ to determine if it corresponds to the $l = 2, m = 1$, mode (the spin-over mode). In effect it appears that at least some of the pressure signal is due to this mode, but not all of it (since the pressure oscillations are definitely bigger than what we would expect from velocimetry and our experience from precessional forcing).

Let us end this section by presenting the pressure amplitudes, both with phys-

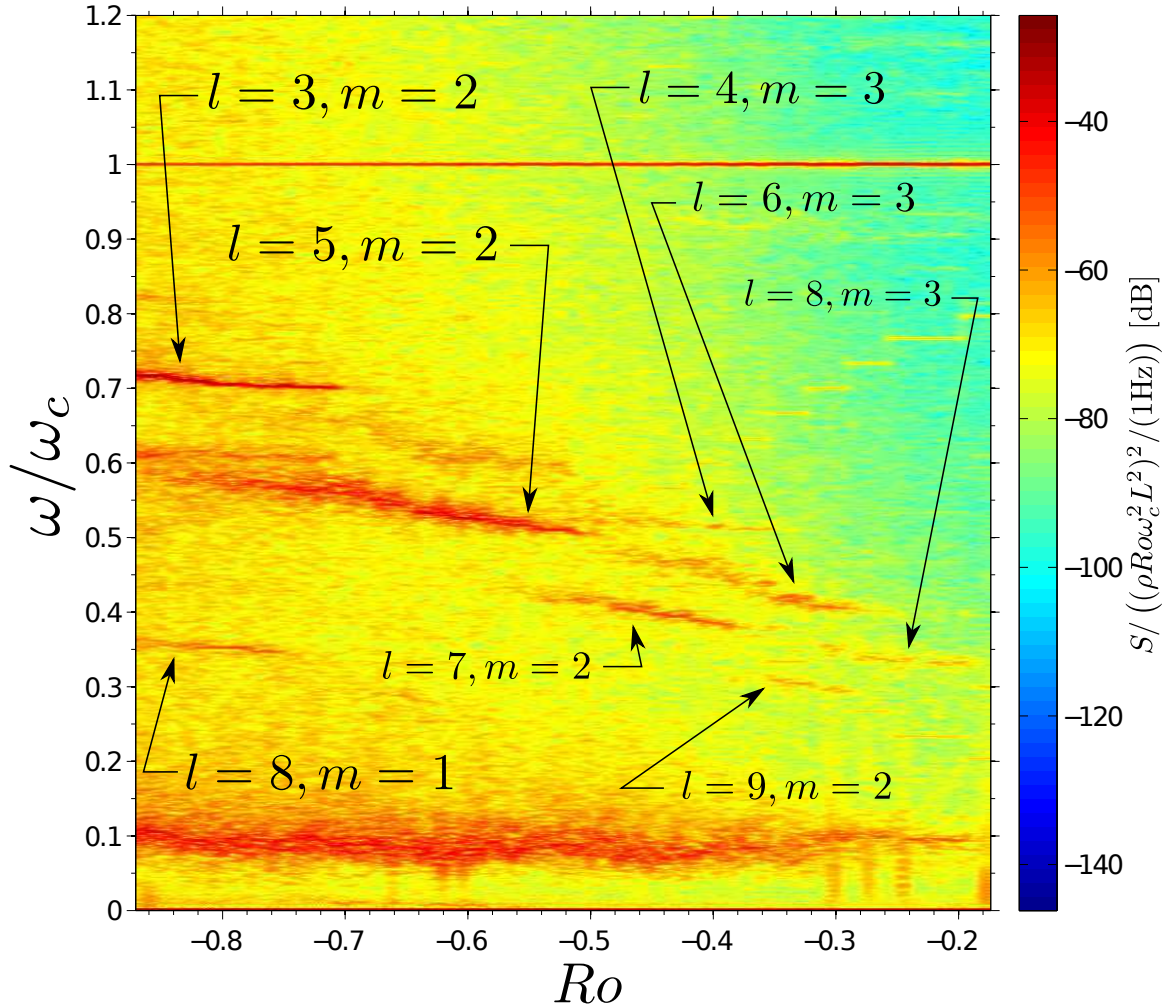


Figure 6.6: Spectrogram of dimensionless pressure as measured at one of the ports. A sequence of “tones” corresponding to inertial modes are excited at different inner sphere speeds. The range of Ro here corresponds to the inner sphere rotating in the same direction as the outer sphere but slower. Data for this ramp was taken with the outer sphere at 1.5 Hz with a corresponding Ekman number $E = 4.98 \times 10^{-8}$.

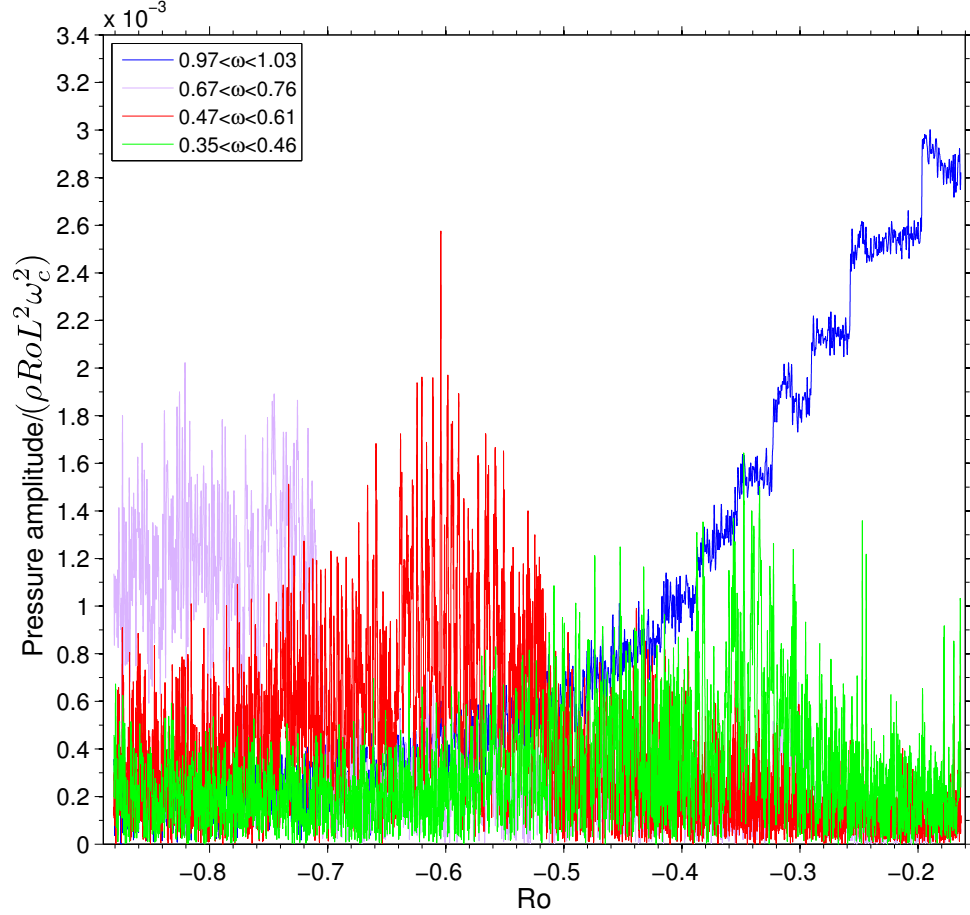


Figure 6.7: Dimensionless pressure amplitude for different frequency bands. The amplitude corresponding to the $0.97 < \omega/\omega_c < 1.03$ band (blue) grows due to the finite amplitude of the spin-over mode as the pressure scale (proportional to $|Ro|$) becomes smaller. Magenta curve shows the region where the $(l = 3, m = 2)$ mode dominates, and red curve shows where the mode $(l = 5, m = 2)$ dominates. Green curve around $Ro = -4.5$ corresponds to mode $(7, 2)$ and later around $Ro = -3.4$ corresponds to mode $(6, 3)$. Here $E = 4.98 \times 10^{-8}$.

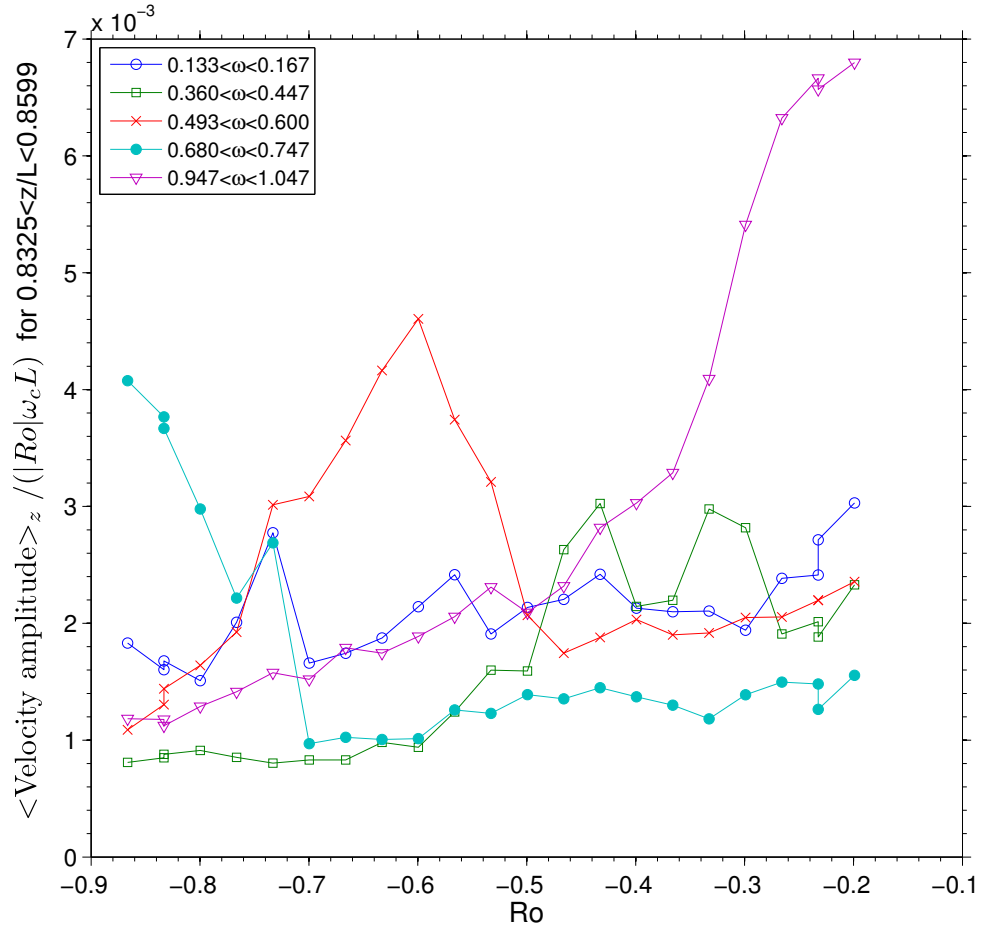


Figure 6.8: Depth-averaged velocity amplitudes (dimensionless). The average is for $0.8325 < z/L < 0.8599$ corresponding to the range 80mm - 120mm directly below the ultrasound transducer. The frequency bands are roughly the same as in Figure 6.7 except here a band near $\omega/\omega_c = 0.1$ was included. Here, velocity scale is $|Ro|\omega_c L$, $E = 4.98 \times 10^{-8}$.

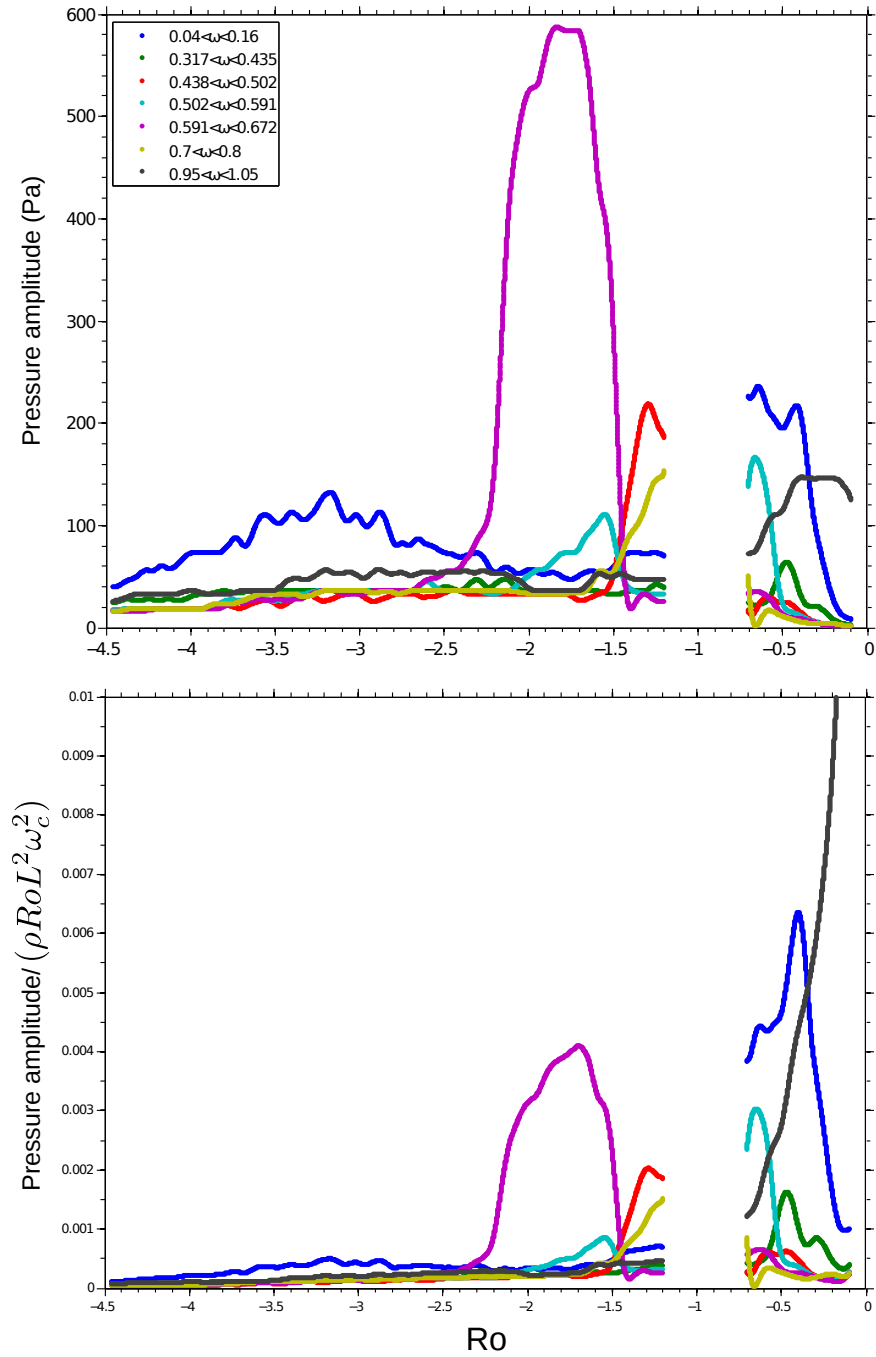


Figure 6.9: Pressure amplitudes both with physical units (top) and dimensionless (bottom) for an extended Ro ramp where we reached $Ro = -4.5$. The Ekman number is $E = 7.47 \times 10^{-8}$ corresponding to the outer sphere rotating at 1.0 Hz.

ical units and dimensionless, of an inner sphere ramp with the outer sphere at 1.0 Hz (see Figure 6.9). During this ramp we reached $Ro = -4.5$. We present both pressure magnitudes to highlight the fact that our unit pressure scale, $\rho Ro L^2 \omega_c^2$ (used to compute dimensionless magnitudes), makes the dimensionless pressure artificially high when Ro is small. This would not arise if the fluid motion becomes small as Ro reaches zero, which in principle should be the case. But as we have seen earlier in chapter 5, the fluid is still active due to the Earth's rotation. That is why in Figure 6.9 the amplitude of the frequency band around $\omega/\omega_c = 1$ grows large for small Ro while the other amplitudes stay finite.

6.3 Azimuthal wave number determination

As an illustrative example of the m number determination let us pick a region in the spectrogram in Figure 6.6 near $Ro = -0.3$ and $\omega/\omega_c = 0.3$. There we find a weak indication of a pressure oscillation at a definite frequency. If we filter the signals from the three pressure probes on ports A, B and C and examine their phase relationship, we might be able to determine the m number assuming that it is actually a single mode. In this particular case we will use a second-order digital band-pass filter with corner frequencies 0.27 and 0.33. We then compute the cross-correlation function between the filtered signals from port B and port A and also from port C and port A. Figure 6.10 shows the result. We can see that the pressure from ports A and C are, in a very rough way, 180° apart from the pressure on port B and also roughly in phase with each other. This means an $m = 2$, or even, azimuthal

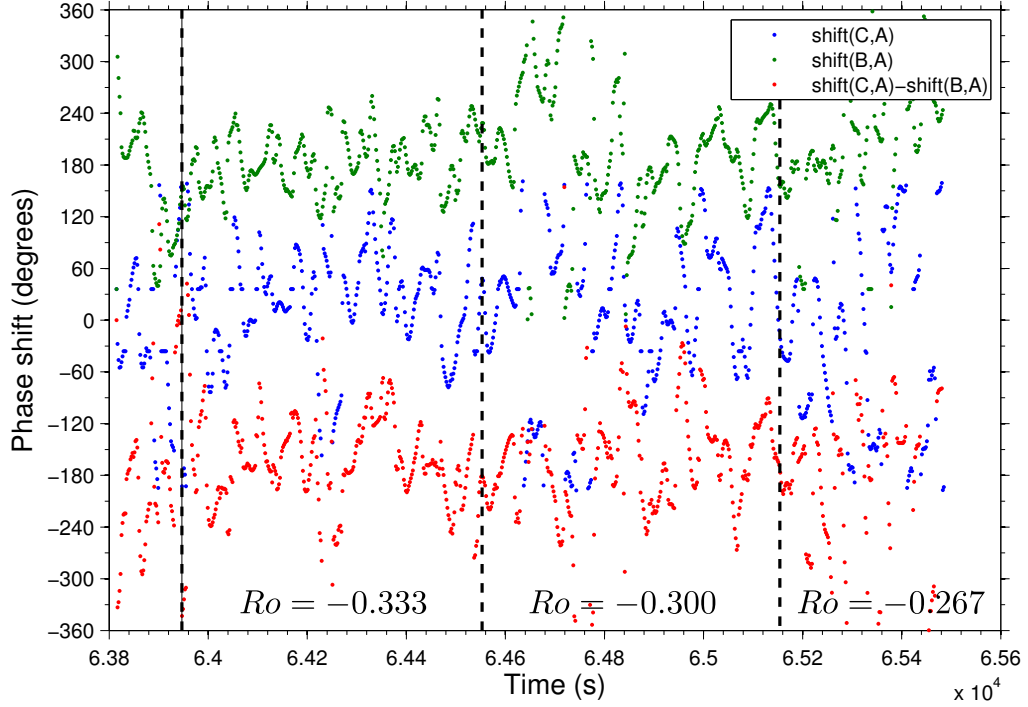


Figure 6.10: Phase shifts of the pressure signals, bandpassed around $\omega/\omega_c = 0.3$. Green dots represent the phase shift between pressure on port C and A. Blue dots correspond to the phase between B and A and the red dots to the difference. The vertical lines indicate a change in inner sphere speed. The corresponding Ro values are shown. In a rough statistical sense the oscillations resemble an azimuthal pattern with $m = 2$ or even.

pattern. We can then look up a full sphere mode with even m and a frequency close to $\omega/\omega_c = 0.3$. It turns out there are two possibilities among the low order modes: the mode ($l = 7, m = 4, \omega/\omega_c = 0.3175$) or the mode ($l = 9, m = 2, \omega/\omega_c = 0.2924$). Apart from differing spatial patterns, their main difference is the angular drift speed $(\omega/\omega_c)/m$. We will see later how this allows us to discard the ($l = 7, m = 4$) mode knowing the angular drift speed of already identified modes excited at neighboring Ro , like the mode ($l = 6, m = 3, \omega/\omega_c = 0.378$). For other

modes also manifest in the 60 cm experiment, the identification is straightforward. We will summarize the identified modes and some of their characteristics in section 6.6.

6.4 Zonal flow

The experimental determination of zonal flows is very difficult in the 3m system given the long time scales involved. In order to have an acceptable ultrasound signal we need particles to stay suspended for several hours. The smaller the particle the longer it stays suspended, but the weaker the echo reflections. Any density mismatch between the particles and the fluid will be noticed after several minutes. By using repeated particle injections pointed directly down (vertically) from the ultrasound probes we were able to capture acceptable velocity profiles along the z direction near the transducer. When we used the special probe arrangement as described in chapter 3, particle injection was not particularly successful primarily due to Coriolis forces deflecting the particle stream away from the ultrasound beam. Nevertheless, we were fortunate enough to obtain some information for the mode $l = 7, m = 2$ excited when $Ro = -0.4$. Figure 6.11 shows a space-time diagram capturing approximately eight fluid oscillation cycles, the left half of the figure corresponds to velocities obtained with a transducer oriented down and West-ward (in the $-\hat{\phi} - \hat{z}$ direction). The other half corresponds to a transducer oriented down and East-ward (in the $\hat{\phi} - \hat{z}$ direction). Positive velocities indicate flow away from the transducers.

By taking time averages we can get an estimate of the mean flow as measured

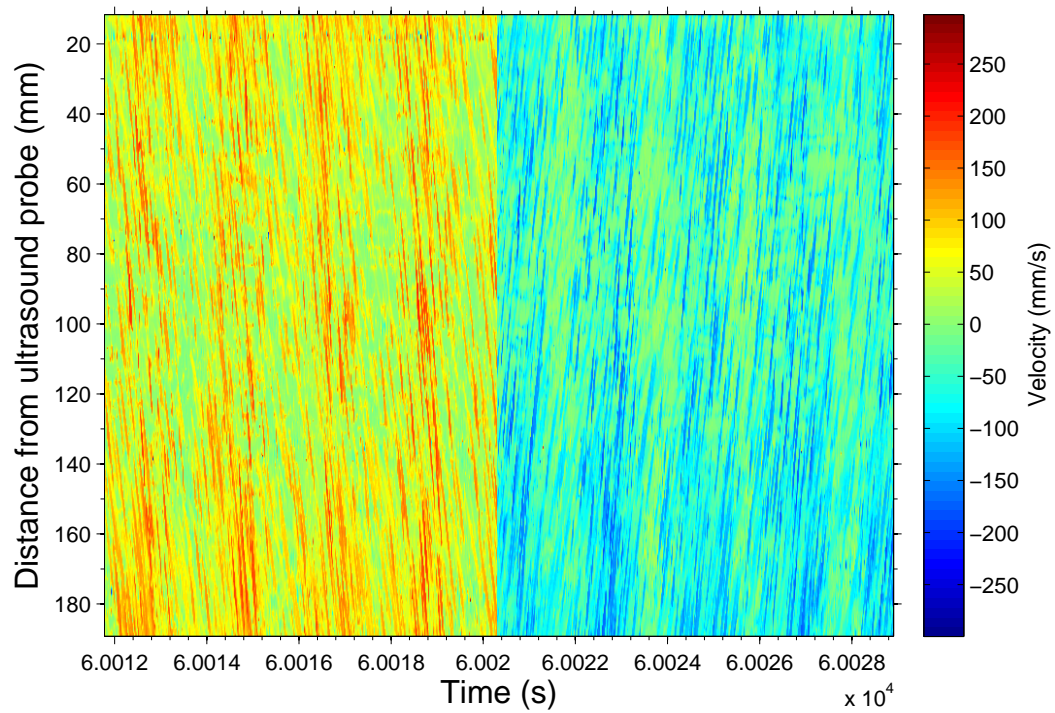


Figure 6.11: Space-time diagram of flow velocities as measured from two ultrasound transducers on port D, oriented perpendicularly to each other. Left half corresponds to the transducer oriented West-ward and down. The other half corresponds to the transducer oriented East-ward and down. Here positive velocities indicate flow away from the transducers. Note the difference between the mean velocities from each transducer orientation.

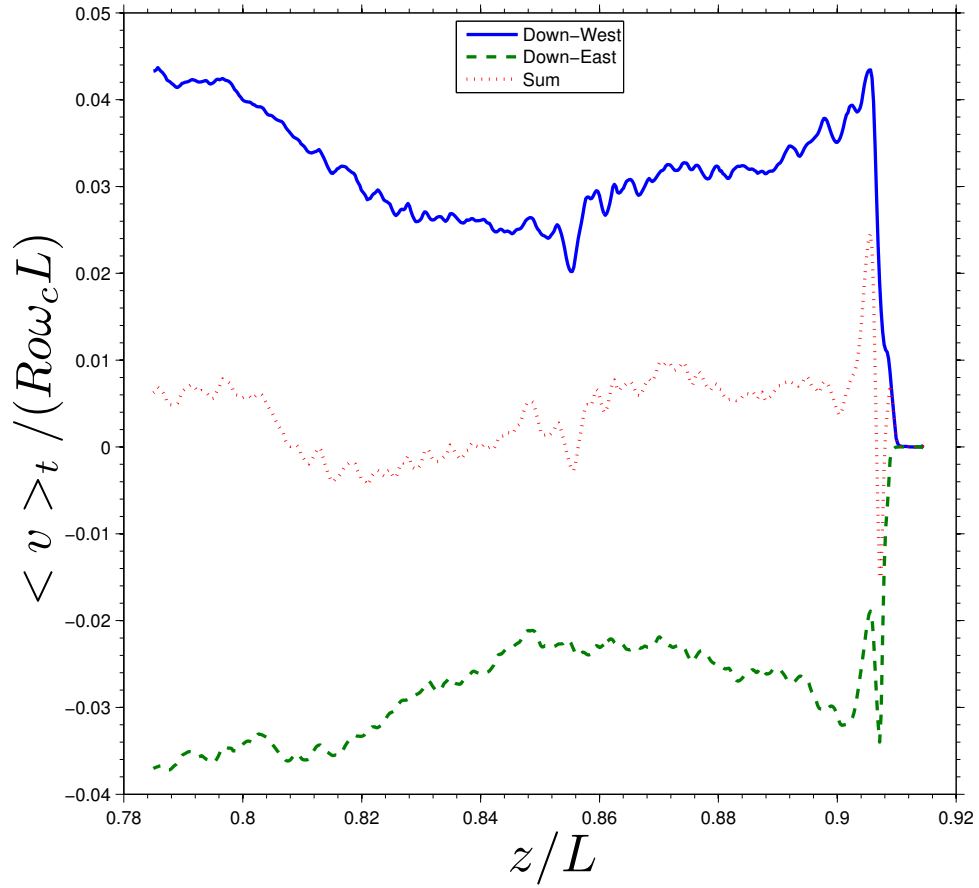


Figure 6.12: Time averaged velocities (dimensionless) as measured from the two ultrasound transducers perpendicular to each other. The flow is mostly azimuthal since the sum of the averages is small compared to the averages themselves.

from each transducer. Figure 6.12 shows such averages for both transducers. Since the two transducers are oriented perpendicular to each other, the fact that the sum of the two averages is relatively small compared to the averages themselves indicates that the mean flow is mostly azimuthal. For comparison the dimensionless tangential velocity at the equator of the inner sphere is 0.525 at this value of Ro .

6.5 Decay times

Two of the excited modes are relatively strong, particularly the $l = 4, m = 1$, $\omega/\omega_c = 0.612$ mode as shown earlier. We can suitably study their decay time if the inner sphere differential rotation is suddenly stopped. This by no means implies a free decay given the strong azimuthal flows present. The inner sphere usually stops within 10 seconds after the motor is made to coast freely. Friction from the lip seals and bearings then keep the inner sphere rotating in unison with the outer. Given the differential rotation background and turbulence in which the modes live, we do not expect to match the viscous decay times as calculated from theory. Table 6.1 lists the experimental decay times and the theoretical using expression 2.9.12 from Greenspan [10]. The dimensionless decay factor is $\sigma = -(E^{1/2}\tau\omega_c)^{-1}$ where τ is the typical time of decay (in seconds) as measured experimentally.

We estimate the instantaneous amplitude (of the pressure or velocity) by calculating the absolute value of the Hilbert transform of the measured (and band pass filtered) time series. The decay is roughly exponential but there is also substantial amplitude modulation. Figure 6.13 shows an example for the (4,1) mode when

Table 6.1: Decay factors

		Decay factor σ	
(l, m)	ω/ω_c	Theory	Experiment
(4,1)	0.612	-3.948	-18 ± 4
(3,2)	0.667	-3.518	-10 ± 5

$Ro = -2$ and $E = 1.867 \times 10^{-7}$.

6.6 Inertial mode ordering

The observed modes can be ordered according to the Rossby number Ro at peak power. Note that the range of Ro studied in this work always involves the inner sphere rotating in the retrograde direction as seen from the outer sphere reference frame. As we pointed out earlier, our Rossby number Ro corresponds to the dimensionless angular speed of the inner sphere as seen from the rotating outer sphere. Perhaps not surprisingly, all the modes observed are also retrograde. Their angular drift speed $(\omega/\omega_c)/m$ is negative. In fact, the angular drift speed and Ro are intimately related: for a given small range of Ro the only modes excited are those with similar angular drift speeds. Table 6.2 lists all the modes observed, ordered according to Ro . The angular drift is based on the observed frequency.

The mode (5,4) (next to last) was very weak, although its signature in the 60 cm experiment is clearer. The last mode is very weak in both 3m and the 60

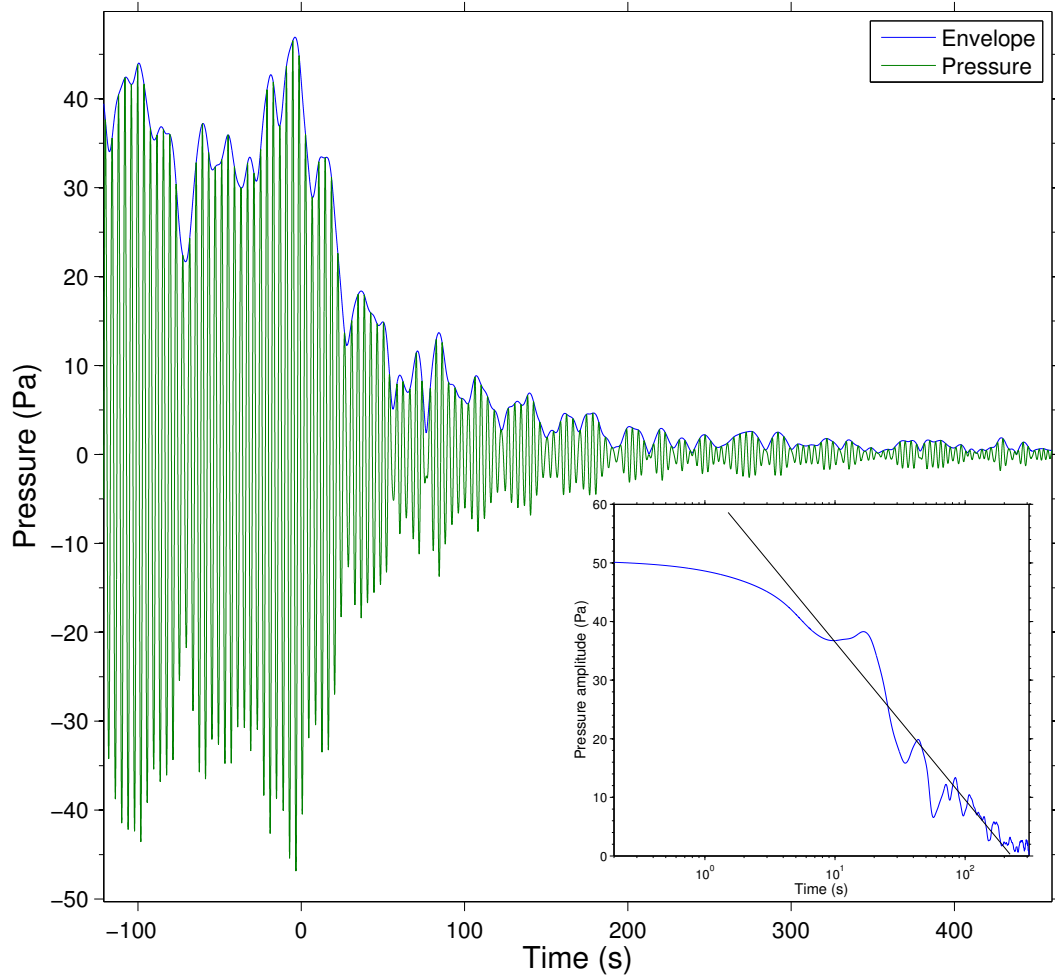


Figure 6.13: Pressure (in Pa) at port A showing the decay of the (4,1) mode. The inner sphere is allowed to coast and spin with the outer sphere at $t = 0$. Here $Ro = -2$ and $E = 1.867 \times 10^{-7}$. A least squares estimate of the decay time is 57 s. The envelope is the magnitude of the Hilbert transform of the pressure signal. The decay is roughly exponential as the inset semilog plot shows.

Table 6.2: Inertial modes observed

(l, m)	ω/ω_c	ω_{meas}/ω_c	$(\omega_{meas}/\omega_c)/m$	$ Ro $ range
(4,1)	0.6120	0.639 - 0.605	0.639 - 0.605	2.20 - 1.42
(6,1)	0.4405	0.500 - 0.444	0.500 - 0.444	1.4 - >0.8
(3,2)	0.6667	0.760 - 0.700	0.380 - 0.350	1.25 - 0.70
(8,1)	0.3440	0.356 - 0.346	0.356 - 0.346	0.83 - 0.77
(5,2)	0.4669	0.573 - 0.508	0.286 - 0.254	0.77 - 0.50
(7,2)	0.3595	0.407 - 0.381	0.190 - 0.183	0.50 - 0.37
(4,3)	0.5000	0.512 - 0.511	0.171 - 0.170	0.40 - 0.33
(9,2)	0.2924	0.312 - 0.295	0.156 - 0.147	0.37 - 0.27
(6,3)	0.3779	0.418 - 0.404	0.139 - 0.135	0.33 - 0.27
(8,3)	0.3040	0.340 - 0.332	0.113 - 0.107	0.27 - 0.20
(5,4)	0.4000	0.398	0.0995	0.23 - 0.20
(7,4)	0.3175	0.299	0.075	0.20

cm experiment. In addition to the nine modes originally detected in the 60 cm experiment we have now the (8,1), (9,2) and (8,3) modes. As we explained earlier the m number determination from pressure measurements is ambiguous if m is even and the corresponding mode signature in the 60 cm experiment is lacking. In our example analyzing the (9,2) mode (section 6.3), the observed ordering according to $(\omega_{meas}/\omega_c)/m$ matching the ordering according to Ro for all the other modes, suggests that the mode appearing close (in Ro) to the (4,3) mode is the (9,2) instead

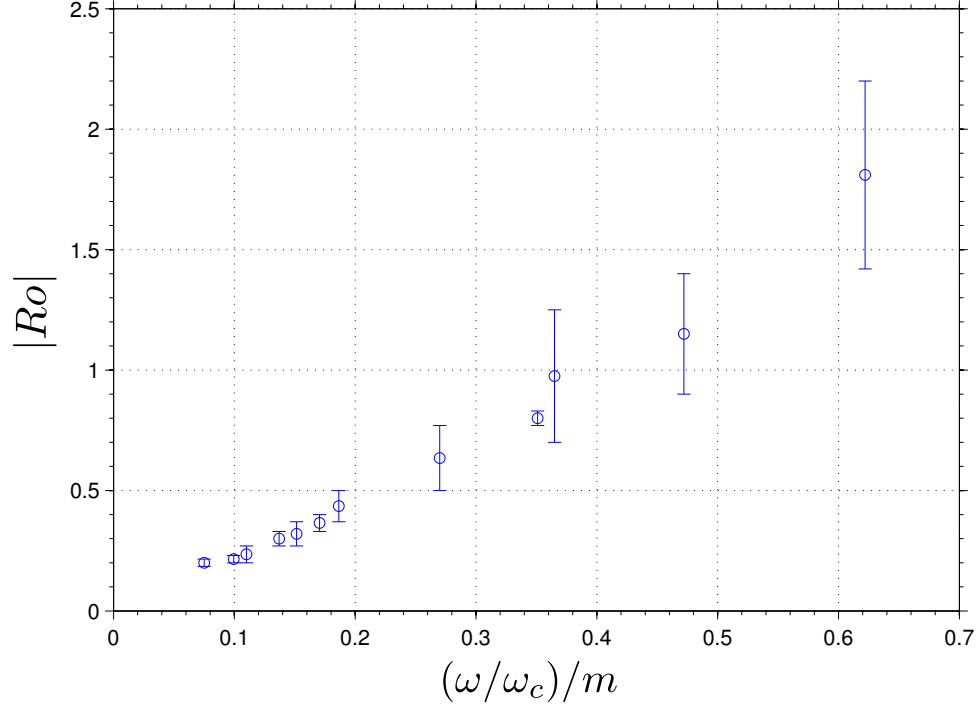


Figure 6.14: The order in which the inertial modes appear is related to their angular drift speed $(\omega/\omega_c)/m$. Error bars here correspond to the range of Ro where each mode gets excited. This graph also shows that the ranges decrease more or less monotonically with $(\omega/\omega_c)/m$.

of the (7,4), as the latter has a drift $(\omega_{meas}/\omega_c)/m$ just half (approximately) of the drift of either the (4,3) or (9,2) mode. Figure 6.14 shows a plot of Ro versus $(\omega/\omega_c)/m$.

Note that $l - m$ is always odd, i.e., the flow patterns are anti-symmetric with respect to the equator. This is puzzling since the forcing through the inner sphere rotation is symmetric with respect to the equator. We will return to this in the discussion section.

6.7 Spectral power scaling

We now compare the power spectral density S of the pressure oscillations at a fixed Ro and varying E . We chose again $Ro = -2$ in order to have a strong (4,1) mode component. We computed S from a time series of the measured pressure, which makes S to have units of Pa^2/Hz . A dimensionless power spectral density would be $S' = S\omega_c/(\rho RoL^2\omega_c^2)^2$, where ω_c is the rotation rate, in rad/s, of the vessel (recall from section 2.2 that the unit time scale is $1/\omega_c$ and the unit pressure scale is $\rho RoL^2\omega_c^2$). Figure 6.15 shows a plot of the dimensionless power spectral density S' of the pressure versus ω/ω_c . The collapse of the spectral curves for different E onto a single curve shows that the dimensionless spectral power S' is independent of E . We think this result will hold true for other values of Ro although this was not tested during the present study. The peak dimensionless power of the mode seems to be independent of E although additional data spanning wider ranges of E are needed to get a more accurate scaling. Another feature of interest is the power law scaling for frequencies $\omega/\omega_c > 2$. In this range inertial modes do not exist; the flow is purely potential, i.e, the Navier-Stokes equation becomes a Laplace problem. The power law exponent is close to -3, which is reminiscent of the direct enstrophy cascade in two-dimensional flows. If high frequency oscillations correspond to small scale motions, then the Taylor-Proudman theorem might be close to being applicable in this range, i.e. the flow might be close to being two-dimensional.

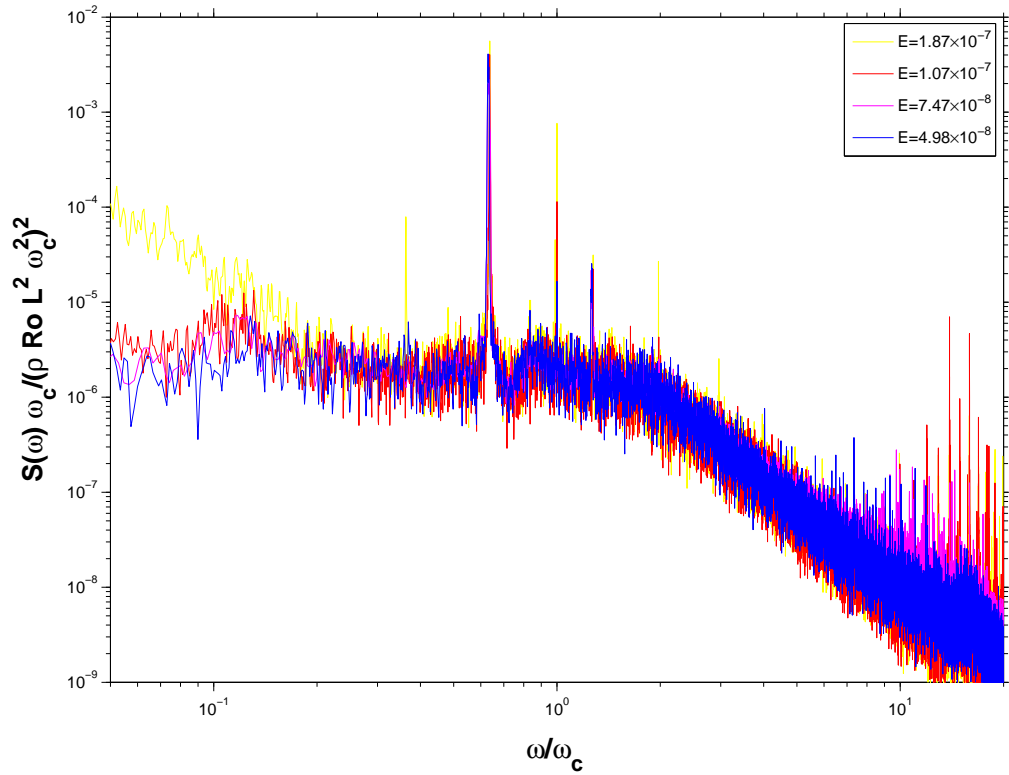


Figure 6.15: The dimensionless power spectral density $S(\omega)\omega_c/(\rho RoL^2\omega_c^2)^2$ of the pressure is independent of E . The peak power of the mode (4,1) here seems to be independent of E as well. The quantity $\rho RoL^2\omega_c^2$ is the unit pressure scale.

6.8 Discussion

Let us begin with a brief discussion of the mechanism believed to be responsible of the mode excitation. An overview is given in section 2.5 which contains concepts and definitions relevant to the discussion in this section. In [13] we discussed the possibility that an over-reflection mechanism causes the excitation of the different modes we observed in the 60 cm sodium experiment. We postulated the existence of a shear layer such that inertial waves could be reflected with a larger amplitude, extracting energy from the shear. In that study, it is assumed that the Mach number M is the ratio of the inner sphere angular speed to angular drift, or phase speed, of the mode (as seen from the outer sphere rotating frame). The critical angle θ_c (see section 2.3 for a definition) is *assumed* to be the incidence angle of some inertial wave onto a cylindrical shear layer. We should note that the over-reflection formulae have been borrowed from sound wave theory with no modifications addressing the particular reflection law of inertial waves. Although we can certainly imagine a shear layer, it is conceptually difficult to picture an incident inertial wave with a wave number \mathbf{k} , with phase speed $(\omega/\omega_c)/m$ in the $\hat{\phi}$ direction that also makes an angle θ_c with an (assumed cylindrical) shear layer.

To the best of our knowledge, conditions for over-reflection of *plane* inertial waves are yet to be derived (although there is some literature considering over-reflection of Rossby waves and internal waves). A preliminary attempt at this task by the author anticipates that a plane inertial wave cannot over-reflect from a vertical shear layer between two regions of fluid if the only relative motion has no vertical

component (assuming a vertical rotation axis). This can already be seen in the case of over-reflection of plane sound waves if the incident wave vector, and the velocity of the moving medium are perpendicular to each other (see Chapter 2, equation 2.26).

The experimental results described here elucidate and extend the previous results from the 60 cm sodium experiment. Several other modes have been identified, and distinguishing features of the mode family seem to emerge. One conclusion is the ordering of the modes according to their drift speed $(\omega/\omega_c)/m$ as the Rossby number Ro is varied, a hard to observe fact when we only had a few modes.

Another very interesting feature of the modes observed is their internal structure (see Appendix A). All modes seem to organize in vertical cells ranging from only one, like modes (3,2), (4,3) and (5,4), or three cells with the one in the middle circulating around the inner sphere like modes (4,1), (5,2), (6,3) and (7,4), or five cells like modes (6,1), (7,2), or (8,3), even going up to seven cells like modes (8,1) and (9,2). Actually, in the complete set of inertial modes for a full sphere, specifying l and m does not suffice to specify a mode (see Chapter 2). Of the possible frequencies for given (l, m) we observed only the smallest retrograde one for that set. In Figure A.4 we can see the rather different flow structure corresponding to the other frequencies. It is hard not to see the pattern: only modes with $l - m$ odd and vertical cells are excited.

In a recent paper [42] Rieutord and Valdettaro reported results on numerical computations of a tidally forced fluid shell, reaching Ekman numbers down to 10^{-8} . The fluid velocity in that study is expressed using poloidal and toroidal decomposi-

tion as

$$\mathbf{u} = \sum_{l,m} u_l^m(r) \mathbf{R}_l^m + v_l^m(r) \mathbf{S}_l^m + w_l^m(r) \mathbf{T}_l^m, \quad (6.3)$$

where

$$\mathbf{R}_l^m = Y_l^m(\theta, \phi) \hat{\mathbf{r}}, \quad \mathbf{S}_l^m = \nabla Y_l^m(\theta, \phi), \quad \mathbf{T}_l^m = \nabla \times \mathbf{R}_l^m. \quad (6.4)$$

Rieutord noted (private communication) that if no external forcing is included, and setting $w_m^m(r_{outer}) = 1$, the energy spectrum reveals a series of peaks that match to modes present in the 3m experiment. Although setting $w_m^m(r_{outer}) = 1$ already assigns an m -fold symmetry to the flow the result is still in remarkable agreement with our observations. Note that this numerical work does not predict what modes are populated for a range of Ro . It seems that for a given m the numerical solution exhibits several modes coexisting at the same time all with same m -fold symmetry.

The ordering, structure and symmetry of the modes observed seem to suggest a simple underlying mechanism that need not be different from over-reflection (simple here might not mean mathematically simple!). In fact it has been shown in the context of Rossby waves that over-reflection and the barotropic instability are intimately related [19]. Moreover, there is at least one experimental report documenting the appearance of shallow-water modes excited by over-reflection in a differentially rotating basin [23]. These two studies suggest that over-reflection is indeed a rather general phenomenon and can arise in rotating fluids. Further analytical research in this area might prove insightful and fruitful.

In light of the preceding, the details of the mode excitation mechanism are still not well understood, although it seems that the regularities discovered will soon

lead us to identify clearly their physical origin.

The origin of the wide peak around $\omega/\omega_c = 0.1$ is unknown. It does not comply with the common characteristics the other 12 modes exhibit. It might be a mode found exclusively in a spherical shell as opposed to a full sphere. Or it could be a superposition of many modes. It seems that these low-frequency oscillations appeared as well in the spherical shell experiments by Schaeffer [47].

A quantitative result regarding the expected scaling of the power spectrum has been established. This is particularly useful since it predicts the mode amplitudes for other spherical shell devices operating at different Ekman numbers, given known amplitudes at other parameter ranges. It is potentially applicable to the interior of planets or stars in which a differentially rotating interior might drive large-scale inertial modes.

The internal shear layers are not revealed by our velocimetry measurements. The stability character of the internal shear layers is unknown and one might wonder if they actually survive the large azimuthal (and turbulent) flow imposed by the inner sphere. All numerical simulations show that these internal shear layers exist and concentrate most of the kinetic energy of the mode. The flow in the 60 cm sodium experiment, imaged magnetically, does not seem to offer any clue regarding their existence. Perhaps their spatial extent is too small to be picked up by the Hall probe array. Or they might not be there, distorted or swamped by the turbulent azimuthal flow from the inner sphere. As we have seen, all of our differential-forcing measurements indicate a flow very much like the inviscid spherical modes; no sharp shear layers appear in the data. This is contrast with the precession-induced flow, in

which we were able to resolve a small section of one of the internal shear layers. But precession forcing is considerably ‘gentler’ than differential rotation, and the shear layers might be present under the relatively weak turbulent background induced by precession. If this is the case, we then would like to know under what conditions the shear layers become unstable. This is certainly an interesting issue and we hope to encourage further research on this matter.

Appendix A

Analytical flow structures

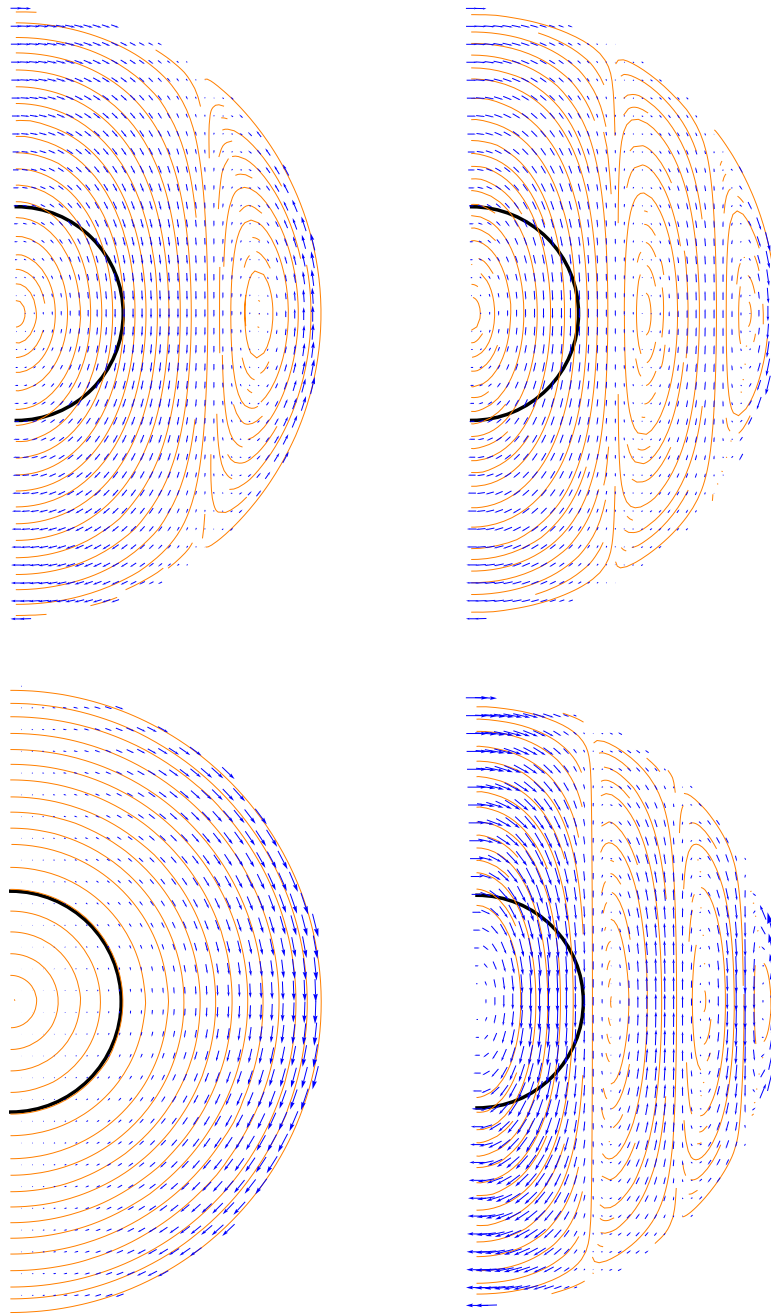


Figure A.1: $\mathbf{u}_s + \mathbf{u}_z$ at maximum amplitude for mode (4,1) (top left), mode (6,1) (top right), mode (3,2) (bottom left) and mode (8,1) (bottom right). Orange lines are approximate streamlines.

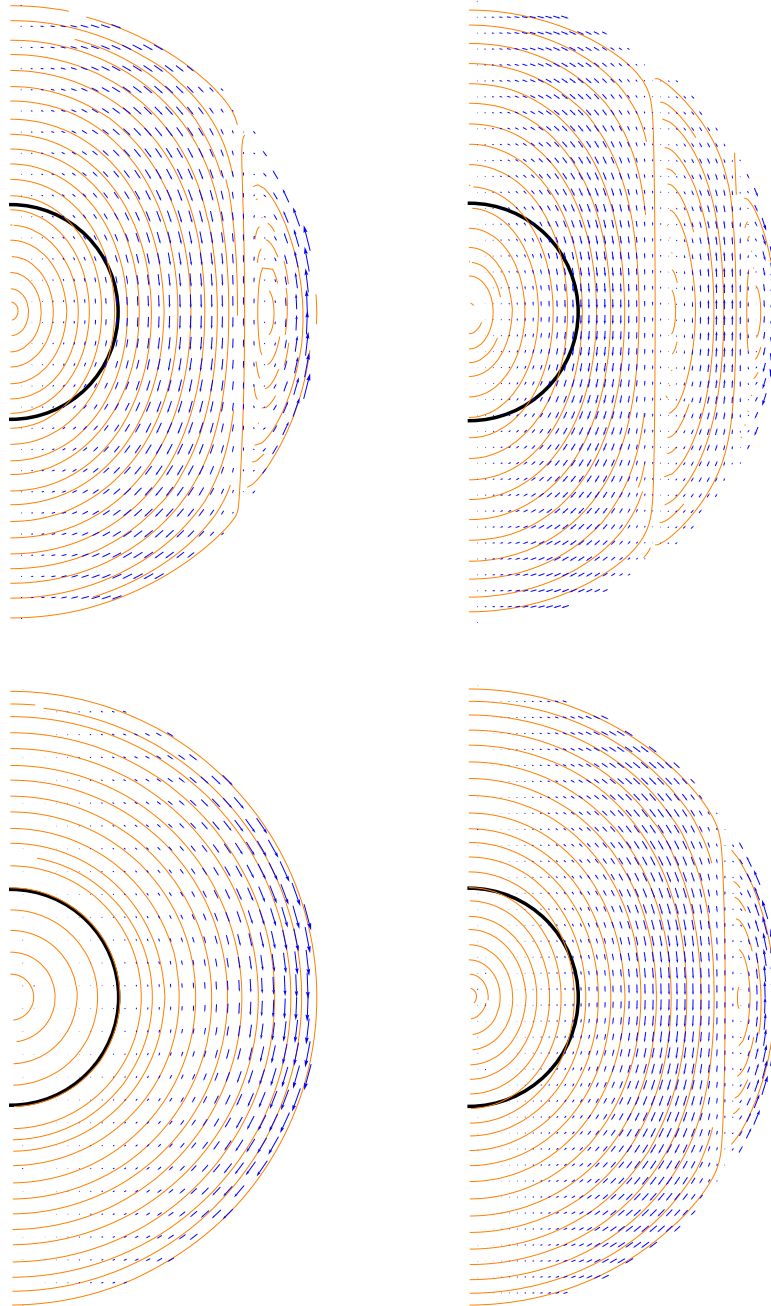


Figure A.2: $\mathbf{u}_s + \mathbf{u}_z$ at maximum amplitude for mode (5,2) (top left), mode (7,2) (top right), mode (4,3) (bottom left) and mode (6,3) (bottom right). Orange lines are approximate streamlines.

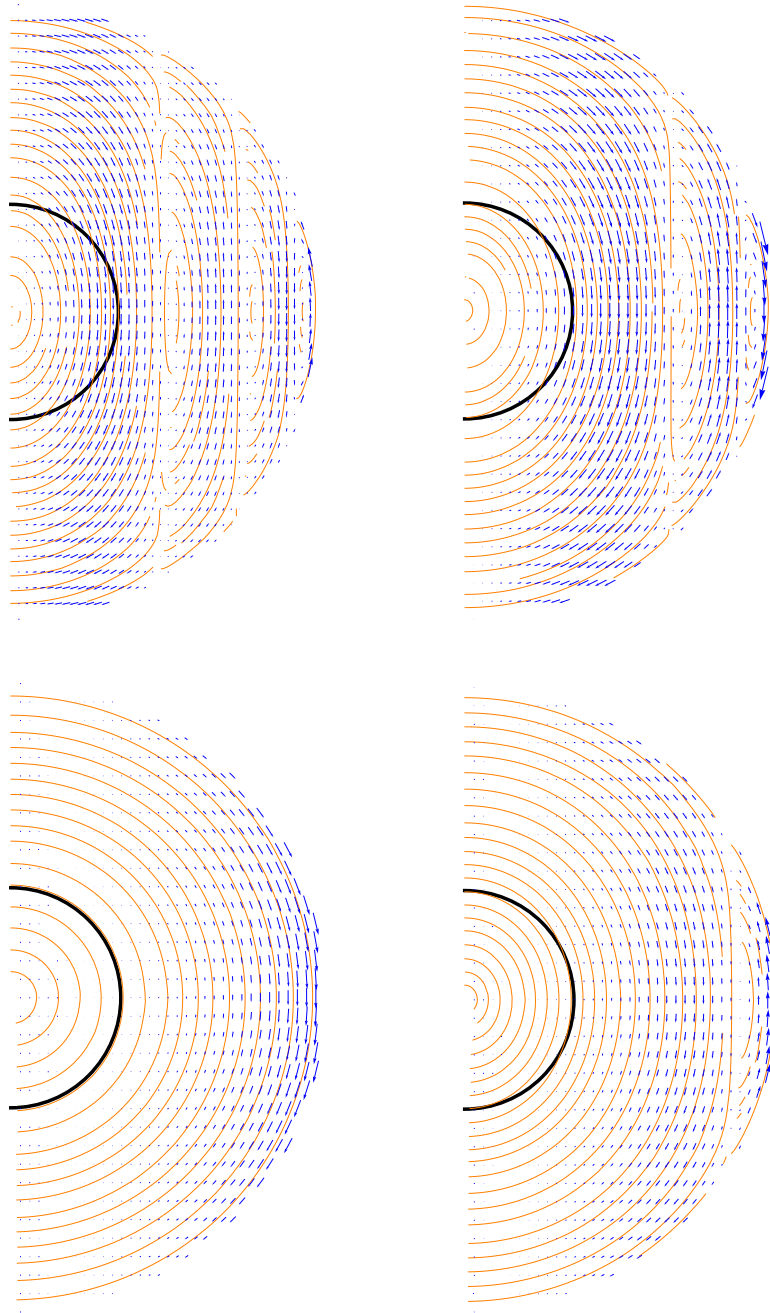


Figure A.3: $\mathbf{u}_s + \mathbf{u}_z$ at maximum amplitude for mode (9,2) (top left), mode (8,3) (top right), mode (5,4) (bottom left) and mode (7,4) (bottom right). Orange lines are approximate streamlines.

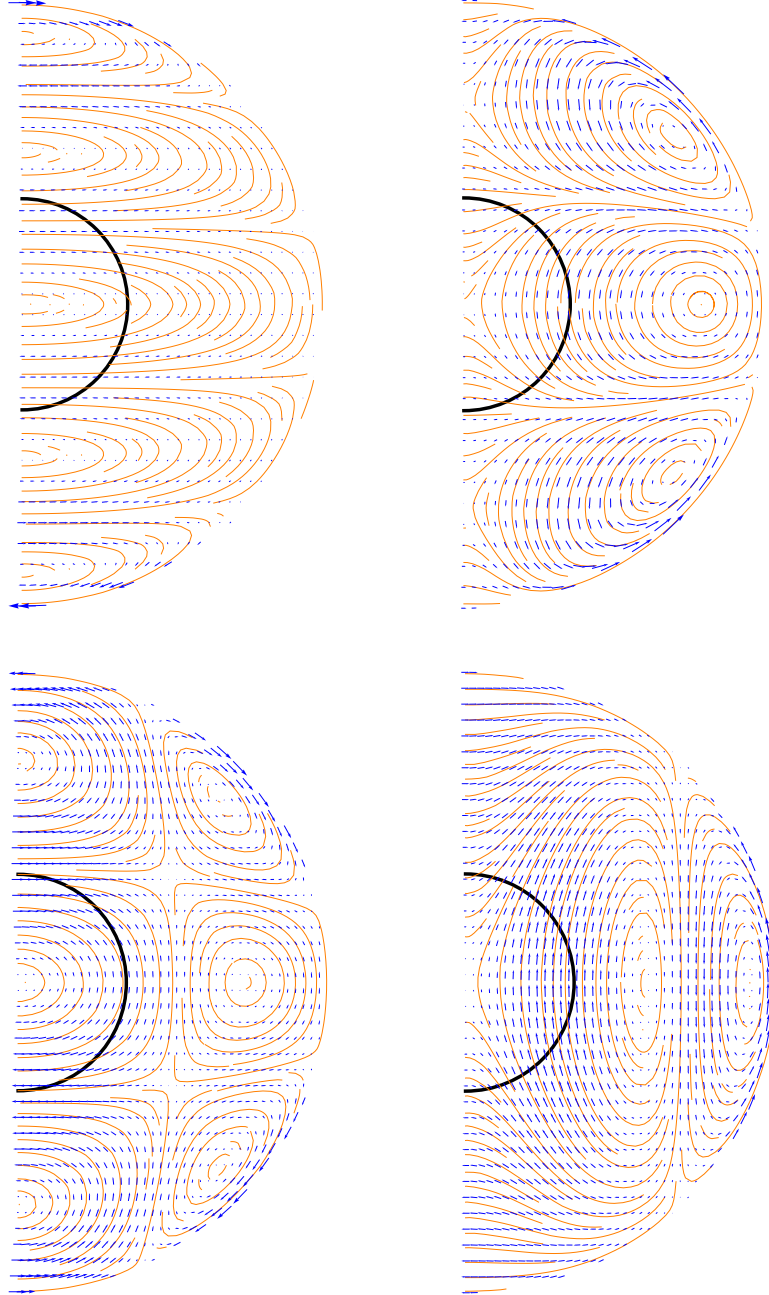
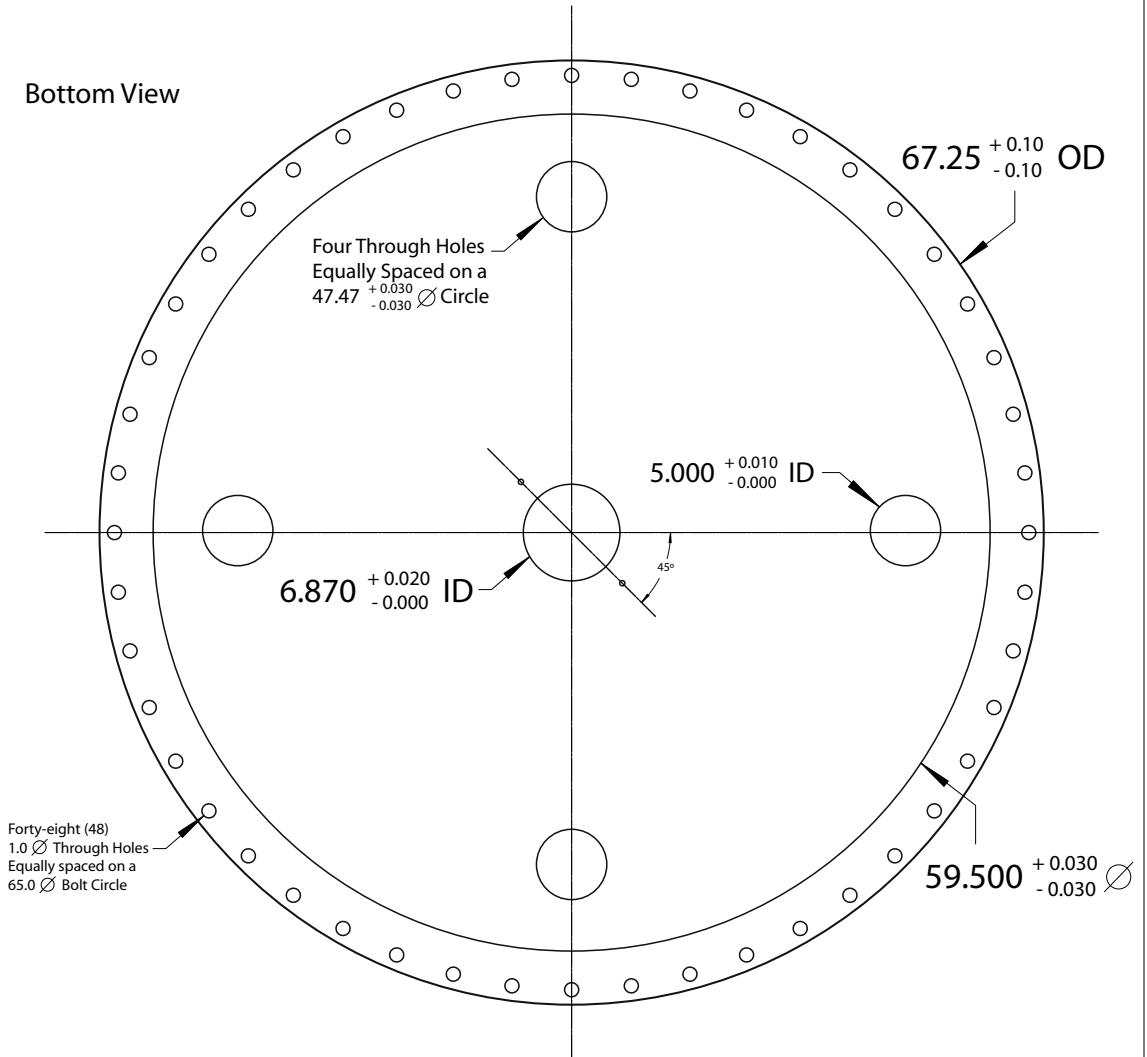


Figure A.4: $\mathbf{u}_s + \mathbf{u}_z$ at maximum amplitude for modes with $l = 6$ and $m = 1$, labeled according to their frequency. The modes shown in this Figure are not excited by differential rotation of the inner sphere. Their frequencies are $\omega = 1.8617$ (top left), $\omega = -1.4042$ (top right), $\omega = 1.3061$ (bottom left) and $\omega = -0.5373$ (bottom right). The last member of this family not displayed here is the mode with $\omega = 0.4405$ which do gets excited. It corresponds to the mode shown on top, right in Figure A.1

Appendix B

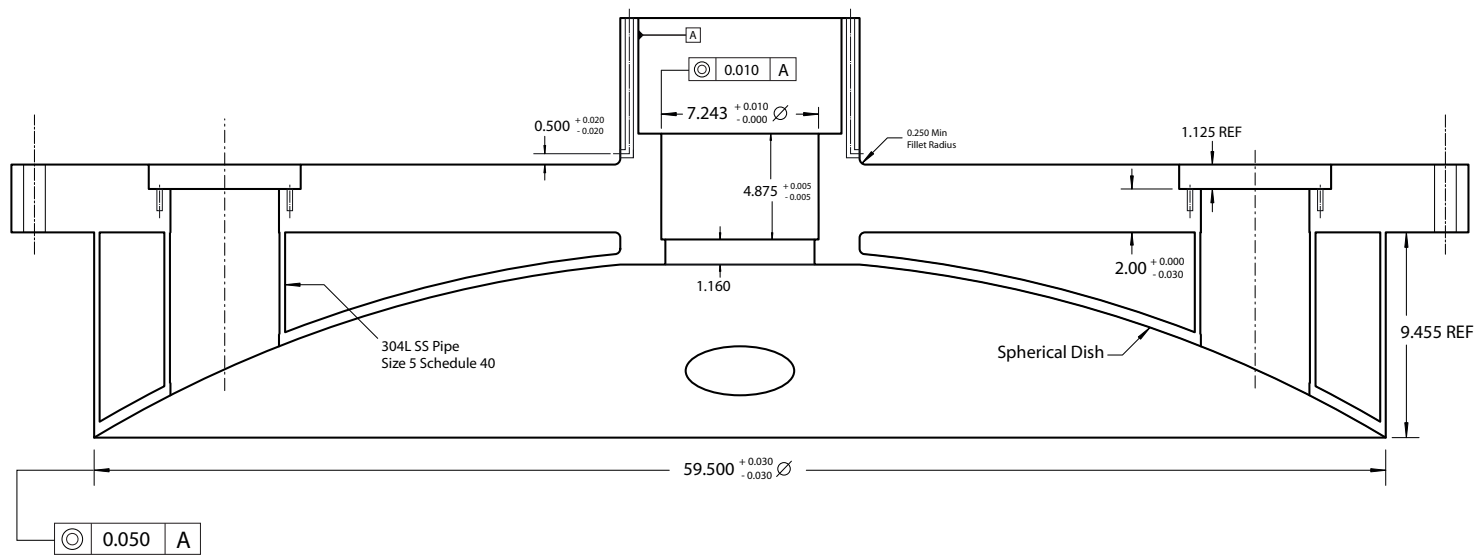
Technical drawings

Bottom View

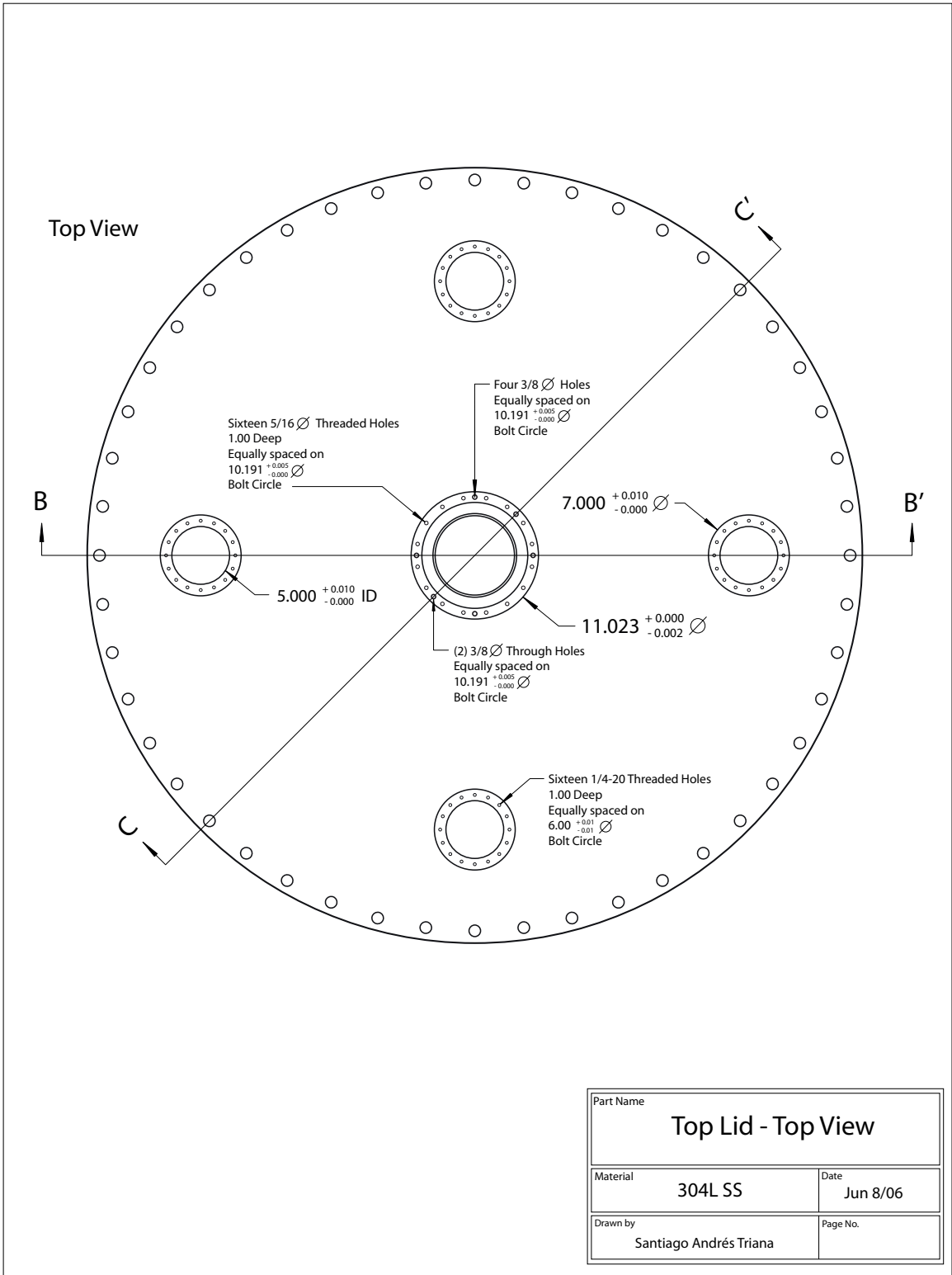


Part Name	
Top Lid - Bottom View	
Material	Date
304L SS	Jun 8/06
Drawn by	Page No.
Santiago Andrés Triana	

Section BB'

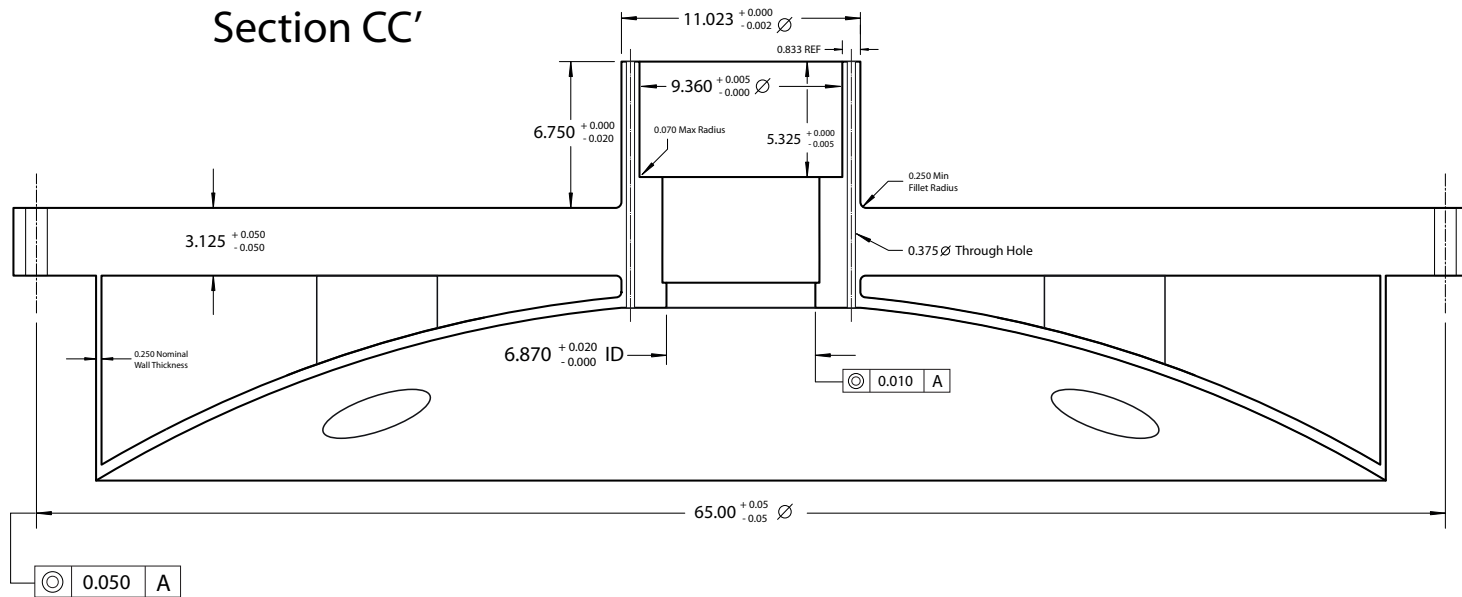


Part Name	
Top Lid - Section BB'	
Material	Date
304L SS	Jun 8/06
Drawn by	Page No.
Santiago Andrés Triana	

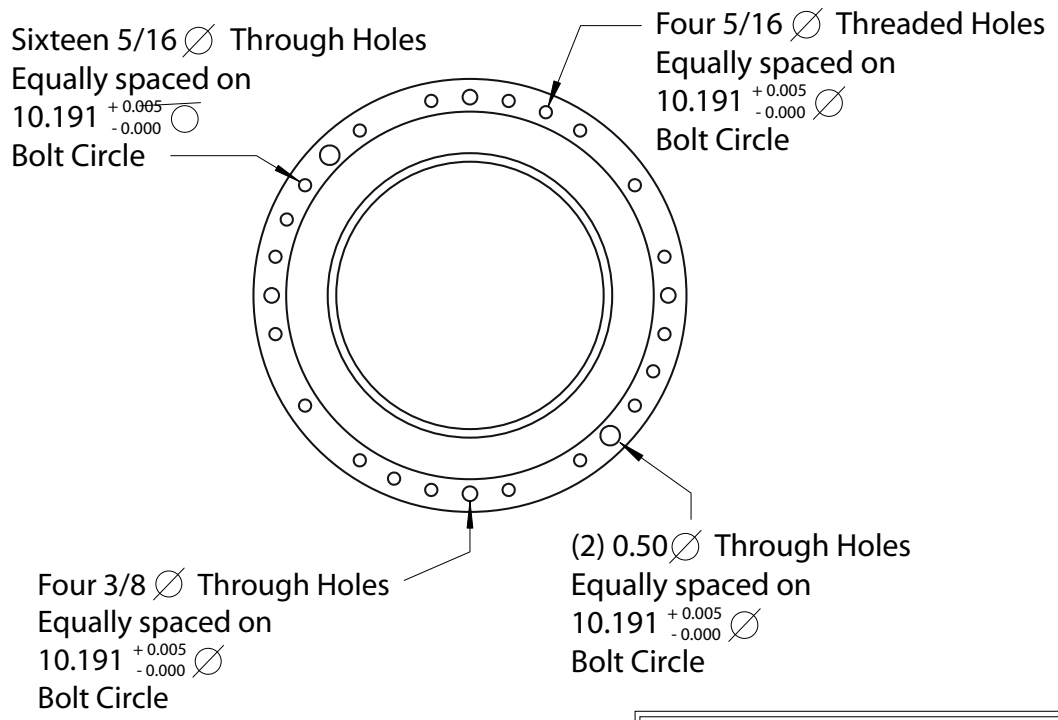
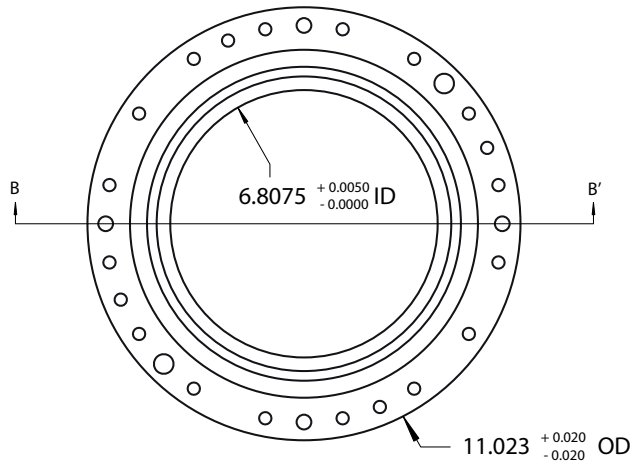


140

Section CC'

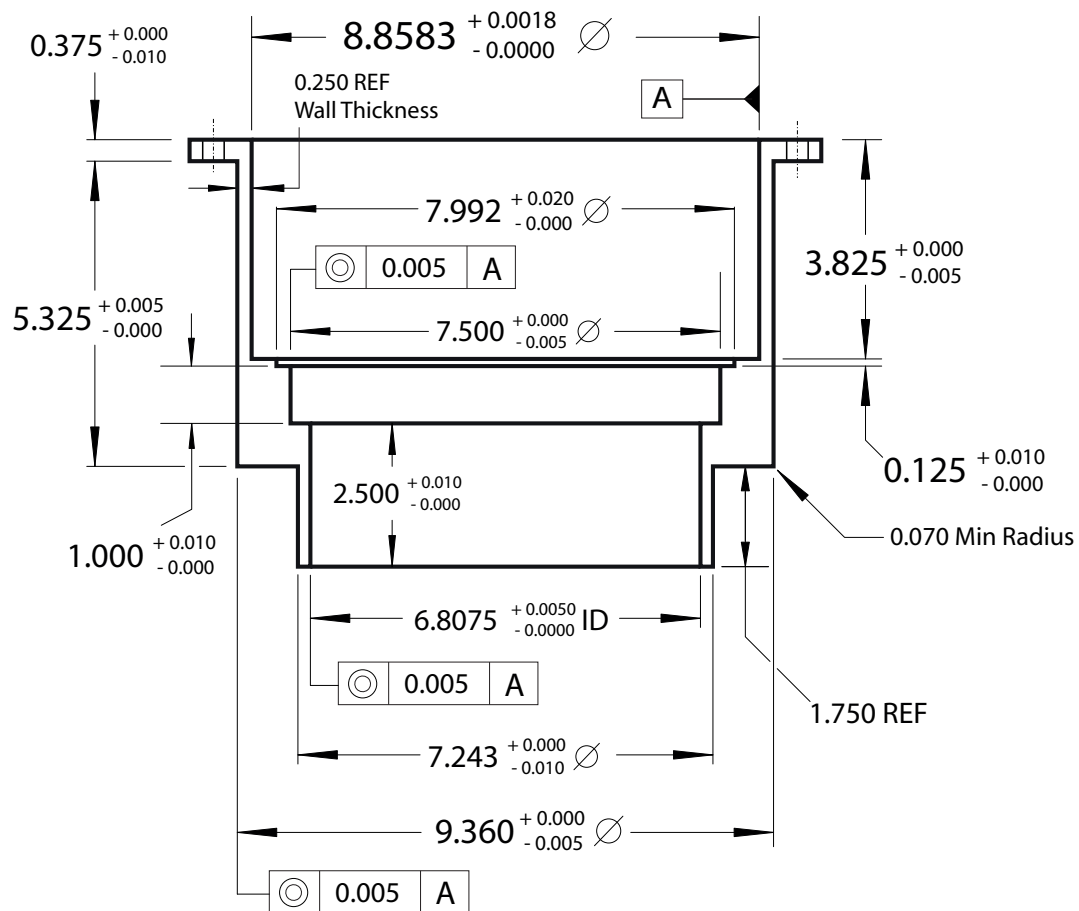


Part Name	
Top Lid - Section CC'	
Material	Date
304L SS	Jun 8/06
Drawn by	Page No.
Santiago Andrés Triana	

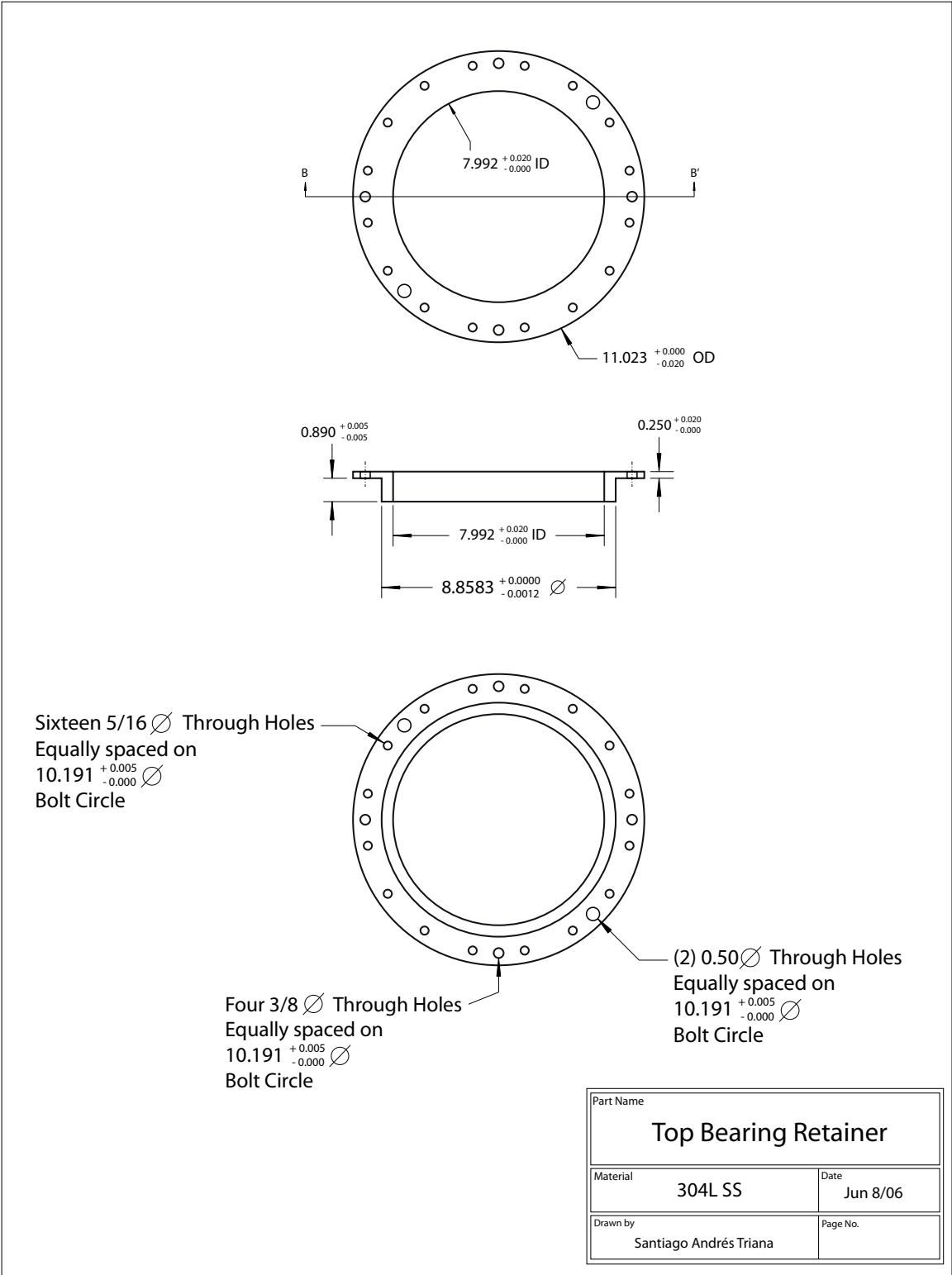


Part Name		Top Bearing seat	
Material	304L SS	Date	Jun 8/06
Drawn by	Santiago Andrés Triana	Page No.	

Section BB'



Part Name	
Top Bearing Seat - Section BB'	
Material	Date
304L SS	Jun 7/06
Drawn by	Page No.
Santiago Andrés Triana	

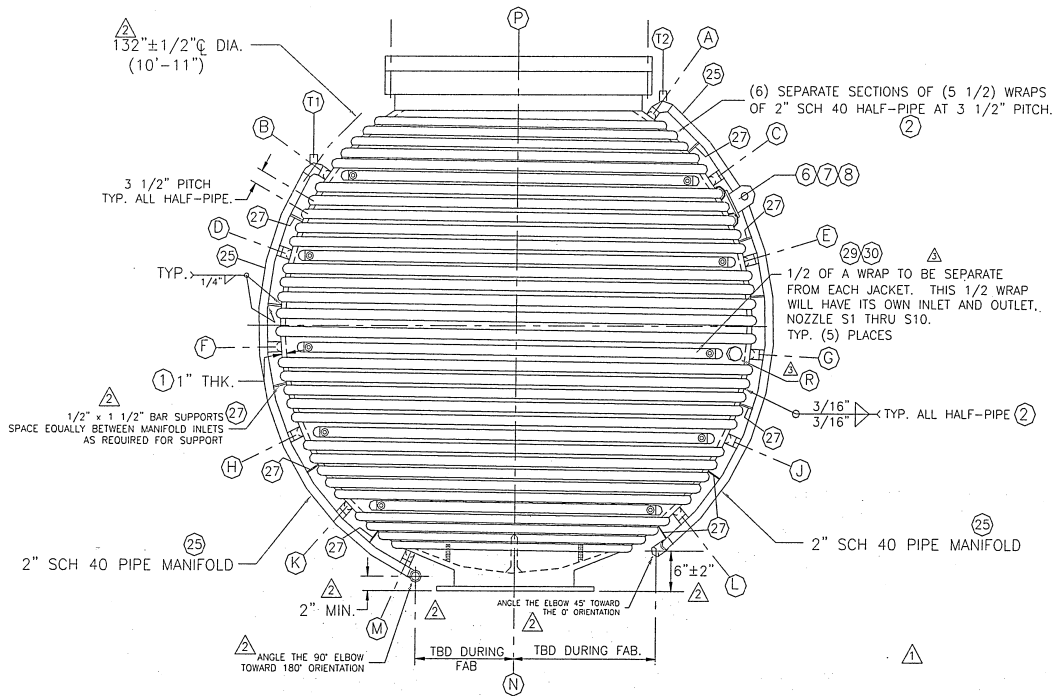
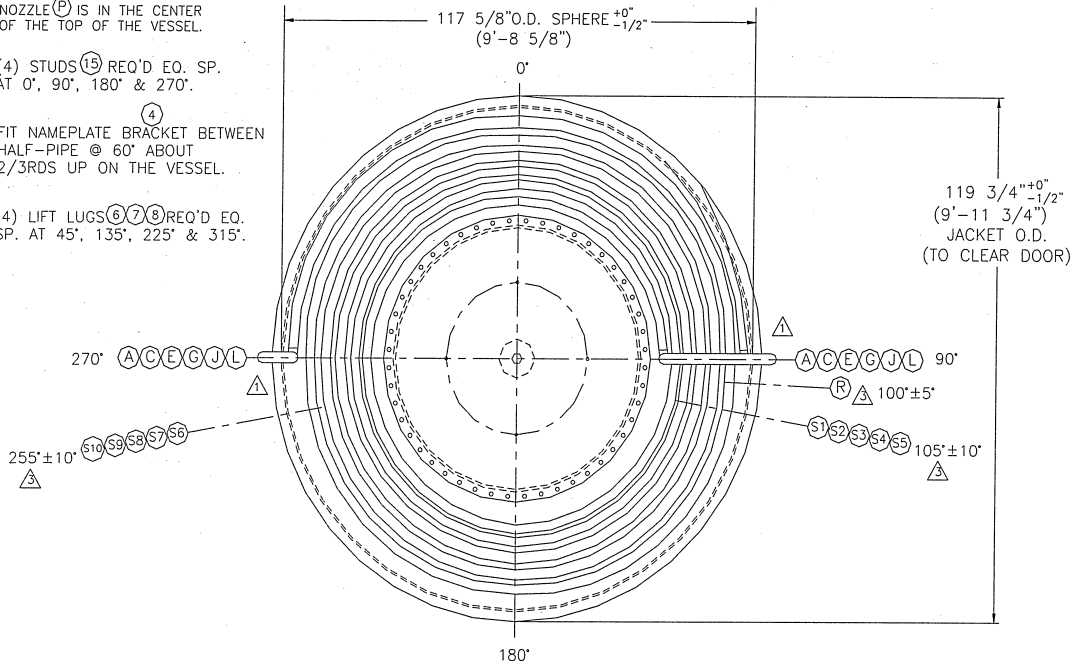


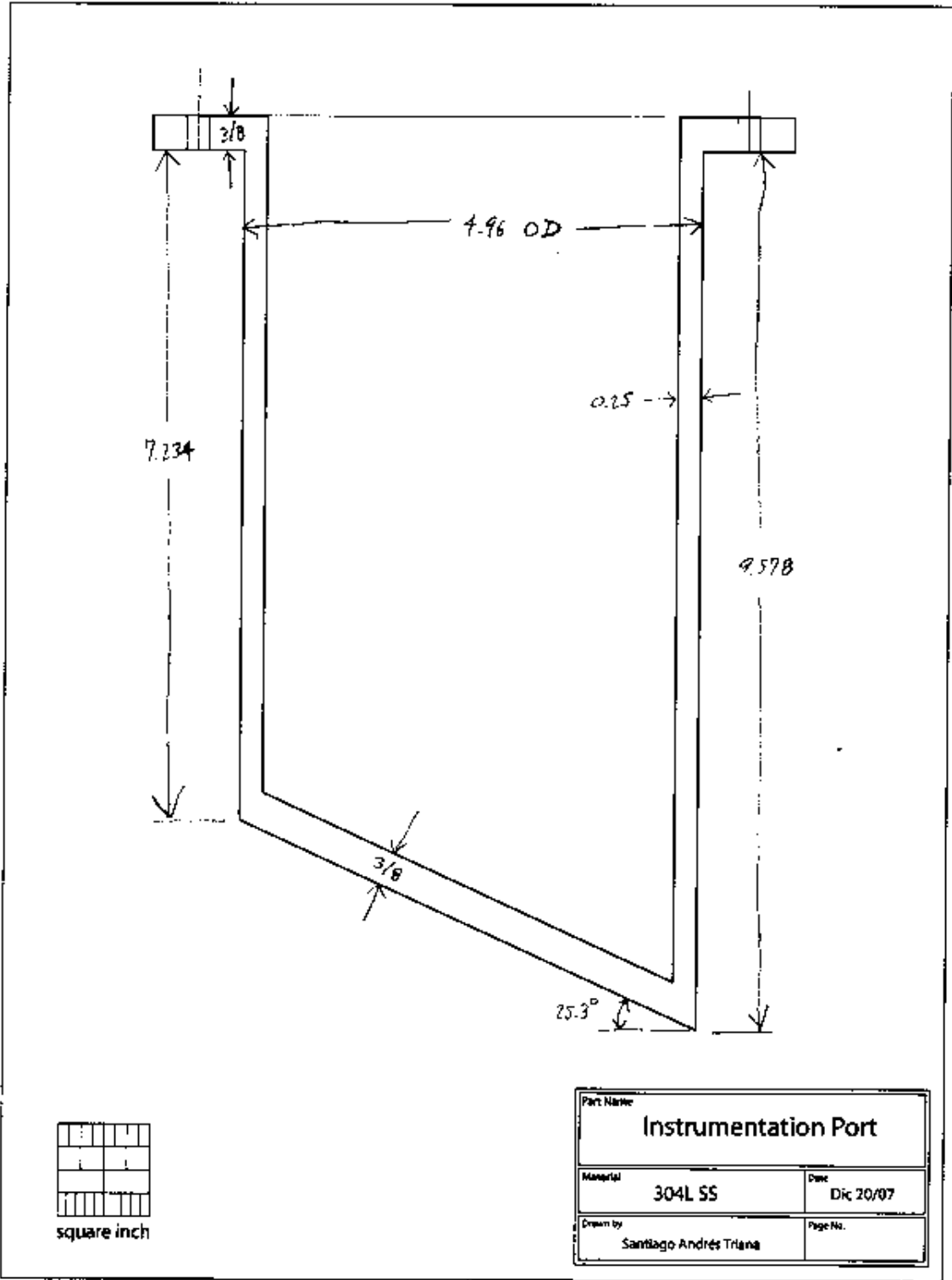
NOZZLE (P) IS IN THE CENTER OF THE TOP OF THE VESSEL.

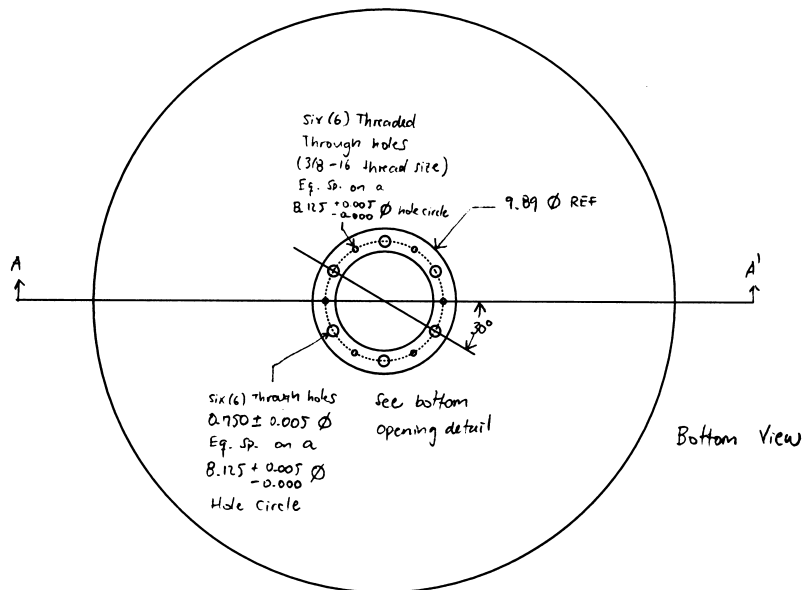
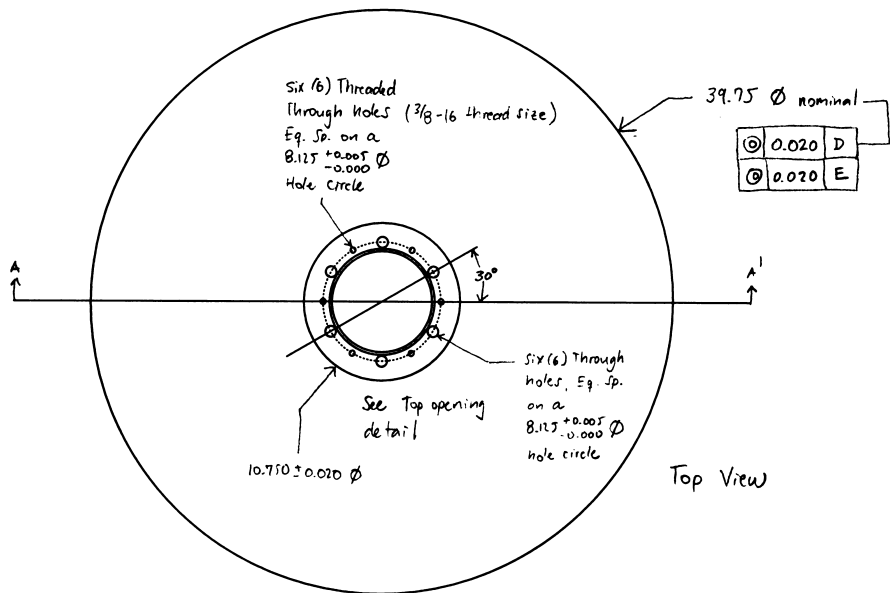
(4) STUDS (15) REQ'D EQ. SP. AT 0°, 90°, 180° & 270°.

(4) FIT NAMEPLATE BRACKET BETWEEN HALF-PIPE @ 60° ABOUT 2/3RDS UP ON THE VESSEL.

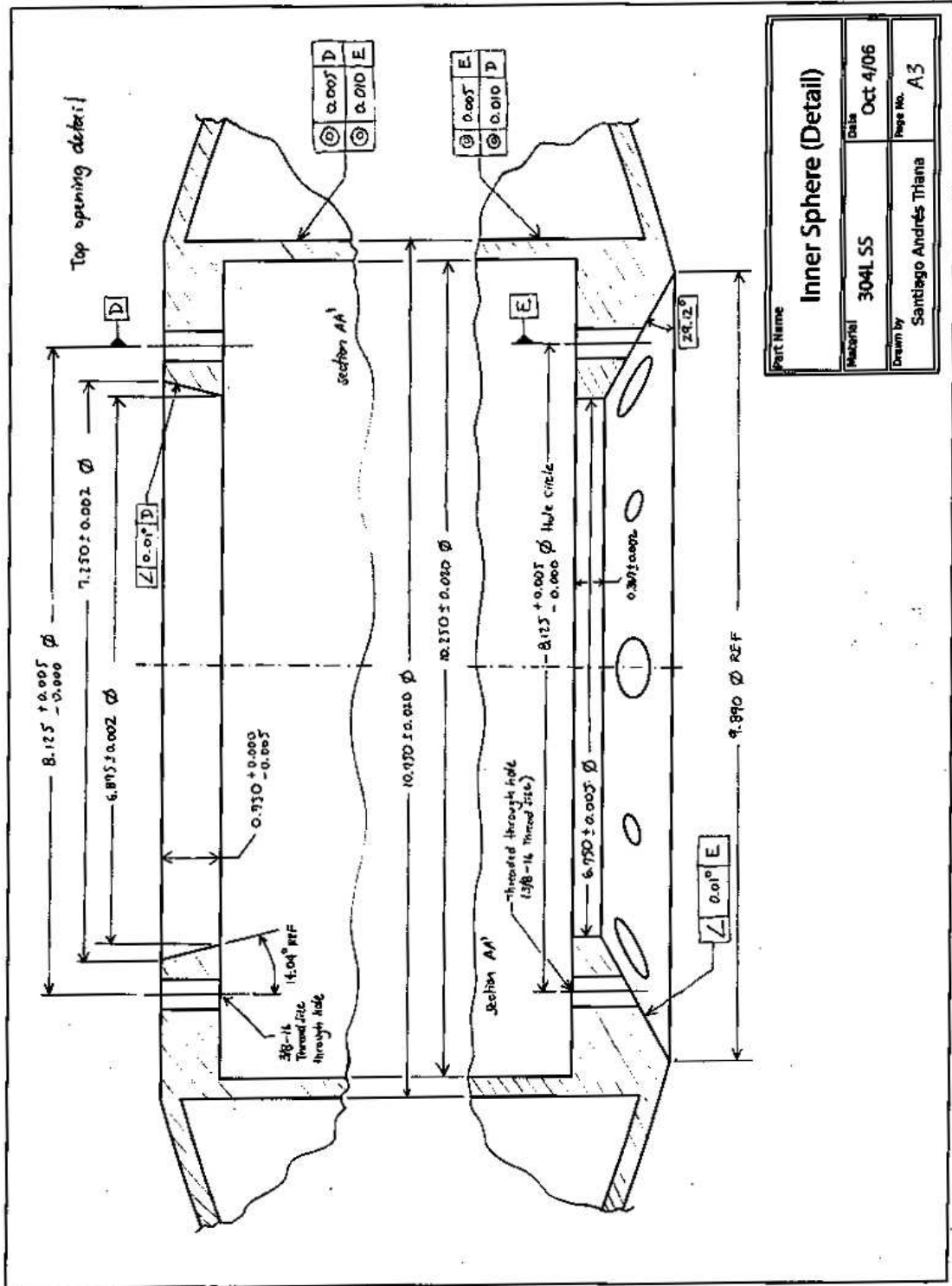
(4) LIFT LUGS (6)(7)(8) REQ'D EQ. SP. AT 45°, 135°, 225° & 315°.



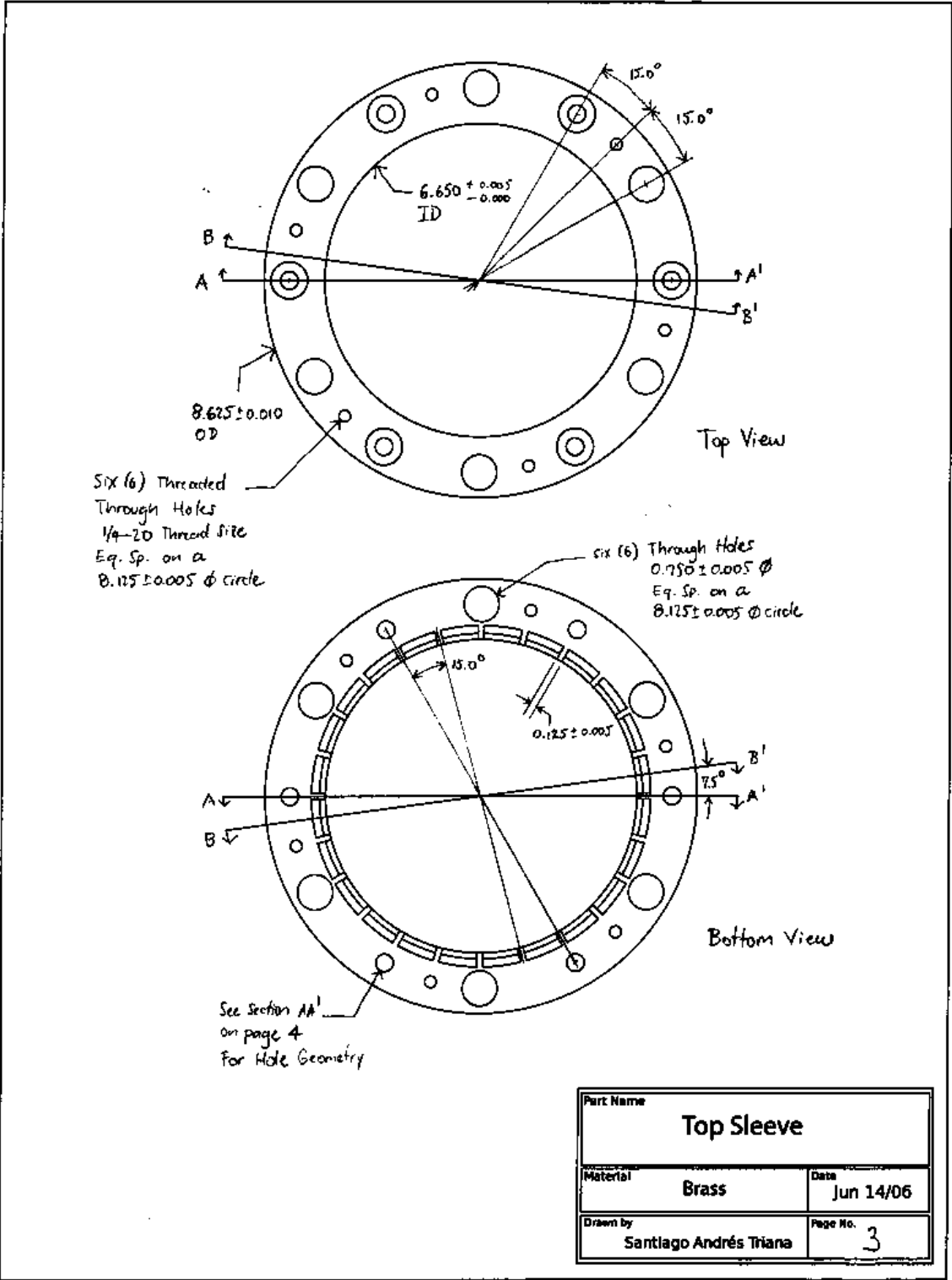


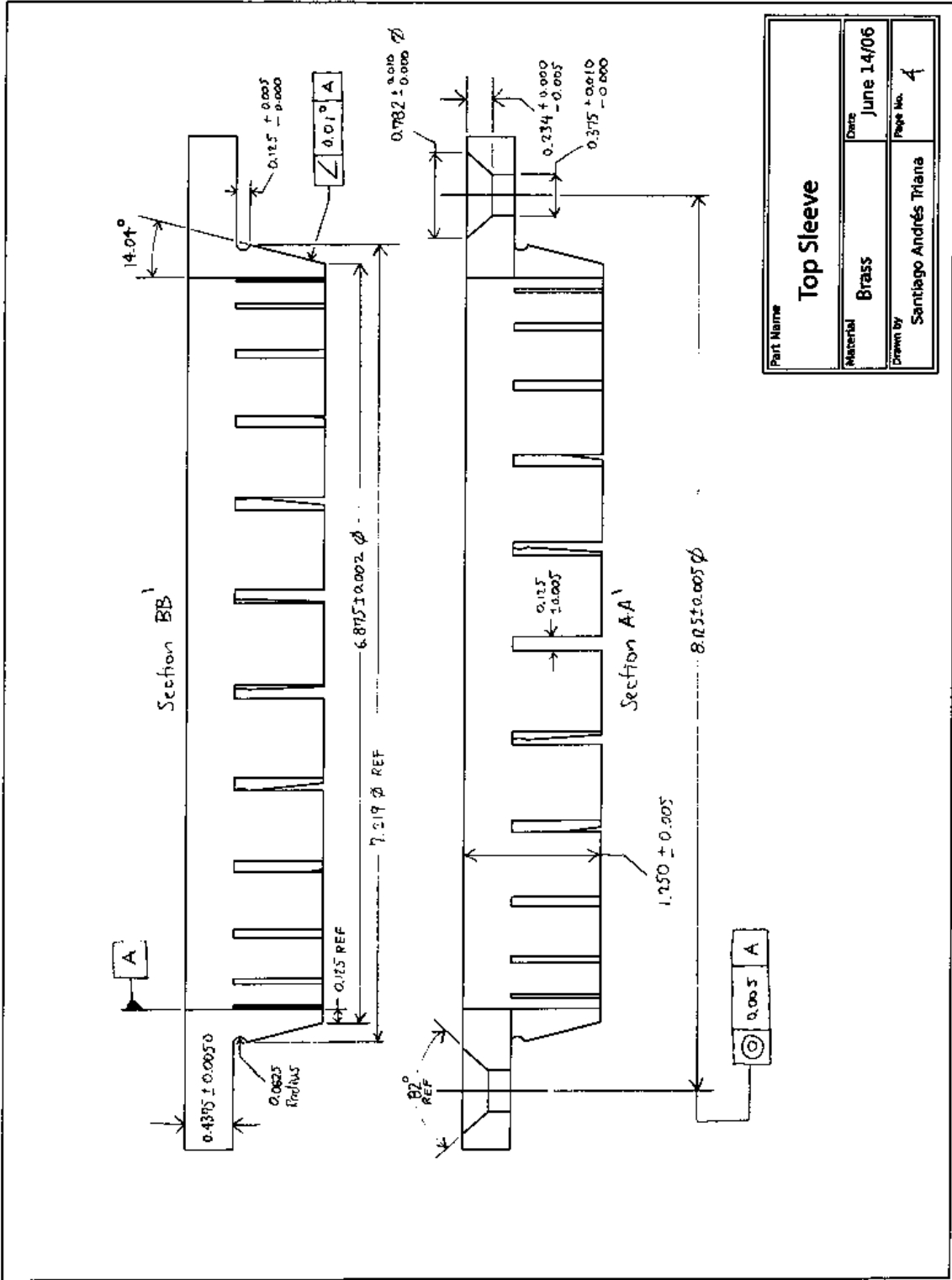


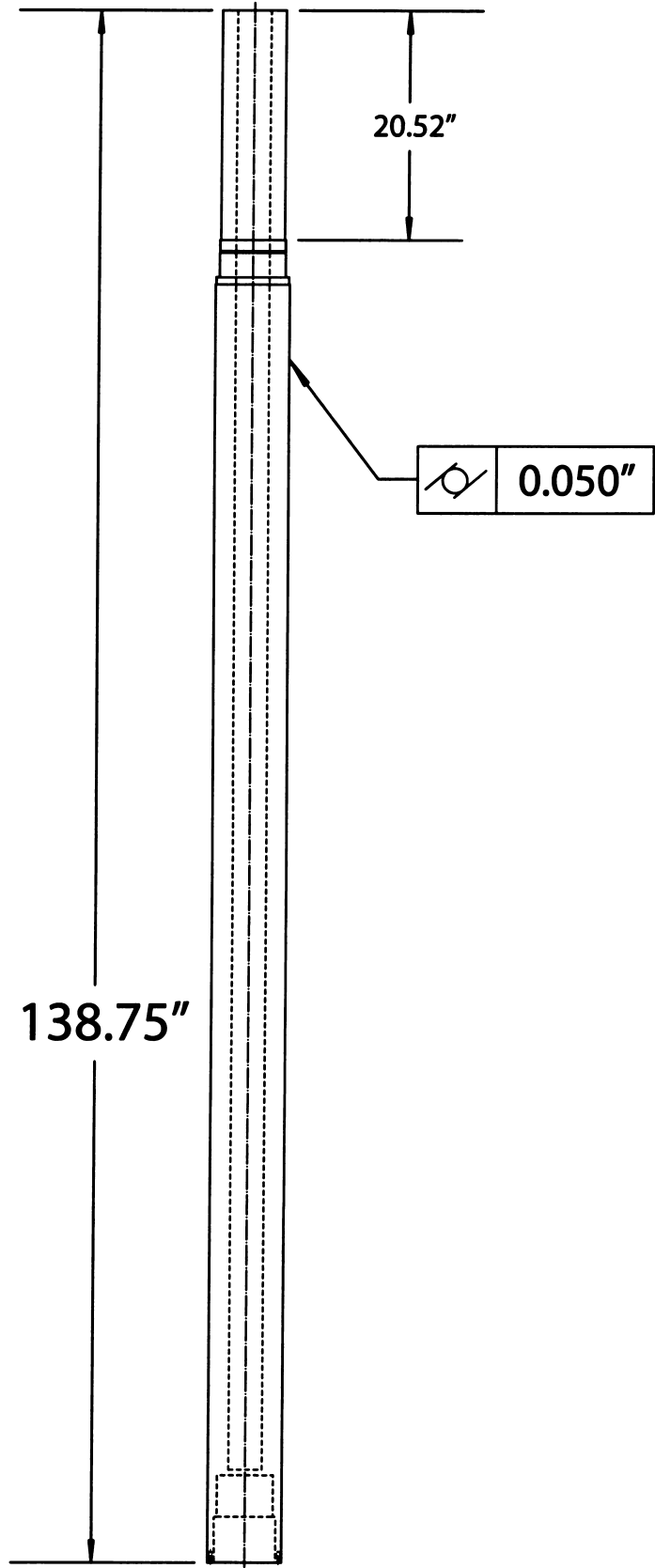
Part Name	
Inner Sphere	
Material	Date
304 L SS	Oct 4/06
Drawn by	Page No.
Santiago Andrés Triana	A2

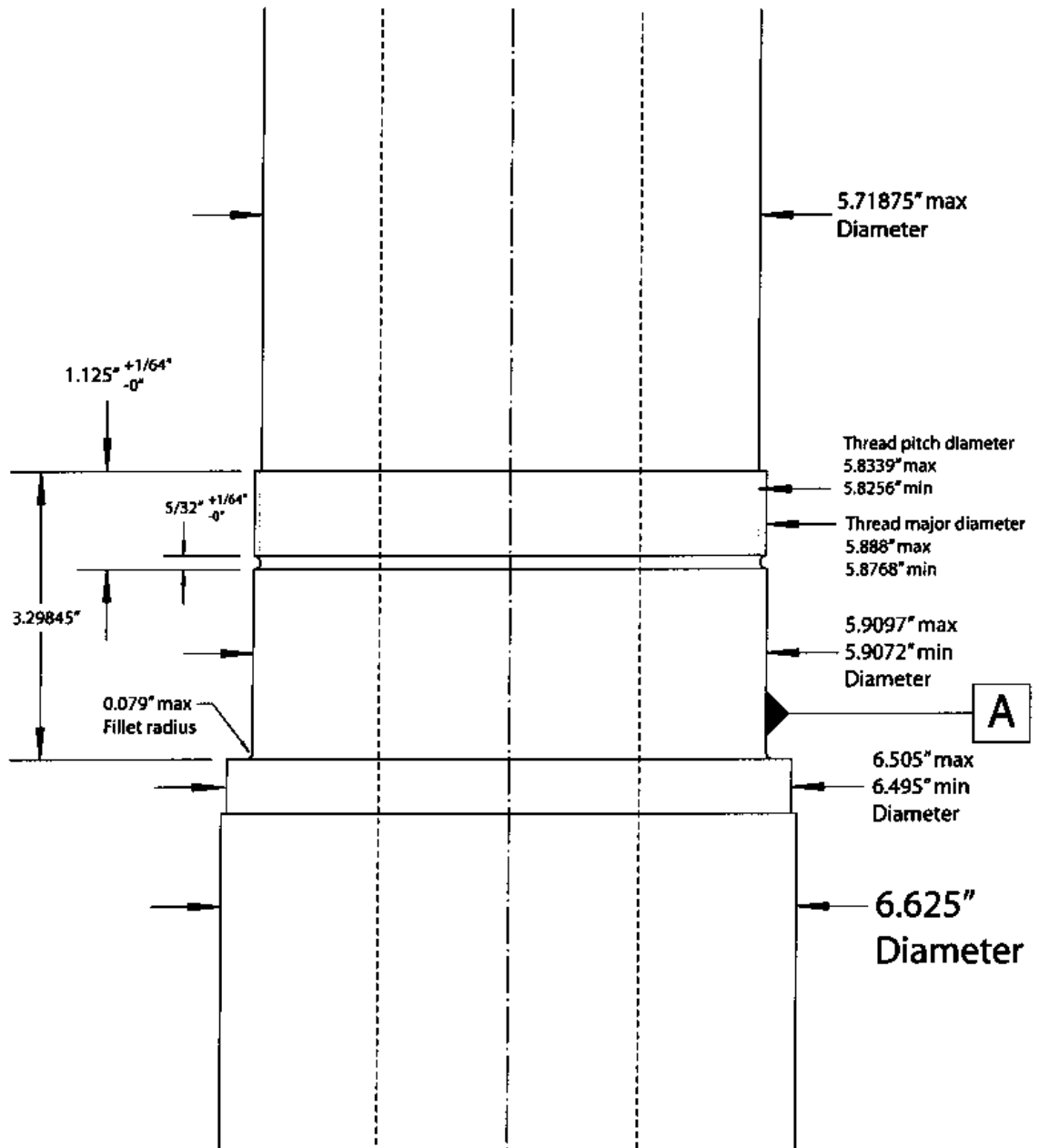


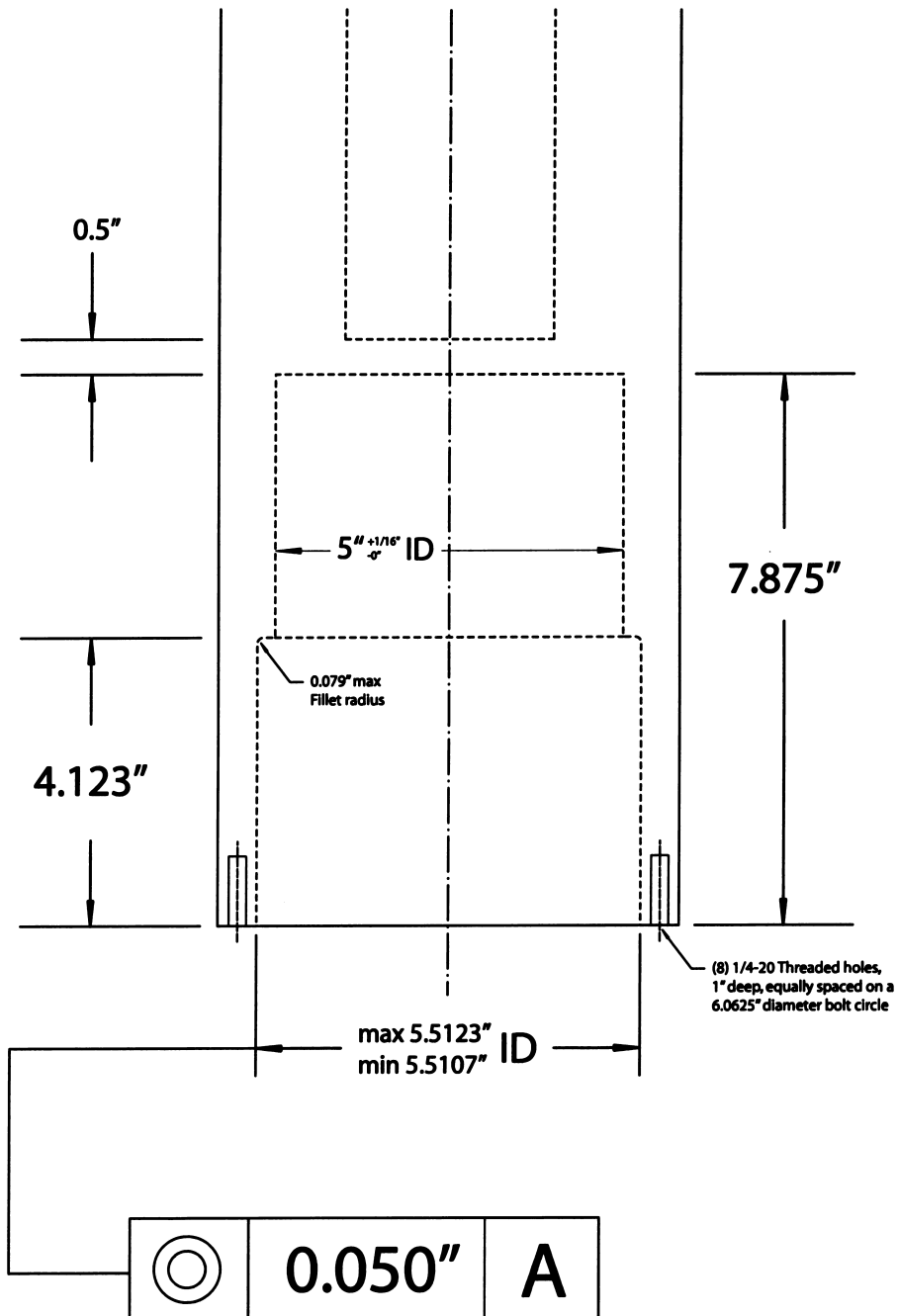
Part Name		Inner Sphere (Detail)	
Material	304L SS	Date	Oct 4/06
Drawn by	Santiago Andrés Triana	Page No.	A.3

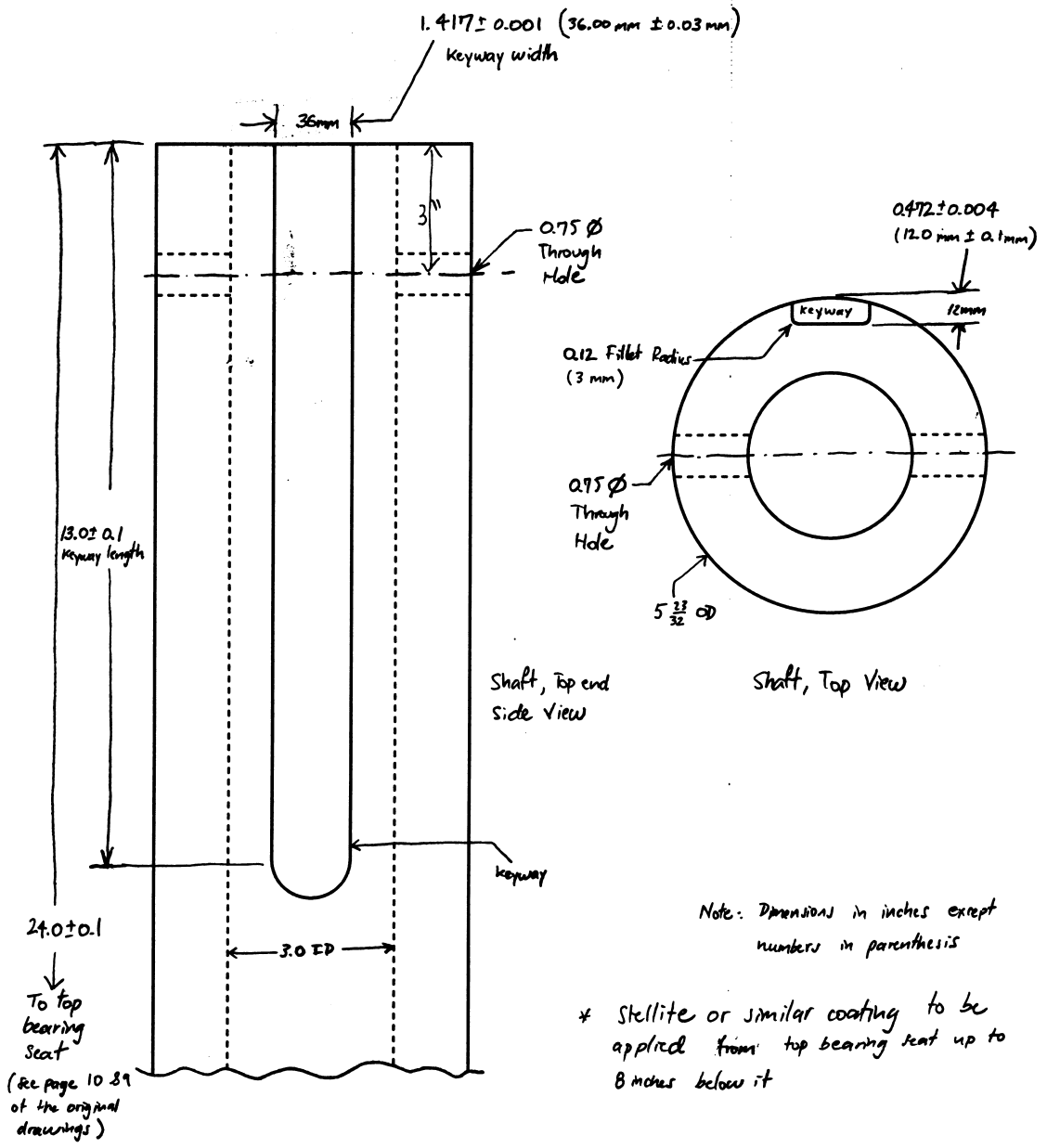


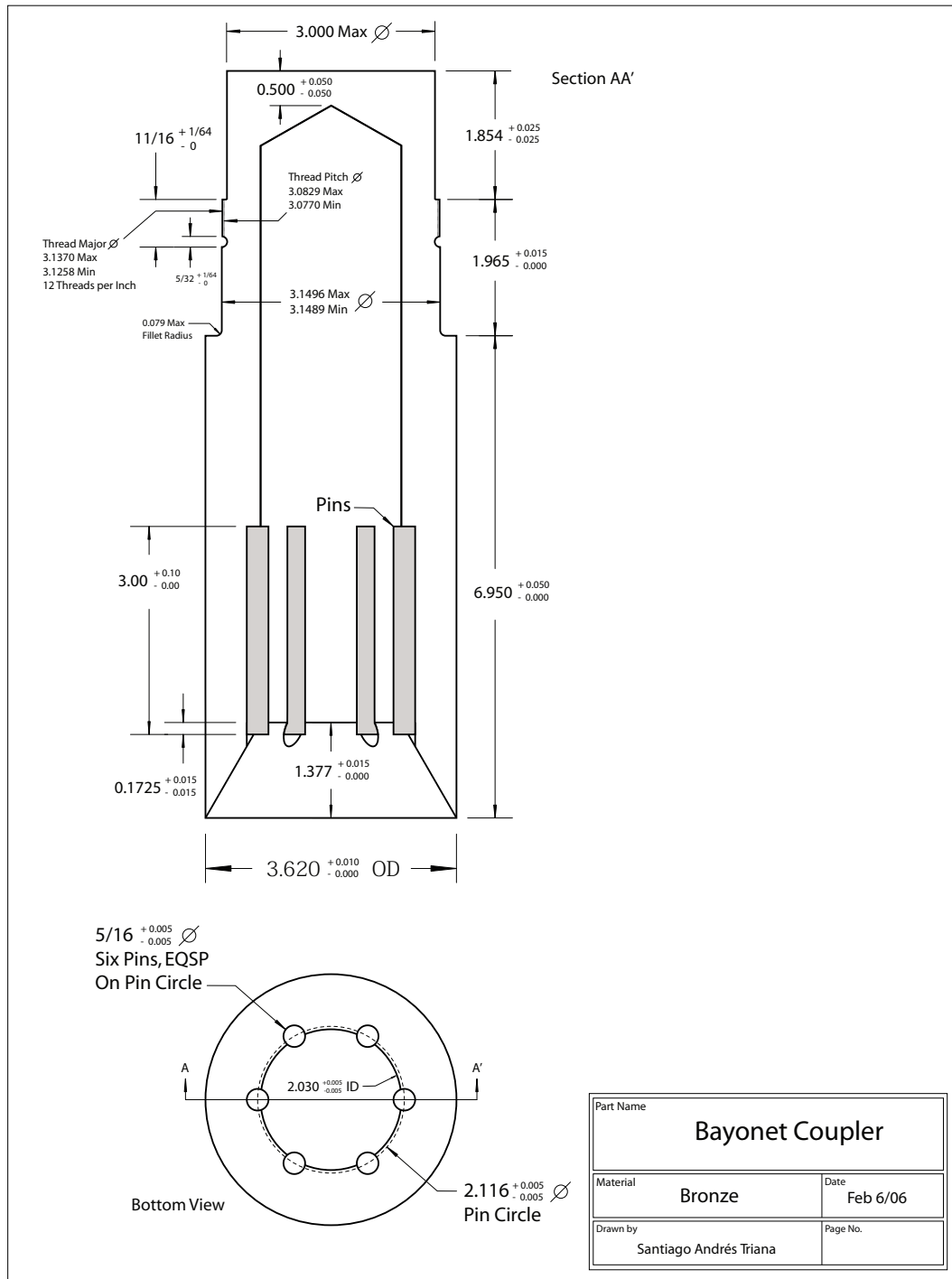












Bibliography

- [1] K. D. Aldridge and L. I. Lumb. Inertial waves identified in the earth's fluid outer core. *Nature*, 325(6103):421–423, 1987.
- [2] K. D. Aldridge and A. Toomre. Axisymmetric inertial oscillations of a fluid in a rotating spherical container. *Journal of Fluid Mechanics*, 37:307–&, 1969. Part 2.
- [3] H. Bondi and R. A. Lyttleton. On the dynamical theory of the rotation of the earth .2. the effect of precession on the motion of the liquid core. *Proceedings of the Cambridge Philosophical Society*, 49(3):498–515, 1953.
- [4] B. A. Buffett, P. M. Mathews, T. A. Herring, and I. Shapiro. Forced nutations of the earth: Contributions from the effects of ellipticity and rotation on the elastic deformations. *Journal of Geophysical Research*, 98:21,659–21,676, 1993.
- [5] F. H. Busse. Steady fluid flow in a precessing spheroidal shell. *Journal of Fluid Mechanics*, 33:739–&, 1968. Part 4.
- [6] E. Dormy, P. Cardin, and D. Jault. Mhd flow in a slightly differentially rotating spherical shell, with conducting inner core, in a dipolar magnetic field. *Earth and Planetary Science Letters*, 160(1-2):15–30, 1998.
- [7] P. Fotheringham and R. Hollerbach. Inertial oscillations in a spherical shell. *Geophysical and Astrophysical Fluid Dynamics*, 89(1-2):23–43, 1998.
- [8] Y. Gasteuil. PhD thesis, ENS-Lyon, 2009.
- [9] H. Görtler. On forced oscillation in rotating fluids. In *5th Midwestern Conference on Fluid Mechanics*, 1957.
- [10] H. P. Greenspan. *The theory of rotating fluids*. Cambridge University Press, 1969.
- [11] R. Hollerbach. Instabilities of the Stewartson layer part 1. the dependence on the sign of Ro . *Journal of Fluid Mechanics*, 492:289–302, 2003.
- [12] R. Hollerbach and R. R. Kerswell. Oscillatory internal shear layers in rotating and precessing flows. *Journal of Fluid Mechanics*, 298:327–339, 1995.
- [13] D. H. Kelley, S. A. Triana, D. S. Zimmerman, and D. P. Lathrop. Selection of inertial modes in spherical Couette flow. *Physical Review E*, 81(2), 2010.
- [14] D. H. Kelley, S. A. Triana, D. S. Zimmerman, A. Tilgner, and D. P. Lathrop. Inertial waves driven by differential rotation in a planetary geometry. *Geophysical and Astrophysical Fluid Dynamics*, 101(5-6):469–487, 2007.

- [15] R. R. Kerswell. The instability of precessing flow. *Geophysical and Astrophysical Fluid Dynamics*, 72(1-4):107–144, 1993.
- [16] R. R. Kerswell. On the internal shear layers spawned by the critical regions in oscillatory ekman boundary-layers. *Journal of Fluid Mechanics*, 298:311–325, 1995.
- [17] R. R. Kerswell. Upper bounds on the energy dissipation in turbulent precession. *Journal of Fluid Mechanics*, 321:335–370, 1996.
- [18] M. D. Kudlick. *On transient motions in a contained rotating fluid*. PhD thesis, M. I. T., 1966.
- [19] R. S. Lindzen, B. Farrell, and K. Tung. The concept of wave overreflection and its application to baroclinic instability. *Journal of the Atmospheric Sciences*, 37:44–63, 1979.
- [20] D. E. Loper. Torque balance and energy budget for precessionally driven dynamo. *Physics of the Earth and Planetary Interiors*, 11(1):43–60, 1975.
- [21] S. Lorenzani and A. Tilgner. Fluid instabilities in precessing spheroidal cavities. *Journal of Fluid Mechanics*, 447:111–128, 2001.
- [22] S. Lorenzani and A. Tilgner. Inertial instabilities of fluid flow in precessing spheroidal shells. *Journal of Fluid Mechanics*, 492:363–379, 2003.
- [23] Fridman A. M., E. N. Snezhkin, G. P. Chernikov, A. Yu. Rylov, K. B. Titishov, and Yu. M. Torgashin. Over-reflection of waves and over-reflection instability of flows revealed in experiments with rotating shallow water. *Physics Letters A*, 372:4822–4826, 2008.
- [24] L. R. M. Maas. Wave focusing and ensuing mean flow due to symmetry breaking in rotating fluids. *Journal of Fluid Mechanics*, 437:13–28, 2001.
- [25] L. R. M. Maas and F. P. A. Lam. Geometric focusing of internal waves. *Journal of Fluid Mechanics*, 300:1–41, 1995.
- [26] W. V. R. Malkus. Precession of earth as cause of geomagnetism. *Science*, 160(3825):259–&, 1968.
- [27] R. Manasseh. Breakdown regimes of inertia waves in a precessing cylinder. *Journal of Fluid Mechanics*, 243:261–296, 1992.
- [28] R. Manasseh. Nonlinear behaviour of contained inertia waves. *Journal of Fluid Mechanics*, 315:151–173, 1996.
- [29] A. D. McEwan. Inertial oscillations in a rotating fluid cylinder. *Journal of Fluid Mechanics*, 40:603–&, 1970.

- [30] L. Messio, C. Morize, M. Rabaud, and F. Moisy. Experimental observation using particle image velocimetry of inertial waves in a rotating fluid. *Experiments in Fluids*, 44(4):519–528, 2008.
- [31] C. B. Moler. *Numerical Computing with MATLAB*. Societ for Industrial and Applied mathematics, 2008.
- [32] S. M. Molodensky. Tides and nutation of the earth: Ii. realistic models of the liquid core. *Solar System Research*, 39(1):54–72, 2005.
- [33] C. Morize, M. Le Bars, P. Le Gal, and A. Tilgner. Experimental determination of zonal winds driven by tides. *Physical Review Letters*, 104(21):4, 2010.
- [34] J. Neuberger, J. Hinderer, and W. Zürn. Stacking gravity tide observations in central europe for the retrieval of the complex eigenfrequency of the nearly diurnal free-wobble. *Geophysical Journal of the Royal Astronomical Society*, 91:853–868, 1987.
- [35] J. Noir, P. Cardin, D. Jault, and J. P. Masson. Experimental evidence of non-linear resonance effects between retrograde precession and the tilt-over mode within a spheroid. *Geophysical Journal International*, 154(2):407–416, 2003. Times Cited: 13.
- [36] J. Noir, D. Jault, and P. Cardin. Numerical study of the motions within a slowly precessing sphere at low ekman number. *Journal of Fluid Mechanics*, 437:283–299, 2001.
- [37] R. Noir, D. Brito, K. Aldridge, and P. Cardin. Experimental evidence of inertial waves in a precessing spheroidal cavity. *Geophysical Research Letters*, 28(19):3785–3788, 2001.
- [38] M. A. Pais and J. L. Le Mouél. Precession-induced flows in liquid-filled containers and in the earth’s core. *Geophysical Journal International*, 144(3):539–554, 2001.
- [39] O. M. Phillips. Energy transfer in rotating fluids by reflection of inertial waves. *Physics of Fluids*, 6(4):513–520, 1963.
- [40] M. Rieutord, B. Georgeot, and L. Valdettaro. Inertial waves in a rotating spherical shell: attractors and asymptotic spectrum. *Journal of Fluid Mechanics*, 435:103–144, 2001.
- [41] M. Rieutord and L. Valdettaro. Inertial waves in a rotating spherical shell. *Journal of Fluid Mechanics*, 341:77–99, 1997.
- [42] M. Rieutord and L. Valdettaro. Viscous dissipation by tidally forced inertial modes in a rotating spherical shell. *Journal of Fluid Mechanics*, 643:363–394, 2010. Rieutord, M. Valdettaro, L.

- [43] P. H. Roberts and K. Stewartson. On motion of a liquid in a spheroidal cavity of a precessing rigid body .2. *Proceedings of the Cambridge Philosophical Society-Mathematical and Physical Sciences*, 61:279–&, 1965.
- [44] M. G. Rochester, J. A. Jacobs, D. E. Smylie, and K. F. Chong. Can precession power geomagnetic dynamo. *Geophysical Journal of the Royal Astronomical Society*, 43(3):661–678, 1975.
- [45] Y. Rogister and B. Valette. Influence of liquid core dynamics on rotational modes. *Geophysical Journal International*, 176(2):368–388, 2009. Rogister, Yves Valette, Bernard.
- [46] T. Sasao, I. Okamoto, and S. Sakai. Dissipative core-mantle coupling and nutational motion of earth. *Publications of the Astronomical Society of Japan*, 29(1):83–105, 1977.
- [47] N. Schaeffer. *Instabilités, urbulence et dynamo dans une couche de fluide cisaille en rotation rapide*. PhD thesis, Université Joseph Fourier Grenoble, 2004.
- [48] D. Schmitt, T. Alboussiere, D. Brito, P. Cardin, N. Gagniere, D. Jault, and H. C. Nataf. Rotating spherical couette flow in a dipolar magnetic field: experimental study of magneto-inertial waves. *Journal of Fluid Mechanics*, 604:175–197, 2008. Schmitt, Denys Alboussiere, T. Brito, D. Cardin, P. Gagniere, N. Jault, D. Nataf, H. -C.
- [49] S. Stergiopoulos and K. D. Aldridge. Inertial waves in a fluid partially filling a cylindrical cavity during spin-up from rest. *Geophysical and Astrophysical Fluid Dynamics*, 21(1-2):89–112, 1982.
- [50] K. Stewartson and P. H. Roberts. On the motion of a liquid in a spheroidal cavity of a precessing rigid body. *Journal of Fluid Mechanics*, 17(1):1–20, 1963.
- [51] A. Tilgner. Driven inertial oscillations in spherical shells. *Physical Review E*, 59(2):1789–1794, 1999. Part A.
- [52] A. Tilgner. Magnetohydrodynamic flow in precessing spherical shells. *Journal of Fluid Mechanics*, 379:303–318, 1999.
- [53] A. Tilgner. Oscillatory shear layers in source driven flows in an unbounded rotating fluid. *Physics of Fluids*, 12(5):1101–1111, 2000.
- [54] A. Tilgner. Precession driven dynamos. *Physics of Fluids*, 17(3), 2005.
- [55] A. Tilgner. Kinematic dynamos with precession driven flow in a sphere. *Geophysical and Astrophysical Fluid Dynamics*, 101(1):1–9, 2007. Tilgner, A.
- [56] A. Tilgner and F. H. Busse. Fluid flows in precessing spherical shells. *Journal of Fluid Mechanics*, 426:387–396, 2001.

- [57] J. Vanyo, P. Wilde, P. Cardin, and P. Olson. Experiments on precessing flows in the earth's liquid-core. *Geophysical Journal International*, 121(1):136–142, 1995.
- [58] J. P. Vanyo. Earth core motions - experiments with spheroids. *Geophysical Journal of the Royal Astronomical Society*, 77(1):173–183, 1984.
- [59] J. P. Vanyo and J. R. Dunn. Core precession: flow structures and energy. *Geophysical Journal International*, 142(2):409–425, 2000.
- [60] C. C. Wu and P. H. Roberts. A precessionally-driven dynamo in a plane layer. *Geophysical and Astrophysical Fluid Dynamics*, 102(1):1–19, 2008. Wu, Cheng Chin Roberts, Paul H.
- [61] C. C. Wu and P. H. Roberts. On a dynamo driven by topographic precession. *Geophysical and Astrophysical Fluid Dynamics*, 103(6):467–501, 2009.
- [62] K. K. Zhang, P. Earnshaw, X. H. Liao, and F. H. Busse. On inertial waves in a rotating fluid sphere. *Journal of Fluid Mechanics*, 437:103–119, 2001.
- [63] D. S. Zimmerman. *Turbulent Shear Flow in a Rapidly Rotating Spherical Annulus*. PhD thesis, University of Maryland, 2010.